Università degli Studi di Ferrara

DOTTORATO DI RICERCA IN
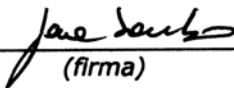## FISICA

CICLO XIII

COORDINATORE Prof. Filippo Frontera

An iterative method
to deconvolve coded-mask images

Settore Scientifico Disciplinare FIS/05

<table>
<tr><td>

Dottorando
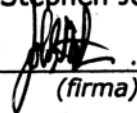Dott. Sambo Lara

_____
(firma)

</td><td>

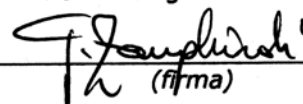**Tutore**
Prof. Frontera Filippo

_____
(firma)

Co-Tutore
Dott. Stephen John Buchan

_____
(firma)

Co-Tutore
Dott. Zanghirati Gaetano

_____
(firma)

</td></tr>
</table>

Anni 2008/2010

Abstract

Efficent astronomical imaging at energy greater than 20 keV is mainly achieved through modulation, either time (i.e. HXMT) or spatial (i.e. IBIS/INTEGRAL), techniques. Currently, the coded mask technique is widely used with the true spatial intensity distribution reconstructed from the data by the cross-correlation (CC) method.
As the sensitivity of instruments increases, so must the angular resolution in order to avoid problems with source confusion. The IBIS 12' angular resolution is clearly not sufficient to distinguish all the sources in the crowded field of the Galactic Centre. One possibility to overcome this problem is to change the deconvolution method.

The objective of this thesis is to evaluate the real imaging capability of the Direct Demodulation (DD) method. It deconvolves incomplete and noisy data by iteratively solving the image formation equation under physical constraints. With the goal of exploiting the DD technique, in the early of the 1990s the HXMT mission was designed, where the imaging capability is obtained through the temporal modulation of the detected counts by a set of mechanical collimators.

To achieve this goal, we developed the Lucy-Richardson (LR) code to reconstruct directly hard-X/soft-γ ray images. It assumes that the data and the noise follow a Poisson distribution and it guarantees the non-negativity of the restored images. For the moment, any kind of regularization or constraint was implemented in the underlying optimization problem, so this will be ill-posed yet.
Due to the general nature of the DD and the fact that HXMT has still to fly, the IBIS/INTEGRAL data and its PSF were used to check our own code. The pure geometrical PSF considering only the effects due to the photon propagation from the mask to the detector was created. Our CC code implements the same balanced cross-correlation as the standard software for IBIS/INTEGRAL analysis. The CC deconvolved images are the reference for the image quality obtained with the LR.

The great improvement in the theoretical angular resolution and location precision is evident. It is independent on the source position in the total FOV, the iteration number and the source flux. Within the parameters of the simulations used, the LR statistical uncertainty was found to be a factor of 10 smaller than that obtained with the CC. Furthermore, the LR deconvolved images have less fluctuating reconstructed background.
The main LR drawback is the flux evaluation of the reconstructed source. It is mainly due to the choice of the correct iteration number. The use of a-priori information about the unknown object allows a complete regularization of the problem, so probably solving the problem with the flux estimation.

Keywords: Coded-mask, Lucy, Richardson, INTEGRAL, IBIS

Abstract

Le immagini astronomiche ad energie maggiori di 20 keV sono ottenute attraverso tecniche di modulazione di tipo temporale (HXMT) o spaziale (IBIS/INTEGRAL). Attualmente la tecnica a maschera codificata è la più usata. In essa la distribuzione spaziale dell'intensità viene ricostruita dai dati attraverso il metodo di cross-correlazione (CC).
Ad un aumento di sensibilità dello strumento dovrebbe corrispondere un aumento della risoluzione angolare al fine di evitare la confusione delle sorgenti. Una risoluzione angolare di 12' come quella di IBIS è chiaramente insufficiente per distinguere le sorgenti in un campo affollato come il Centro Galattico. Una possibilità per ovviare a questo problema è cambiare il metodo di deconvoluzione.

L'obiettivo di questa tesi è valutare le reali potenzialità di fare immagini con il metodo di Demodulazione Diretta (DD). Esso deconvolve dati incompleti e rumorosi risolvendo in maniera iterativa l'equazione di formazione dell'immagine imponendo vincoli fisici. Per utilizzare la DD, all'inizio degli anni Novanta si progettò la missione HXMT, dove le immagini si ottengono attraverso la modulazione temporale dei conteggi misurati da un set di collimatori meccanici.

Per raggiungere questo obiettivo, si è sviluppato il codice Lucy-Richardson (LR) che ricostruisce direttamente le immagini nella banda X-duri/γ-leggeri. Esso assume che i dati e il rumore seguano una distribuzione di Poisson e garantisce la non-negatività delle immagini ricostruite. Per ora, non si è implementato alcun tipo di regolarizzazione o vincolo nel problema di ottimizzazione, così esso sarà ancora mal-posto.
Grazie alla genericità della DD e al fatto che HXMT deve ancora esser messo in orbita, per testare il nostro codice si sono usati i dati di IBIS/INTEGRAL e la sua PSF. Si è creata una PSF puramente geometrica considerando solo gli effetti della propagazione dei fotoni dalla maschera al rivelatore. Il nostro codice CC implementa lo stesso tipo di cross-correlazione pesata usata nel software standard per l'analisi dei dati di IBIS/INTEGRAL. Le immagini deconvolute con il CC sono il riferimento per la qualità dell'immagine ricostruita con il LR.

Il grande miglioramento nella risoluzione angolare teorica e nella precisione di posizionamento è evidente. Esso non dipende né dalla posizione della sorgente nel campo di vista, né dal numero di iterazioni, né dal flusso della sorgente. All'interno dei parametri nelle simulazioni usate, l'incertezza statistica nel LR è un fattore 10 più piccola di quella ottenuta con il CC. Inoltre, le immagini deconvolute con il LR hanno un background ricostruito meno fluttuante.
Il principale inconveniente del LR è la stima del flusso della sorgente ricostruita. Esso è principalmente dovuto alla scelta del corretto numero di iterazioni. L'utilizzo di informazioni a-priori sull'oggetto incognito consente una completa regolarizzazione del problema, così probabilmente risolvendo il problema della stima del flusso.

Contents

Acronyms

AGN Active Galactic Nuclei

ASI Italian Space Agency

BH Black Holes

CC Cross-Correlation code

CXB Cosmic X-ray Background

DD Direct Demodulation

e.m. electromagnetic

EM Expectation-Maximization

ESA European Space Agency

FCFOV Fully Coded Field of View

FOV Field of View

FWHM Full Width at Half Maximum

FWZI Full Width at Zero Intensity

GRB Gamma-Ray Burst

IBIS Imager on Board INTEGRAL

INTEGRAL INTErnational Gamma-Ray Astrophysics Laboratory

HE High Energy

IR Infrared

ISGRI INTEGRAL Soft-Gamma Ray Imager

ISDC INTEGRAL Science Data Centre

KL Kullback-Leibler

LMXB Low-Mass X-ray Binary

LR Lucy-Richardson code

MAP Maximum A Posteriori

ML Maximum Likelihood

MURA Modiefied Uniformly Redundant Array

NLP NonLinear optimization Problem

NS Neutron Star

PCFOV Partially Coded Field of View

PICsIT Pixellated Imaging CsI Telescope

OSA Off-line Scientific Analysis

PSLA Point-source Location Accuracy

PSD Position Sensitive Detector

PSF Point Spread Function

r.v. random variable

SSC Synchtroton Self-Compton

SED Spectral Energy Distribution

SPI SPectrometer on INTEGRAL

s.t. subject to

SW Science Window

URA Uniformly Redundant Array

UV Ultraviolet

WD White Dwarf

Foreward

Efficient astronomical imaging in hard X and γ rays (> 20 keV) is still an observational problem when high energy photons in this range are not focused (e.g. for sky surveys). Indeed, their arrival direction cannot be accurately determined from Compton scattering or pair production. In this case, imaging is mainly achieved through modulation, either time or spatial, techniques. Currently, the coded mask technique is widely used with the true spatial intensity distribution reconstructed from the observational data by the cross-correlation method.

This imaging method requires a Position Sensitive Detector (PSD). In addition, the geometric area of the detector through the mask holes is reduced to half or more and a wide field of view (FOV) will lead to a higher background through the mask aperture. Image distortions (e.g. side lobes, pseudo images, ...) appear in the image obtained by coded aperture telescopes, which strongly reduce the imaging capability for weak sources.

However, as the sensitivity of instruments increases, so must the angular resolution in order to avoid problems with source confusion. For example, in the 4th IBIS/INTEGRAL catalogue [78], the resolution of the telescope is clearly not sufficient to distinguish all the sources in the crowded field of the Galactic Centre. One possibility is to use instruments with less intrinsic angular resolution but which employ the extra dimension of time modulation. Another possibility is to change the deconvolution method. This thesis investigates this way.

A Direct Demodulation (DD) method for inversion was developed in the 1990s by T.P.Li and M.Wu [55] and [56]. With this method, high resolution reconstructions of celestial objects from incomplete and noisy data are achieved by solving modulation equations iteratively under physical constraints. The DD uses an iterative algorithm (Jacobi, Gauss-Seidel, Lucy-Richardson, etc) to reconstruct directly the sky image. These kinds of algorithms are already used in many scientific fields, like medicine, medical

physics or engineering, and also in astronomy, as in the case of the Hubble Space Telescope data analysis [85] and [42].

The novelty of this method is indeed its application to high energy astrophysics. While in the medical physics we know the background contamination, in X and γ ray astronomy we must deal with a lot of unknown sources of spurious signal, like cosmic rays, diffuse cosmic X-ray background (CXB) and instrumental background.

With the goal of exploiting the DD technique, in the early 1990s the high energy astrophysical mission Hard-X ray Modulation Telescope (HXMT) was designed. In this case, a PSD is not required as the imaging capability is obtained through the temporal modulation of the detected counts by a set of suitable mechanical collimators.

Actually the expected capability of obtaining high resolution sky reconstructions by means of the DD was greeted with scepticism probably due to the complex mathematical algorithm involved and, consequently, the difficulty of interpretation.

The goal of this thesis is to investigate the real capability of the DD. With several difficulties tied to the lack of details about DD, I first derived the mathematics behind this method and thus I created my own algorithm, trying to cling as much as possible to the original Chinese idea.

While HXMT employes passive collimators, the IBIS/INTEGRAL is a coded mask instrument. Due to the general nature of DD and the fact that HXMT has still to fly, the IBIS/INTEGRAL data and its PSF were used to check my own code. Indeed, the strong advantage of the algorithm used is its versatility: regardless of instrumentation type used for imaging, it is sufficient to know the PSF as accurately as possible.

In order to compare the DD capability with that of the cross-correlation deconvolution method, only the geometrical effects of the coded mask were considered, disregarding everything which is connected to the instrument implementation limits and payload influences. Indeed, this work is only the first step of what may be obtained with this new method.

After a short overview of the high energy sky (Chapter 1), Chapter 2 will deal with the main type of detectors for high energy astrophysics and the observational limits of the X-ray telescopes. Before applying the DD to real IBIS/INTEGRAL data, the basic concepts of coded mask imaging should be dealt with, including the classical cross-correlation (CC) deconvolution technique and the definition of the Modified Uniformly Redundant Array

(MURA) (Chapter 3). Chapter 4 will describe the IBIS instrument aboard the INTEGRAL satellite and the fundamental CC steps for the analysis of its data.

Chapter 5 will focus on the DD and Lucy-Richardson (LR) algorithm, describing the details of the new code. Chapters 6 and 7 will show the results of the analysis for both simulated and real IBIS/INTEGRAL data, respectively. They confirm the power of the proposed reconstruction algorithm as made the preliminary results discussed at "The Extreme Sky: Sampling the Universe above 10 keV" Congress [66]. Finally, Chapter 8 will draw conclusions and outline prospects for the future.

Chapter 1

The hard-X/softγ ray band

As said before, this thesis studies the real capability of the DD deconvolution method. This chapter will make a general overview of the X ray sky, dealing with the main problems and the main emission mechanisms. Furthermore, since the LR code is tested employing data from the IBIS/ISGRI imager aboard the INTEGRAL satellite, the main kinds of sources that are detected by this telescope will be shortly described .

1.1 Introduction

The term light refers to the entire frequency range of electromagnetic radiation. Each photon has its own frequency and, depending on it, the nature of the radiation dramatically changes.

X rays and γ rays are highly energetic form of light, ranging from a few tens of keV until about several MeV. An X ray is a quantum of e.m. radiation with energy in the range 12 eV to 120 keV. Traditionally, the soft-X ray band is defined as the energy range 0.12-12 keV (corresponding to wavelength of 100-0.1 nm), the hard-X ray extends to about 120 keV (0.01 nm wavelength). The higher the photon energy, the higher is the penetrating power and the harder are the X rays. The energy range beyond hard-X rays to a few MeV is regarded as soft γ rays (wavelength less than 10 pm).

X and γ rays are produced in the cosmos when gas is heated to millions and billions of degrees or electrons have been accelerated to near the speed of light by violent and extreme conditions. Exploding stars, neutron stars (NSs), black holes (BHs) and galaxy clusters are among the objects which give birth to this radiation.

The lauch of the INTErnational Gamma-Ray Astrophysics Laboratory (IN-

TEGRAL) satellite (15 keV-10 MeV, i.e. from hard-X to soft-γ rays) in October 2002 marked the beginning of a new chapter in high energy astrophysics, since it observes γ rays across a broad energy spectrum with unequalled precision and resolution.

1.2   Brief historical overview

X rays were first observed in 1985 by W.C.Röntgen, a German scientist who found them quite by accident when experimenting with vacuum tubes. He called them "X" to indicate their unknown nature. In 1900 P.Villard, a French chemist and physicist, discovered γ rays while studying radiation emitted from radium. In 1910 Bragg demonstrated that γ rays ionize gas just like X rays. This signaled the first step towards the identification of X and γ rays as e.m. radiation.

The direct observation of the X ray sky began after the Second World War, when a large number of captured V2 rockets were made available to scientists for small experiments in sub-orbital flights. These led H. Friedman to detect X rays from the Sun corona in the 1950s.

The most important event was the X ray detection of Scorpio X-1. In 1962, during an attempted observation of X ray fluorescence from the Moon, R.Giacconi detected the first extra-solar X ray source in the constellation of Scorpius, Sco X-1 [34]. Assuming that it was a nearby star, it would emit X rays at a rate of 10^7-10^8 times greater than the Sun. In 1966 the optical counterpart of Sco X-1, V818 Scorpi, was discovered [67] and [49]. This object emitted 1000 times more power at X ray wavelengths than at optical ones. It is now known that Sco X-1 is a Low-Mass X ray Binary (LMXB), i.e. a compact 1.4 $M_\odot$ NS accreting matter from a 0.42 $M_\odot$ companion star and transforming gravitational energy to e.m. ($M_\odot$ =1.99 10^{33} g is the mass of the Sun).

The first earth-orbiting mission entirely dedicated to X-ray astronomy was X-ray Small Astronomy Satellite SAS-1 (2-20 keV), also called Uhuru. It was lauched in December 1970. After this, NASA launched two other companion satellites in 1972 and 1975. SAS-3 (0.1-60 keV), the first fully imaging X ray telescope, could determine bright X ray source locations to an accuracy of 15 arcsec. It was the first to survey the soft X ray background (0.1-0.28 keV).

The orbital motion in Cen X-3 [69] confirmed that many X ray sources originate in galactic close binary star systems in which mass is transferred from

a normal star to a collapsed one. The in-fall mass into the collapsed object powers the X ray radiation. In other sources the X rays were found to originate from synchrotron emission in the nebulae of supernovae remnants.

The High Energy Astrophysical Observatory HEAO-1 A2 full-sky cosmic X ray experiment (1977-1979) scanned the X ray sky over 0.2 keV-60 keV. It provided the most comprehensive data on the cosmic X ray background (CXB) broadband spectrum. The solid state spectrometer at the focus of the HEAO-2 Einstein Observatory (0.2-20 keV) grazing incidence telescope was the first high resolution spectrometer to be used for X ray astronomy. In the next decades, more sensitive instrumentation was lauched into space which permitted a deeper understanding of the environment of X ray sources.

NASA's Compton Gamma-Ray Observatory (CGRO) inaugurated a new era in γ ray astronomy with its unprecedented sensitivity and coverage of a large range of γ ray energies (30 keV-30 GeV). The Compton Observatory was succeeded by ESA's INTEGRAL, lauched in October 2002. In Chapter 4, the INTEGRAL satellite will described, with a particular accent on the IBIS imager.

NASA's Rossi X ray Timing Explorer (RXTE; 2-250 keV), lauched in December 1995, has the ability to study changes in the intensity of X rays produced in the violent environment around NSs and BHs on time scales ranging from microseconds to months. Two other NASA missions, the High-Energy Transient Explorer (HETE-2; 0.5-400 keV), lauched in 2001, and the Swift satellite, lauched in 2004, are dedicated to the exploration of GRBs. Swift carries three instruments: the Burst Alert Telescope (BAT; 15-150 keV), the X ray Telescope (XRT; 0.2-10 keV) and the Ultraviolet/Optical Telescope (UVOT; 170-650 nm).

1.2.1 X ray detection issues

There are some important issues that must be considered in the hard-X/soft-γ ray energy band. First, the hard-X/soft-γ photons are absorbed by the atmosphere, so to detect them telescope must be placed above most or all the atmosphere (higher than 40 km a.s.l.) using balloons and satellites. However, the region between the UV and low energy X rays (0.1 keV) is inacessible even from space, given that the interstellar medium is opaque to them.

Balloon-borne high energy imaging telescopes has provided important discoveries, such as the first images of the sky between 20 and 1000 keV and the BH candidate source in the Galactic Centre region. Their main draw-

back is their short mission life (at most a few days), although nowadays with circumpolar flights, durations of up to 30 days are becoming possible.

The best way to perform hard-X/γ-ray observations is to place telescopes aboard satellites. In this way, instruments are able to observe the full range of the X ray spectrum and they can collect data for several years.

Another problem of hard-X/soft-γ ray astronomy lies in the very nature of the rays themselves. The higher the frequency of a photon, the higher its energy is, the lower is the number of photons emitted with an equal amount of energy. A X ray source would emit a million times less high energy photons than visible ones. Furthermore, the high energy instruments detect also cosmic rays, massive particles having nothing to do with the e.m. radiation. They are difficult to be distinguished: high energy observations are, therefore, contaminated by them.

As in the other regions of the e.m. spectrum, also in hard-X/soft-γ rays we can made imaging and spectroscopy. Hard-X and γ rays have energies such that traditional techniques (i.e. lenses or mirrors) cannot be employed to focus them. X rays can make reflect off mirrors only if photons strike at grazing angles (see Sect.2.4). For this reason, X ray mirrors have to be carefully shaped and aligned nearly parallel to the incoming X rays.

The Chandra X-ray Observatory (0.1-10 keV), lauched by NASA in July 1999, is one of the premier focusing X ray telescopes. It has an assembly of four pairs of the smoothest mirrors ever constructed.

The ESA's XMM-Newton (0.1-15 keV), a powerful telescope launched in December 1999, had 58 mirrors. They were not as smooth as Chandra's, so XMM could not make images with the same crispness, but it could detect fainter sources and measure the energy of the X rays very accurately. Thanks to its very large collecting area, it was specialised in spectroscopy.

The imaging problem of hard-X rays ($E > 20$ keV) can be solved by applying temporal or spatial multiplexing techniques. A straightforward example of spatial multiplexing is a coded mask system, a mask with a special pattern of holes, which is placed at a given distance from a PSD. The photons incident on the mask will project a shadow onto the detector allowing the location of the sources in the FOV of the telescope. Passive modulation collimators are instead an example of temporal multiplexing. They will be used in the Chinese HXMT mission still under development. Multiplexing techniques will be discussed in Chapter 3, with particular attention on coded masks principles.

1.3 The high energy sky

X and γ astronomy has unveiled a Universe very different from that known from optical observations. It presents unique opportunities to explore exotic objects, to search for new physics, testing theories and performing experiments which are not possible in earth-bound laboratories. Observing the Universe at these energies allows us to understand how matter and radiation interact with each other under extreme conditions, such as at temperatures of hundreds of millions of degrees, where matter is very dense and the magnetic fields are very strong.

High energy observations have also revealed many types of objects with variability timescales from years, months, days or hours down to milliseconds. The energy source is mainly the conversion of gravitational energy in to e.m. radiation.

This section overviews the main types of high energy sources that the IBIS imager aboard the INTEGRAL satellite can observe. Some fields containing this kind of sources will be analyzed with the LR code in Chapter 7.

1.3.1 Supernovae

When a massive star (≥ 10 M$_\odot$) has used up the nuclear fuel that makes it shine, the pressure drops in its central core. Gravity crushes the matter in the core to higher and higher densities. The temperature increases to billions of degrees and the intense heat generated in the collapse produces a cataclysmic rebound that sends debries flying outward. A thermonuclear shock wave accelerates the expanding stellar debries, producing a brilliant visual outburst with the brightness of several hundred million suns. This phenomena is called a supernova explosion. The shell of matter thrown off by the supernova creates a magnetized object of gas of several million degrees mixed with high energy particles, called a supernova remnant. The hot gas expands and produces X rays for thousands of years. An example of this phenomenon is Cassiopeia A (Cas A), the 320-year-old remnant of a supernova explosion.

1.3.2 Neutron stars: the Crab

In 1731 John Bevis discovered the Crab Nebula. Located in the costellation of Taurus, it is a pulsar immersed in a nebula. At energies above 30 keV, the Crab is generally the strongest persistent source in the sky, with a measured flux extending to above 10^{12} eV. Today the Crab has a luminosity

of $8 \times 10^4 L_\odot$, where $L_\odot = 3.828 \times 10^{33}$ erg s^{-1} is the luminosity of the Sun. In 1968, at the centre of the Crab supernova remnant, Lovelace discovered the pulsar PSR 0531-21, with the very short pulse period of only 0.0333 s [20]. The collapse of the supernova and the rapid rotation of the NS caused it to become highly magnetized. The NS gravity is overwhelmed by the electric field and particles are pulled off the NS and accelerated to speeds close to the speed of light. An intense shower of electrons and positrons is produced by these particles. As particles spiral around magnetic field lines, they produce synchrotron radiation, visible in the pulsed emission from the Crab Nebula.

The rotation-powered activity of an isolated NS can last only a few thousand years. However, if it is in binary system, its X ray intensity may increase again. Indeed, when the companion star enters the red giant stage of its life, it will increase greatly in size and gas will flow from the giant onto the NS. The gas will be heated to tens of millions of degrees as it falls onto the surface of the NS and the compact object will shine in X rays.

1.3.3   Black holes and quasars

When some very massive stars collapse, they form a BH. A BH does not have a surface in the usual sense of the word. There is simply a region, the event horizon, around a BH beyond which nothing can escape from the inside. For this reason, a BH cannot be seen directly.

One of the best methods for finding a BH is to study X ray binary systems. Some binary systems have compact objects with a so great mass (more than 3 $M_\odot$) that it cannot be a NS.

As gas and dust particles stripped from the companion swirl toward a BH, they speed up and form a flattened disk around it. The matter inside the disc cycles faster the closer it gets to the BH due to the conservation of momentum. The gas particles are heated to temperatures around 10^8 K, so creating an ionized plasma. Just before the fall into the BH, the fast rotated charged particles create an e.m. field and there is X and γ rays emission into two jets perpendicular to the disc.

Massive BHs live in the centres of galaxies and can be very bright (AGN) or very quiet as the massive SgrA in the centre of the Milky Way.

Cygnus X-1 is the strongest X ray emitter in the Cygnus constellation as seen from Earth. After its discovery in the 1965 [12], it was the first source accepted to be a BH candidate. It is a very close bound binary system with a 33 $M_\odot$ giant blue star, orbiting around a 15 $M_\odot$ BH.

A BH grows when matter falls into it, so a BH in the centre of a galaxy where stars are densely packed may grow to the mass of 10^9 M$_\odot$, which is about the upper limit for BH masses. A great quantity of energy can be released from large clouds of gas as they fall into these supermassive BH. Supermassive BHs are usually located outside the Milky Way and give rise to different types of objects.

Quasars are distant galaxies hosting a strongly interacting supermassive BH in their centre. Their power output at the centre of a galaxy can be a thousand times greater than an entire galaxy of 10^{11} stars. For this reason, the sources are also called Active Galactic Nuclei (AGN).

1.3.4 Gamma Ray Burst

GRBs are the most energetic events observed in the Universe and, for few seconds, they can become brighter than 10^{15} L$_\odot$. They have a cosmological origin and sometimes come from the far reaches of the Universe.

According to their duration, there appear to be at least two types of GRBs. Short ones (0.3 s on average) are likely produced by the merger of two NSs or a NS and a BH. Long bursts (about 30 s on average) represent the explosions of extremely massive stars (> 50 M$_\odot$) at the end of their life.

GRBs are observed to occur about twice per day. They are totally unpredictable and appear randomly in the sky. Even if the INTEGRAL payload was not specially designed to support primarily a GRB mission, its wide energy band coverage and fine imaging capabilities make this satellite well suited to provide important observational data on GRB.

1.3.5 Cosmic X ray background

The combination of many unresolved X ray sources gives rise to the X ray background (CXB). Discovered by Giacconi [34] in 1962, the CXB was initially suggested to be due to the emission from a hot diffuse intergalactic medium, well described by a thermal bremsstrahlung with $kT_e \approx 40$ keV [59]. It was, however, immediately clear that it would be very difficult to understand how a gas of this temperature could be heated and distributed throughout space.

It was first suggested by Setti and Woltjer [70] that the CXB is comprised mainly of AGNs powered by accreting supermassive BHs at the centers of large galaxies [19] and [35]. Optically bright quasars and Seyfert galaxies dominate at low energy (up to a few keV), while obscured AGNs are respon-

sible for the bulk of the CXB at energies greater than 10 keV.

The major effort to get a reliable estimate of the spectrum in a broad energy band (2-400 keV) was performed in the late 1970s using the A2 (3-60 keV), A4 (13-180 keV) and Medium Energy Detector (MED, 100-400 keV) instruments aboard HEAO-1. The HEAO-1 results ([59], [8], [9], [10], [11] for A2; [40] and [41] for A4; [50] for MED) on the CXB spectrum are consistent with the best fit $E \times J(E)$ spectrum given by a bell shape with a maximum intensity of 42.6 keV cm^{-2} s^{-1} sr^{-1} at 29.3 keV, and an energy spectrum below 60 keV given by a power law with a high energy exponential cutoff:

$$F(E) = 7.877 E^{-0.29} e^{-\frac{E}{41.13}} erg\ keV^{-1}\ cm^{-2}\ s^{-1}\ sr^{-1}. \tag{1.1}$$

After HEAO-1, no other CXB measurement was performed in the hard X ray range (> 15 keV). At lower energies several CXB detections were performed with imaging telescopes aboard the satellite missions ROSAT (0.1-2 keV), ASCA (1-8 keV), Beppo-SAX (1-8 keV; [83]), XMM-Newton (2-8 keV), Chandra (0.5-8 keV), and with the non imaging PCA (3-15 keV) aboard the Rossi-RXTE. All these low energy measurements show sistematically higher CXB intensities than those obtained with HEAO-1. Probably there are systematic errors in the HEAO-1 measurements.

Frontera [33] reported the first accurate hard X ray measurement of the CXB in the 15-50 keV range after that of HEAO-1, performed with the PDS instrument aboard the Beppo-SAX satellite. The most likely CXB intensity level at its emission peak (26-28 keV) was found to be about 40 keV cm^{-2} s^{-1} sr^{-1}, consistent with those obtained with HEAO-1 at the same energies.

At energies greater than 100 keV, where the bulk of the background energy resides, the only available measure is that of HEAO-1.

1.4 X ray emission mechanisms

In this section the main issues on X ray emission mechanisms are dealt with. For further details see [65]. Any charged particle in accelerated motion loses energy and emits e.m. radiation. The intensity of the radiation is ruled by Larmor's formula:

$$\frac{dW}{dt d\Omega} = \frac{1}{4\pi c^3} q^2 \left(\frac{dv}{dt}\right)^2 \sin^2\Theta, \tag{1.2}$$

where q is the electric charge, v is the particle velocity, Θ the angle between the acceleration vector and the emission direction. In the non relativistic case (Eq.1.3), the power P, averaged over the emission angles, is in general inversely proportional to the square of the mass of the emitting particle. So, electrons emit much more than protons.

$$P = \frac{dW}{dt} = \frac{2}{3c^2}q^2\left(\frac{dv}{dt}\right)^2 \sin^2 \propto \left(\frac{F}{m}\right)^2. \tag{1.3}$$

If the velocity v of the emitting particle is relativistic, then the power is:

$$P = \frac{2}{3c^2}q^2\gamma^4\left[\left(\frac{dv}{dt}\right)^2_{perp} + \gamma^2\left(\frac{dv}{dt}\right)^2_{parallel}\right], \tag{1.4}$$

where γ is the Lorentz factor ($\gamma = (1 - v^2/c^2)^{-1/2}$) of the emitting particle and the acceleration vector is decomposed in the components parallel and perpendicular to the velocity. The equation of the radiative transfer is:

$$\frac{dI_v}{d\tau_v} = -I_v + S_v, \tag{1.5}$$

where $\tau_v = \alpha_v ds$ is the optical depth, $S_v \equiv j_v/\alpha_v$ the source function and I_v the intensity. j_v and α_v are the emissivity and the absorption coefficients, defined as:

$$j_v \equiv \frac{dE}{dV\ dt\ dv\ d\Omega} \qquad \alpha_v = -\frac{1}{I_v}\frac{dI_v}{ds}. \tag{1.6}$$

Different processes emit their own characteristic radiation. Here the main emission mechanisms are briefly described. For X and γ rays, it is customary to divide them into thermal and non-thermal, according to whether the velocity distribution of the emitting electrons is Maxwellian or not.

1.4.1   Thomson scattering

Thomson scattering results from the interaction of a photon with a free electron at rest, with $h\nu << mc^2 = 511$ keV. Scattering is one of the most important processes in high energy astrophysics between 100 keV and 10 MeV, as it allows to transfer an important fraction of the electron energy to the photons and thus to cool the electron plasma. Furthermore, the resulting radiation appears predominantly in the X rays up to TeV energies.
Thomson scattering is an elastic process, whose cross section has the same value for all energies:

$$\sigma_T = \frac{8\pi}{3}\left(\frac{e^2}{m_e c^2}\right)^2 = 6.65 \; 10^{-25} \; cm^2, \tag{1.7}$$

where

$$r_0 = \frac{e^2}{m_e c^2} = 2.82 10^{-13} \; cm \tag{1.8}$$

is the classic radius of the electron. The small size of σ_T means that the electron scattering is most effective as a source of opacity at high temperature, as in planetary and stellar atmosphere.

1.4.2   Pair production and annihilation

An electron-positron pair $e^+ - e^-$ may annihilate producing two γ rays for the conservation of momentum. If the electrons are not relativistic, the two photons have energy of $E = 511$ keV. It is a threshold process: the photon energy must be greater than the equivalent rest mass of the pair ($2E_0 = 2m^2 c^4 = 1.02$ MeV).

At extreme environments of compact objects as pulsars and accreting BH, conversely, two γ rays or a γ ray with a nucleus, may produce a $e^+ - e^-$ pair. This mechanism is called pair production. The cross sections are:

$$\sigma_{\gamma\gamma} \approx \sigma_T \tag{1.9}$$

$$\sigma_{\gamma p} \approx \alpha \sigma_T \tag{1.10}$$

where $\alpha \approx 1/137$, for pair production obtained by two γ rays and a γ ray and the nucleus p, respectively.

1.4.3   Bremsstrahlung

Bremsstrahlung ("braking radiation") is produced by the deflection of a charged particle (usually an electron) in the Coulombian field of another charged particle (usually an atomic nucleus). It is also called free-free emission, because the electron is free both before and after the deflection that causes the emission.

Bremsstrahlung is likely to be operating in virtually all X ray sources. It's important in HII regions, planetary nebulae, stars and clusters of galaxies. However, at intermediate temperatures the ions are not completely ionized and some electrons are bound to the nuclei. Transitions between states of
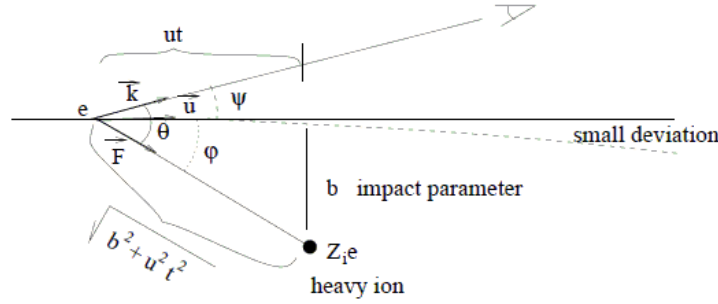
Figure 1.1 Schematic representation of the bremsstrahlung emission process.

the ion are therefore possible. These lead to lines and edges in the emission spectrum of the plasma.

The interaction (Fig. 1.1) occurs on a timescal $\Delta t \approx 2b/v$, where b is the impact parameter and v is the particle velocity. The emitted energy per unit of frequency in a single collision is inversely proportional to the square root of: the mass, the velocity of the deflected particle and the impact parameter. Indeed, the emission is:

$$\frac{dW}{dv} \approx \frac{16Z^2e^6}{3c^3m^2v^2b^2} \quad b << \frac{\nu}{\omega}, \tag{1.11}$$

while it is equal to zero for $b >> v/\omega$.

Integrating over the impact parameter, we obtain:

$$\frac{dW}{dv\,dt\,dV} = \frac{32\pi^2 Z^2 e^6}{3\sqrt{3}c^3m^2v}n_e n_i g_{ff}, \tag{1.12}$$

where g_{ff} is the Gaunt factor,

$$g_{ff} = \frac{\sqrt{3}}{\pi}\ln\left(\frac{b_{max}}{b_{min}}\right). \tag{1.13}$$

b_{max} and b_{min} must be evaluated taking into account quantum mechanics. g_{ff} is of the order of unity for large intervals of the parameters.

To get the final emissivity, the integration over the velocity distribution of the electrons in the macroscopic plasmas must be made. Since the emissivity is proportional to the square root of the density, thermal bremsstrahlung will therefore play a role whenever the densities are high. The velocity of

the electrons in thermal equilibrium follows a Maxwellian distribution. The thermal bremsstrahlung emission, in the optically thin case ($\tau << 1$), thus becomes:

$$\frac{dW}{dt} = f(T) \int n_e n_i dV, \tag{1.14}$$

with

$$f(T) = \frac{64\pi^2 Z^2 e^6}{3hc^3 m^2} \sqrt{\frac{2\pi k}{3km}} T^{-\frac{1}{2}} \overline{g}_{ff}, \tag{1.15}$$

where $\int n_e n_i dV$ is the emission measure and $\overline{g}_{ff}$ is a velocity averaged Gaunt factor. For further datials see [65]. The emission spectra will be flat at lower frequencies ($h\upsilon << kT$) with an exponential cutoff at higher ones ($h\upsilon >> kT$). In the optically thick case, we have the blackbody emission. Furthermore, the auto-absorption decreases with the increasing of υ. If the plasma is optically thin, the bremsstrahlung radiation leaves the plasma, carrying part of the internal plasma energy emitting as a blackbody. This effect is known as the bremsstrahlung cooling.

For any emission mechanism, the cooling time is defined as:

$$t_{cool} \equiv \frac{E}{|dE/dt|}, \tag{1.16}$$

where E is the energy of the emitting particle and dE/dt the energy lost by radiation. For thermal bremsstrahlung,

$$t_{cool} \approx \frac{6 \ 10^3}{n_e Z^2 \overline{g}_{ff}} T^{-\frac{1}{2}} \quad yr. \tag{1.17}$$

The cooling time is of order one thousand years for HII regions and of a few 10^{10} years for a cluster of galaxies.

Free-free absorption

It is the absorption of a photon by a free electron in the Coulombian field of an atom. Free-free absorption is the absorption mechanism corresponding to bremsstrahlung. For thermal electrons,

$$j_\nu^{ff} = \frac{dW}{4\pi \ d\nu \ dt \ dV} = \alpha_\nu^{ff} B_\nu(T) \tag{1.18}$$

$$\alpha_\nu^{ff} = \frac{8\pi Z^2 e^6}{3hc^3 m^2} \sqrt{\frac{2\pi}{3km}} T^{-\frac{1}{2}} n_e n_i \nu^{-3} (1 - \exp^{-\frac{h\nu}{kT}}) \overline{g}_{ff}, \tag{1.19}$$

where $B_\nu(T)$ is the blackbody radiation at the temperature T. At low frequencies, matter in thermal equilibrium is optically thick to free-free absorption (self-absorption), becoming thin at high frequencies.

1.4.4 Cyclotron and synchrotron emission

One of the most common non-thermal emission is synchrotron. It is produced by the acceleration of a moving charged particle in a magnetic field B due to the Lorentz force:

$$F = \frac{q}{c}(v \times B),$$ (1.20)

where v and q are the velocity and the charge of the particle.
The force F is always perpendicular to the particle velocity, so it does not do work. Therefore, the particle moves in a helical path with its axis parallel to the direction of the magnetic field. The radius of the gyration and the frequency of the orbit are:

$$r_B = \frac{\gamma m c v \sin \alpha}{qB} \qquad \omega_B = \frac{v \sin \alpha}{r_B} = \frac{qB}{\gamma m c},$$ (1.21)

where α is the angle between v and B.
Non-relativistic electron velocity ($\gamma \approx 1$) results in cyclotron radiation, while the relativistic particles ($\gamma >> 1$) produce synchrotron radiation. Synchrotron emission is often observed in the radio domain, but, in some extreme cases (such as in jets of blazars and in GRBs) it is seen up to the X and γ rays. Eq.1.20 shows that the acceleration is inversely proportional to the mass of the particle. Electrons therefore dominate the radiation in most situations: they move helicoidally at relativistic velocities inside a magnetic field emitting synchrotron radiation through a cone of half opening angle $1/\gamma$ in the direction of the motion.
For relativistic electrons, averaging over α, the power emitted by an electron is:

$$P = \frac{4}{3}\sigma_T c \beta^2 \gamma^2 U_B$$ (1.22)

$$U_B \equiv \frac{B^2}{8\pi} \quad \beta \equiv \frac{v}{c}.$$ (1.23)

The synchrotron spectrum from a single electron is peaked at:

$$v_0 = \frac{3\gamma^2 eB \sin \alpha}{4\pi m c}.$$ (1.24)

To get the total spectrum from a population of electrons, we must know their energy distribution.

1.4.5 Inverse Compton scattering

In a frame where the electron initially moves with relativistic speed and has an $\gamma m_e c^2$ energy much higher than the photon one, the photon energy is increased by a factor γ^2, so gaining a very large energy in the scattering. Inverse Compton scattering explains why X ray photons are often created by scattering of soft photons on hot relativistic electron plasma.

Inverse Compton scattering is a dominating radiative process shaping the spectra of accreting BH, NS and AGN. In the electron rest frame, the photon energy changes as:

$$E = \frac{E_0}{1 + \frac{E_0}{mc^2}(1 - \cos\theta)}. \tag{1.25}$$

The cross section is the Klein-Nishina [65]:

$$\sigma_{KN} = \sigma_T \frac{3}{4} \left[\frac{1+x}{x^3} \frac{2x(x+1)}{1+2x} - \ln(1+2x) + \frac{\ln(1+2x)}{2x} - \frac{1+3x}{(1+2x)^2} \right] \tag{1.26}$$

where $x \equiv E/mc^2$. At low energy, it behaves as σ_T.

Assuming an electron thermal distribution, the mean percentage energy gain of the photon is:

$$\frac{\Delta E}{E_0} = \frac{4kT - E_0}{mc^2}. \tag{1.27}$$

For $4kT > E_0$, the energy is transferred from the electrons to the photons, while for $4kT < E_0$ from the photons to the electrons.

Inverse Compton losses dominate when the energy density of the radiation field is larger than that of the magnetic field (Compton catastrophe). The cooling time is:

$$t_{cool} \approx \frac{(\gamma - 1)mc^2}{\frac{4}{3}\sigma_T c U_{rad}\gamma^2\beta^2}, \tag{1.28}$$

where U_{rad} is the energy density of the radiation field. The cooling time may be very short for relativistic electrons in a strong radiation field.

Chapter 2

Detectors for High Energy Astrophysics

When an astrophysical instrument is planned, the right detector must be chosen. Two main features must be taken into account: the problematics connected with the X and γ ray sky (seen in Chapter 1) and the different physical processes underlying the matter-radiation interaction.

This chapter briefly deal with the principal ways in which X rays interact with matter and with the main detectors able to detect them. Hard-X/soft-γ photons are detected by observing their effect on the detector material. The choice of the right detector depends on the X ray photon energy and on what we want to measure. This chapter will focus to semiconductor detectors, such as those employed in the IBIS/INTEGRAL telescope.

Until now, the best solution for image hard-X/soft-γ ray sources is by coded mask systems. To improve the sensitivity of a coded mask telescope, mainly limited by the high background radiation, another imaging possibility, but still in a development phase, is focusing optics. The last part of this chapter will shortly deal with the main focusing optics for X ray telescopes, while the following one will describe coded mask systems now used in hard-X/soft-γ ray energy band.

2.1 The matter-radiation mechanisms

The interaction of the γ ray radiation with matter causes three main phenomena: the photoelectic effect, the Compton scattering of free electrons and the pair production. Each of these processes is very complex, since there are secondary effects as the emission of Auger electrons and fluorescence radiation in the photoelectric effect or the emission of recoil electrons in the

scattering or, finally, the anihilation of positrons in pair production.

The influence of these emission mechanisms depends on the spectral region of the radiation and on the atomic number Z of the detector absorber material (see Fig. 2.1). The choice of the detector material must be made to best guarantee the detection of its energy for one of these emission mechanisms.
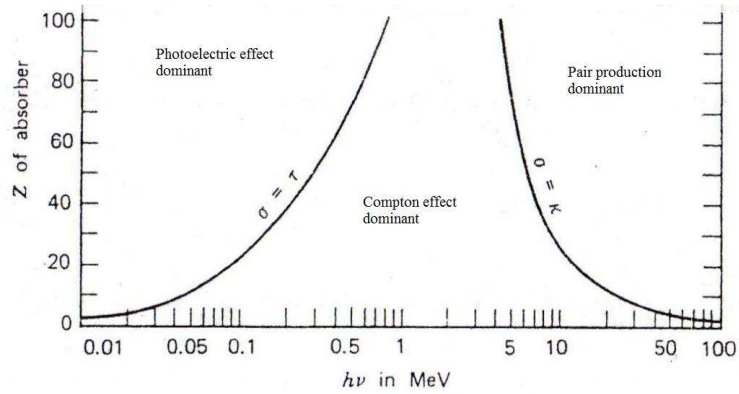
Figure 2.1 Importance of the three main mechanisms of radiation-matter iteration as a function of photon energy and atomic number Z of the absorbing material.

2.1.1 Photoelectric effect

In the photoelectric absorption the γ ray photon energy $h\nu$ is spent to remove one of the bound electrons from the absorber atom. This process can happen only if the γ ray has energy bigger than the electron binding energy E_B. This causes jumps in correspondence of the binding energy of the different shells in the absorption coefficient curve.

The kinetic energy of the resulting photoelectron, E_e, will be given by $E_e = h\nu - E_B$. The resulting atom is in an excited state and could expell the excess energy in two ways: with photon emission of energy close to the excess one, in which case we have X ray fluorescence. In alternative, the atom could emit another electron of energy equal to the excess one due to the electron redistribution in the atomic levels (Auger effect).

The probability of the photoelectric absorption is

$$\tau = kZ^n E_{h\nu}^{-3.5}, \tag{2.1}$$

where Z is the atomic number of the detector material and n assumes values between 4 and 5. For the same photon energy, materials with higher Z have higher photoelectric absorption.

2.1.2 Compton scattering

The Compton scattering (see Fig. 2.2) is the interaction of a photon of energy $h\nu$ with a bound electron of the absorbing material. The electron recoils in the direction ϕ, while the photon is scattered by an angle θ. Because the photon has lost energy to the electron, the photon energy has decreased. In this collision, both the momentum and the total energy are conserved. The change in energy of the scattered photon is very small, so Compton scattering is usually lumped together with Thomson scattering.
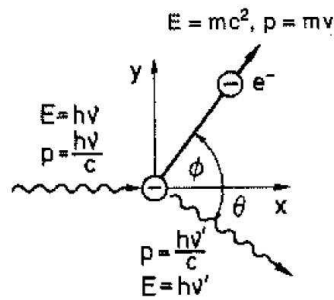
Figure 2.2 Schematic view of the Compton scattering.

The energy of the scattered electron depends on θ as

$$h\nu' = \frac{m_e c^2}{1 - \cos\theta + (\frac{1}{\alpha})} = \frac{h\nu}{1 + \frac{h\nu}{m_e c^2}(1 - \cos\theta)} \qquad (2.2)$$

where $m_e c^2$ is the rest energy of the electron (equal to $E_0 = 0.511$ MeV). The term $h/(m_e c^2)$=0.0243 A$^\circ$, called the Compton wavelength λ_c, is the characteristic change in the wavelength of the scattered photon. For $\alpha = h\nu/m_e c^2 >> 1$, the energy of the scattered photon verges to $m_e c^2/2$ for $\theta = 180^o$ and to 511 keV for $\theta = 90^o$.

For small θ, the kinetic energy of the scattered photon is about equal to the initial one, so the energy of the recoil electron $E_K = h\nu - h\nu'$ is zero. At 180°, the energy of the scattered photon is minimum and that of the recoil

electron is maximum, equal to

$$E_K = \frac{h\nu}{1 + \frac{2h\nu}{m_e c^2}}.$$
(2.3)

The probability of a Compton scattering depends on the number of target electrons, so it grows up linearly with Z. The angular distribution of the scattered photons is given by the Klein-Nishina formula (Eq.1.26).
For polarized photons, the cross section is given by [25]:

$$\frac{d\sigma}{d\Omega} = \frac{r_0^2}{2} \left(\frac{\nu'}{\nu}\right)^3 \left(\frac{\nu}{\nu'} + \frac{\nu'}{\nu} - 2\sin^2\theta\cos^2\eta\right),$$
(2.4)

where r_0 is the classic radius of the electron and η is the angle between the electric field of the incident photon and the azimuthal direction of the scattered photon at θ angle.
For not-polarized photons, instead, the cross section will be:

$$\frac{d\sigma}{d\Omega} = Zr_0^2 \left(\frac{1}{1 + \alpha(1 - \cos\theta)}\right)^2 \left(\frac{1 + \cos^2\theta}{2}\right)\left(1 + \frac{\alpha^2(1 - \cos\theta)^2}{(1 + \cos^2\theta)[1 + \alpha(1 - \cos\theta)]}\right),$$

where $\alpha = h\nu/m_e c^2$.

2.1.3 Pair production

The threshold energy for the pair production is the equivalent rest mass of the electron-positron pair ($2E_0 = 2m^2c^4 = 1.02$ MeV). This absorption mechanism becomes important at energies above 5 MeV.
In the Coulombian field of a detector nucleus, the γ ray photon disappears substituted by a $e^+ - e^-$ pair. All the photon energy in excess with respect to the pair rest energy becomes kinetic energy of the pair itself.
A simple expression of the pair production cross section does not exist. For photons of some MeV energy, we can say that

$$\sigma_{pp} \approx r_0^2 \frac{Z^2}{137}.$$
(2.5)

2.2 Detectors for high energy astrophysics

The principal issue when selecting a detector is to establish what you exactly want to measure. High energy detectors usually measure the energy and the arrival time of individual photons. In addition to this information,

the position of the detected photons is essential for imaging.

All detectors have to deal with background. The total X ray background has the same intensity level or it is higher than the source you want to measure. Thus, it is needed to separate source counts and background contribution and to minimize the last one. The employment of not focusing collimators in hard-X/γ ray telescopes restricts the telescope FOV but also blocks the background radiation coming from directions different from that of interest. The different types of detectors have different capabilities. If one wants to get accurate energy measurements for individual regions of a source with exact timing and a good ability to reject background counts, a large area detector with intrinsic energy resolution is needed. Instead, if one wants only excellent timing resolution (i.e. to tag each photon with a highly accurate arrival time), one wants to be able to perfectly distinguish the source from the overall sky. Lastly, if you want that electronics or read-out devices do not add any noise, it is better to transmit all the signals.

Most of the X ray detectors is based on the absorption (scattering) of incident photons in the detector material. The energy lost by the photon becomes energy of the electron. Depending on the energy of the photons to be detected, energy resolution and efficiency, the energy lost can be used to produce a cascade of electrons, so creating a signal proportional to the original photon one (as in proportional counters), to excite fluorescence states of the detector material, so producing a luminous signal proportional to the incident photon energy (as in scintillator detectors) or, finally, to create pairs in the solid state detectors.

Recently, for soft γ rays, calorimeters, i.e. detectors that measure the temperature variations associated to the photon absorption, are being developed. To get a very accurate measure of the X ray energy, they have to be cooled down to nearly zero Kelvin. These calorimeters are suitable to be used as focal plane detectors.

Gas detector: proportional counter

A proportional counter is a metallic box (that works as cathod) filled with gas and with one o more wires (anodes). A photon that crosses the gas, ionizes it creating electrons and free ions. Electrons are captured by the anode, producing an electric pulse. If the potential difference between anode and cathod is low, electrons could recombine themselves with ions. Instead, for a sufficiently high voltage, all the electrons are accelerated towards the anod, with energies able to ionize other atoms producing other electrons

Crystal	Z	Density (g cm^{-3})	Decay time (ns)	Light yield (ph/100 keV)	Wavelength of max emission (nm)
CsI(Na)	50-53	4.51	460	3900	420
NaI(Tl)	23-53	3.67	230	3800	415

Table 2.1 Properties of crystals used in hard-X ray detectors, data taken from [51].

(electrical current). Proportional counter is one of the most common X ray detectors used in recent X ray missions. With these detectors it is possible to measure energy, arrival time and position information.

Scintillation detector

Scintillation remains one of the most used methods for detection and spectroscopy of hard-X rays (> 15 keV) in a broad energy band. When a γ ray interact with the atoms and is absorbed, violet fluorescence is produced. The energy lost produces a transfer of electrons from the valence to the conduction band. To enhance the fluorecence during the de-excitation process (i.e. electron comes back to the valence band), small amounts of impurity, called activators, are commonly added to inorganic scintillators. Thallium and sodium are often used for this purpose. Well known and used scintillators are NaI(Tl) with a thallium activator and CsI(Na) with a sodium activator. Tab. 2.1 describes the properties of these crystals.

The scintillator is physically coupled to a photomultiplier tube. Its photocathode transforms the incident light signal into electrons. Electrons are multiplied by the dynodes. Since there is an electric field between dynodes, low-energy electrons are also accelerated. This current is then collected at the anode. Charge amplification is performed in a very linear manner, producing an output signal that remains proportional to the original number of photoelectrons.

2.2.1 Semiconductor Detectors

A newer technology has become more widespread since the late 1990's. Semiconductor detectors, as their name implies, are based on crystalline semiconductor materials. They are also referred as solid state detectors. Their basic operating principle is similar to gas ionization devices in which the medium is a solid semiconductor material. The interaction of the radiation creates $e^+ - e^-$ pairs which are then collected by an electric field. The advantage of the semiconductor is that the energy required to create a

pair is about 10 times smaller than that required for gas ionization. Thus the produced charge for a given energy is one order of magnitude greater resulting in the increasing of the energy resolution. Moreover, thanks to their greater density and atomic number, they have a bigger stopping power than gas detectors.

In a pure semiconductor crystal, the number of holes and that of electrons in the conduction band is equal. This balance can be changed by introducing a small amount of impurity atoms having one more or one less valence electron in their outer atomic shell. The quantity of dopant used is generally very small with typical concentrations being on the order of a few times 10^{-13} atoms/cm^3.

An example of solid state compound used to detect γ ray photons is Cadmium Telluride (CdTe). It combines relatively high atomic numbers (48 for Cd and 52 for Te) with a large enough bandgap energy (1.52 eV) to permit room temperature operation without cryogenic cooling, as instead germanium requires. The probability of photoelectric absorption per unit pathlength is rougly 4-5 times higher in CdTe than in Ge and 100 times larger than in Si for typical γ ray energies (E > 20 keV).

CdTe is used for the ISGRI/IBIS detector aboard the INTEGRAL satellite. Its energy resolution is 8 % at 122 keV. In Tab. 2.2 some features of CdTe and, for comparison, of silicon (Si) and germanium (Ge) are reported. Materials such as CdTe offer better energy resolution, less noise and better spatial resolution.

Using these materials as imager requires the employment of coded aperture masks or Compton scatter type configurations. This is another feature that these detectors have in common with scintillators.

Collecting area is important for the telescope sensitivity: the more radiation it can collect (that is, the larger its collecting area), the more likely it detects dim objects. Most of the advanced materials being considered for future missions have the problem that the crystals are small. It requires large arrays of these crystals to achieve collecting areas acceptable for high energy astronomy. Nevertheless, collection areas on the order of thousands cm^2 are achievable.

2.3 Observational limits of X ray telescopes

Most celestial sources have small angular dimensions, such as a point like source. In the case of extended sources as clusters of galaxies, it is useful to

Material	Z	Density (g cm^{-3})	Bandgap (eV)	Ionization E (eV/e-h pair)	Best Gamma Ray Energy Resolution (FWHM)
CdTe (300 K)	48/52	6.06	1.52	4.43	1.7 keV at 60 keV 3.5 keV at 122 keV
Si (300 K) (77 K)	14	2.33	1.12 1.16	3.61 3.76	400 eV at 60 keV 550 eV at 122 keV
Ge (77 K)	32	5.33	0.72	2.98	400 eV at 122 keV 900 eV at 662 keV 1300 eV at 1332 keV

Table 2.2 Properties of CdTe semiconductor, data taken from [51].

know the spatial distribution of the emissions. One of the most important requirements for X ray telescopes is angular resolution.

One limit to the maximum angular resolution achievable is given by the telescope response to coherent radiation. Indeed, the aperture of the telescope acts as a slit. If the X ray photon beam is coherent, we have the diffraction phenomena, for which the Rayleigh criterion is valid. This dictates that an extended source of wavelength λ could be partially coherent if its angular dimensions θ_s are shorter than the first angular minimum θ_T of the diffraction pattern of a telescope of aperture d, i.e.

$$\theta_s < \theta_T = 1.22\frac{\lambda}{d} \ rad \ = 251643\frac{\lambda}{d} \ arcsec. \tag{2.6}$$

For X rays of about 1 keV ($\lambda = 10$ A^o) and a telescope of diameter $d = 50$ cm, Eq.2.6 gives:

$$\theta_T^X = \frac{251643}{0.5} \ 10 \ 10^{-10} \approx 5 \ 10^{-4} \ arcsec, \tag{2.7}$$

i.e. only sources with $\theta_T < 5 \ 10^{-4}$ arcsec could be sources of coherent radiation. Theoretically, these telescopes would have a big angular resolution, but the instrument quality required is difficult to obtain.

Sensitivity of a direct-view telescope

The performance of an imaging telescope depends on its ability to reconstruct faithfully the fluxes from the FOV both in term of intensity and angular distribution. The Signal-to-Noise Ratio (SNR) determines the minimum source strength that may be detected in the observation time t, for which it's also called flux sensitivity.

Here the SNR equation in the case of non-focusing direct view detector is reported. This kind of detector can give sky images by means of coded masks or modulation collimators.

Given a flux intensity of photons, $I(E)$ (in units of photons cm^{-2} s^{-1} keV^{-1}) at energy E, coming from an X ray source, the number of events, N_{tot}, counted by the detector in the time interval Δt in the energy band ΔE around E can be expressed as the sum of the counts due to the photons from the X ray source and those due to the telescope background, $N_{tot} = N_S + N_B$. For a direct-view telescope, N_S and N_B are given by:

$$N_S = \epsilon_d S_d \Delta t I(E) \Delta E, \tag{2.8}$$

$$N_B = S_d \Delta t B(E) \Delta E, \tag{2.9}$$

where ϵ_d is the detector efficiency, S_d the detector area and $B(E)$ the intensity of the measured background spectrum (in units of cts cm^{-2} s^{-1} keV^{-1}) at energy E.

The information on the source is contained in N_S and can be derived subtracting from the total counts the background counts, i.e. $N_S = N_{tot} - N_B$. Therefore, the standard deviation of the counts due to the source is:

$$\sigma_{N_S} = \sqrt{\sigma_{N_{tot}}^2 + \sigma_{N_B}^2}, \tag{2.10}$$

where $\sigma_{N_{tot}}^2$ and $\sigma_{N_B}^2$ are the standard deviations of N_{tot} and N_B, respectively. This expression is valid if the fluxes from the source and from the background are uncorrelated.

In the γ ray energy band, the source signal is much smaller than the instrumental noise and so, in the evaluation of the sensitivity, it is usually assumed that the number of counts is dominated by the background ($N_S << N_B$). Using Poissonian statistics, we have $\sigma_{N_{tot}} = \sqrt{N_{tot}}$ and $\sigma_{N_B} = \sqrt{N_B}$, so:

$$\sigma_{N_S} = \sqrt{(N_S + N_B) + N_B} \approx \sqrt{2\sigma_{N_B}^2} = \sqrt{2B(E)S_d \Delta t \Delta E}. \tag{2.11}$$

The confidence level chosen for the sensitivity is generally 99.7%, corresponding to a number of standard deviations (n_σ) of 3. Thus, the minimum detectable source flux is:

$$N_S^{min} = \epsilon_d S_d \Delta t I_{dv}^{min}(E) \Delta E = 3\sqrt{2B(E)S_d \Delta t \Delta E} \tag{2.12}$$

from which the sensitivity results to be

$$I_{dv}^{min}(E) = \frac{3}{\epsilon_d}\sqrt{\frac{2B(E)}{S_d \Delta t \Delta E}}. \tag{2.13}$$

More in general, the ratio between the source signal and its error is:

$$n_\sigma = \frac{N_S}{\Delta N_S} = \frac{\epsilon_d I_{dv}^{min}(E) S_d \Delta t \Delta E}{\sqrt{2B(E) S_d \Delta t \Delta E}}. \tag{2.14}$$

Thus, at any n_σ level the sensitivity of a direct-view telescope is given by:

$$I_{dv}^{min}(E) = \frac{n_\sigma}{\epsilon_d} \sqrt{\frac{2B(E)}{S_d \Delta t \Delta E}}. \tag{2.15}$$

The easiest way to improve the instrument sensitivity is to decrease the background and to increase the value of the detector area S_d. However the sensitivity dependence on S_d implies that the minimum detectable intensity decreases by a factor of 10 when the detector surface increases of a factor of 100.

Great progress from this class of instruments is hard to foresee. The development of new deconvolution techniques could improve source location and flux estimation accuracy.

Chapter 4 will deal with the IBIS/INTEGRAL sensitivity estimation. In real cases, the background cannot be measured independently from the source signal, so other ways to estimate the SNR in coded mask systems will be used.

2.4   Focusing optics for X rays

The main problem with instrumentation employing inelastic interactions (like coded mask ones) is the high background level. Since the collection area has the same size as the detector and the instrument sensitivity is proportional to it, building any coded mask instrument with high sensitivity is difficult. A compact instrumentation is preferred. This section will deal shortly with the alternative approach represented by focusing techniques.

The currently employed focusing optics for X rays are based on the total reflection technique. However this technique becomes inefficient for photon energy greater than 10-20 keV. Other techniques, such those based on the diffracting optics in Laue configuration which take advantage of the progress made in crystal production, are under development.

X rays will reflect off mirrors only if they strike at grazing angles. For this reason, X ray mirrors have to be carefully shaped and aligned nearly parallel to the incoming X rays. To increase the collection area and the sensitivity of the telescope, they are nested one inside the other.

The use of X ray optics based on total reflection has already been exploited since the late seventies for photon energies below 2 keV (Einstein satellite). All materials with high atomic number are efficient X ray reflectors when the grazing incidence angle is lower than a critical angle θ_C,

$$\theta_C = \sqrt{2\delta} = \sqrt{4\pi r_0 \lambda^2 N_e}, \tag{2.16}$$

where δ is equal to 1 minus the real part of the reflective index n_r, λ is the wavelength of the incident radiation, $r_0 = e^2/mc^2$ is the classical electron radius and N_e is the electron density of the material [3]. The reflection efficiency is nearly the 100% for angles lower than θ_C, but steeply drops to zero for larger grazing angles.

The critical angle is inversely proportional to the photon energy: to reflect high energy photons, a smaller grazing angle is needed. Furthermore, θ_c depends on the electron density, that is approximately the atomic number of the surface material: a better reflection needs high Z material. The most commonly used reflecting materials for X ray mirrors are gold (used for Suzaku, XMM, Beppo-SAX and Swift satellites) and iridium (for Chandra X ray Observatory).

Usually, to limit coma aberrations and to have a greater compactness, special mirror geometries are adopted. To be free from coma aberration, high energy optics must obey to the Abbe condition, i.e. the intersection of the direction of the incident rays and that of the reflected ones must be on a spherical surface around the image. The most used configuration correcting off-axis aberration is the Wolter I [87] [88], i.e. two coaxial and confocal mirrors, one with the shape of a parabola and the other with that of a hyperboloid (Fig. 2.3). It has been used for example in the Beppo-SAX satellite.

However, the efficiency of this type of optics is acceptable only until about 10 keV. It is hard to think that the use of new materials can extend the energy band of the total reflection technique above the 10 keV limit. The only solution with this technique could be increasing the focal length of the mirrors, as was proposed for SIMBOL-X, whose focal length is 30 m [31]. Hovewer its sensitivity above 70 keV decreases to values achievable with the direct-view telescopes.

With this necessity of a significant sensitivity improvement at energies above 10 keV, the employment of Bragg diffraction appears the most promising technique to focus high energy photons. Multilayers mirrors (NuStar,
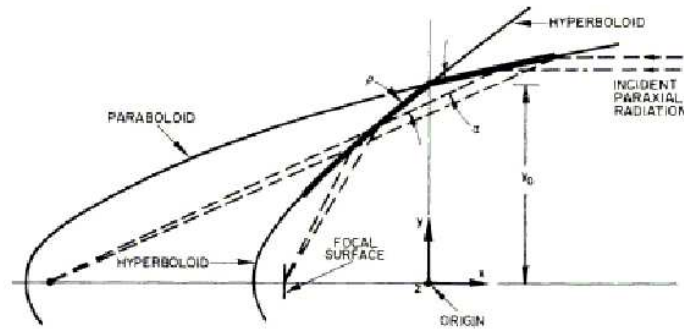
Figure 2.3 Wolter I configuration.

NeXT) for focusing X rays up to 80 keV [48] and mosaic crystals in reflection configuration [32] could be used. However, for photon energies greater than 100 keV, very large mirror surfaces and very long focal length are required in order to achieve significant effective areas to be competitive with direct-view detectors.

Laue lenses appear to be the best solution to efficiently focus high energy X rays (> 80 keV) and to overcome the weight and size problems of direct-view telescopes. The concept that stands behind a Laue lens is that a properly distribution of mosaic crystals in transmission configuration allows the incoming photons to be concentrated.

The X ray diffraction theory shows as with a mosaic of small crystals it is possible to deviate X ray photons. Using a set of mosaic crystals it is possible to create a Laue lens which is able to deviate, through diffraction, photons towards a focal point. A detailed description of Laue lenses goes beyond the scope of this thesis. More details can be found in [89], [90] and [63].

Chapter 3

Coded Mask Telescopes

The previous chapter briefly describes focusing telescopes. The main alternative imaging technique is the multiplexing technique. It offers the opportunity to image at higher energies and over a large FOV. It is based on the encoded signal of the incoming photons before their detection and the reconstruction of the sky image by decoding the encoded data.

Multiplexing techniques can be of temporal or spatial type. One subclass of spatial multiplexing techniques is the coded-mask system. At the beginning of the 1990s, the Chinese scientist T.P.Li and his collaborators proposed the DD deconvolution technique to deconvolve HXMT data. It is a general inversion method which uses non linear iterative algorithms to solve the underlying optimization problem. The DD can be used to deal with the observational data by various types of space telescopes, amongst which the coded mask ones. Since our LR code was tested on the coded mask data of the IBIS imager, this chapter will discuss the imaging technique of coded mask systems.

A short view on HXMT temporal modulation collimators and the detailed description of the IBIS/INTEGRAL satellite will be given in Chapter 4.

3.1   Principles of Coded Mask Imaging

Coded aperture imaging in high energy astrophysics represents an important advancement in X and γ ray instrumentation, where other imaging techniques become ineffective or not suitable to achieve the observational goals (e.g. imaging over wide FOV).

Coded mask systems can image the sky from a few keV until few MeV. They basically consist of a coded mask, i.e. a plate with transparent and opaque elements, and a PSD. Mask elements have equal size and shape and are dis-

tributed in a pre-determinated pattern. Two very sucessful basic patterns, the Uniformly Redundant Array (URA) and Modified URA (MURA), will be discussed in Sects.3.2.1 and 3.2.2.

Coded masks are an extension of the pinhole camera concept. Photons from a certain direction in the sky project the mask pattern on the detector. This projection, called the shadowgram, has the same coding as the mask pattern, but it is shifted depending on the photon direction. The PSD pulse distribution gives the sum of the patterns corresponding to each of the sources in the FOV. Every source is encoded in a unique way. Fig. 3.1 shows an outline of the coded-mask system working principle. The basic requirement is that the autocorrelation function would consist of a single peak and flat sidelobes.
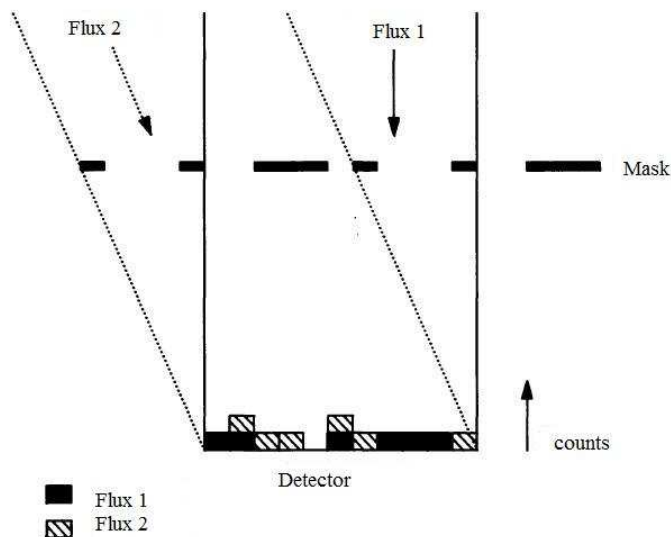
Figure 3.1 A schematic diagram illustrating the working principle of a coded mask telescope. The recorded count rate in each pixel of the detection plane is the sum of contributions from each source flux modulated by the mask. In particular, the shadow generated by two sources at infinite distance from the mask-detector system - one on axis and the other at the edge of the FOV- are shown. Taken from [15]

Coded mask systems allow simultaneous measurement of the source plus background flux (detector area throught the mask holes) and of background flux (detector area blocked by the mask opaque elements) alone.

The mask and the PSD of a coded mask telescope can have several configurations, depending on their relative dimensions (i.e. the mask and the PSD

of the same dimensions or the PSD is larger than the mask or the mask is larger than the PSD). What changes between these configurations is the FOV. The configuration in which the mask is larger than the PSD allows for larger FOV: this is that used in IBIS/INTEGRAL. It allows for the use of smaller detectors, thus limiting the γ ray background detection.

The FOV consists of two distinct regions: a Fully Coded Field of View (FC-FOV), where the detected flux is completely modulated by the mask, and a Partially Coded Field of View (PCFOV) or vignetted FOV, in which only a fraction of the detected photons is coded by the aperture pattern (see Fig. 3.2).
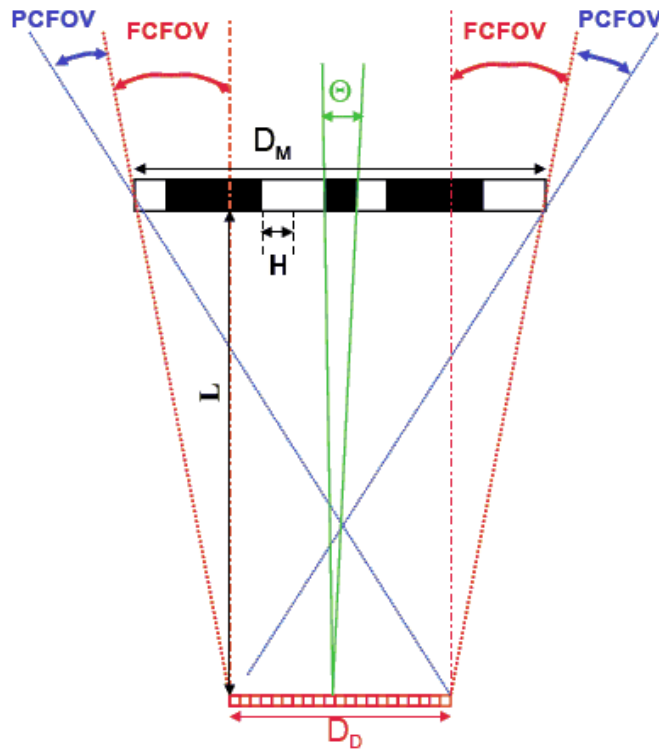
Figure 3.2 The FOV of the IBIS/INTEGRAL. Opaque and transparent elements have constant size H and pixel size is less than mask element one. Here D_M and D_D are mask and detector dimensions, and $D_D < D_M$. L is the fixed mask-ISGRI distance. Taken from [36].

An important aspect of direct-view imaging systems such as coded mask telescopes is the fact that the Poisson noise from any source in the sky is induced at any other position in the reconstructed sky. The quality of the reconstructed image is mainly determined by the choice of mask pattern and

decoding method, in addition to the optical design of the camera and the spatial response of the detector.

In the following, the image formation and reconstruction using a coded mask system will be discussed.

3.1.1 The IBIS/INTEGRAL optical design

Fig. 3.2 shows the optical design chosen for the IBIS/INTEGRAL telescope. The optical design of a coded mask system concerns the choice of the mask size ($D_M = 1064$ mm), the size of the mask and detector elements ($H = 11.2$ mm and $s_d = 4.6$ mm, respectively), the number of basic patterns used in the mask, the mask-detector distance ($L = 3200$ mm) and the size and shape of an optional collimator. The design establishes the angular resolution and the FOV of the imaging telescope. The nominal angular resolution (FCFOV) of the IBIS imager is 12' [36], deduced by the mask element size, while ISGRI pixel size corresponds to 5'.

To make use of all detector area and to allow more than one source to be fully coded, the mask basic pattern of the IBIS imager is taken as the same size and shape as the PSD. The aperture is a 2×2 cyclic repetition of the basic mask pattern, with 11 rows and 11 columns excluded, in order to eliminate the cyclic nature of the PSF. This configuration and the choice of a MURA of order 53 as basic pattern allow to have a sidelobe-free response, given that a source casts an entire basic pattern on the detector. These physical characteristics define a FCFOV and a PCFOV of [36]

$$\Theta_{FC} = \arctan \frac{D_M - D_D}{L} = 9^o \times 9^o \qquad (3.1)$$

$$\Theta_{PC} = \arctan \frac{D_M + D_D}{L} = 29^o \times 29^o. \qquad (3.2)$$

The IBIS/INTEGRAL arrangement provides a wider FOV without loss of angular resolution and a uniform sensitivity over the FCFOV because the overall transparency of the working zone (i.e. the part of the mask that constributes to the coding on the PSD) for each direction is constant. However, in the PCFOV the sensitivity decreases. For poor SNR sources this implies a very significant advantage, even if the major constraints on the final telescope's sensitivity and resolving power are determined by the detector background and position sensitivity.

3.2   Mask Pattern

As discussed above, the choice of mask pattern has a basic role in the quality of the image deconvolution. Here two of the very successfully basic patterns applied in X and γ ray astronomy will be discussed: the URA and a their modification, the MURA.

In 1968 Dicke proposed an extension of the pinhole camera, based on an aperture composed by multiple holes into an opaque plate, with 50% total transmission. To have the best imaging quality possible, two conditions must be satisfied: the autocorrelation of the mask pattern should be a single peak with no sidelobes and the SNR of the coded sky source should be maximized. To have a good sensitivity, the open area of the plate could be increased, while preserving the angular resolution by placing many pinholes in the plate. Nevertheless, the autocorrelation of a random matrix as that suggested by Dicke, does not have flat sidelobes. The URAs and the MURAs, derived on quadratic residue sets, guarantee perfectly flat sidelobes. For further details see [29].

3.2.1   Uniformly Rendundant Array

The URAs are able to optimize the sensitivity in the restored images independently of the decoding method used. They belong to the family of cyclic difference sets array [4] (see Appendix A for their definition).

The cyclic autocorrelation function of the binary sequence produced by cyclic difference sets is always a single peak on a perfectly flat background. The uniform redundancy of the pattern is a translational property and guarantees that the shadow pattern cast by a source is unique to that source.

Among the cyclic difference sets the Hadamard sets class is particularly suitable for creating coded masks. A quadratic residue set is a class of Hadamard sets characterized by optimum SNR and about half open mask pattern. Once the binary sequence has been generated, if its length N can be factorised into a product of two integers ($N = p \times q$), it is possible to construct a two-dimensional array from the URA. The mask pattern thus arranged is called basic pattern, from which the aperture of a coded mask telescope could be created. To preserve the features of the autocorrelation function, basic patterns must be orthogonal each other. Since applying a cyclic shift to the elements of any array built from a URA we find again a URA, the URA autocorrelation characteristic is fulfilled if every $p \times q$ section is a cyclic shift of the basic pattern.

These mask designs are suited for use in the 2×2 mosaic form: a complete cycle of the basic pattern must be recorded for each sky direction to preserve optimum property of image reconstruction. For instance, this could be achieved with a mosaic mask of 2×2 cycles of the $(2p - 1) \times (2q - 1)$ basic pattern and a $p \times q$ PSD and, as a consequence, FCFOV.

In the high energy band it is impossible to have the transparent elements completely open. However, to minimize the absorption of photons, an isolated opaque element is mounted on a support grid. This does not affect the ideal autocorrelation characteristic, even if the open area is decreased somewhat, resulting in less sensitive area.

3.2.2 Modified Uniformly Redundant Array

The MURA (Modified URA) derives from the quadratic residue arrays, developed by Calabro and Wolf in 1968 [13]. Although the MURA arrays are derived from quadratic residues, they do not belong to the cyclic difference sets and, consequently, are constructible in configurations forbidden to that design. At the end of the 90's, Gottesman and Fenimore [38] proposed their imaging application: nowadays MURAs are implemented, for instance, on the IBIS/INTEGRAL.

A MURA basic pattern is a square array of side p, with a total number of elements equal to p^2. For details on their construction technique, see [38] and the references therein. Using this approach, the MURA is equals the URA in imaging performances.

An interesting feature of these patterns is their symmetry: square MURAs are invariant to 180° rotations around their central element. This property may offer advantages in the physical construction of the apertures.

All MURAs have complementary patterns (which are MURAs) that are built from the original pattern by complementing every element in the array except the initial one.

The MURA's superior imaging capability originates from the fact that G, the correlational inverse of M, is in fact the aperture pattern itself (see [26]). The unimodularity of G ensures that all pixels intensities S_{ij} will contribute in the same manner to the noise: the optimum SNR (Eq. A.9) will be independent from the source structure.

The sensitivity formula for MURAs agrees with the expression derived for the URA in [26]. Since in this derivation it was only required that G was unimodular, this SNR formulation is valid for any aperture with a unimodular decoding function.

MURAs perform as well as URAs, since both apertures have the same amount of open area ($(p^2 - 1)/2p^2 = 50\%$). In the typical conditions of high energy astronomy (few point sources and high background), MURA guarantees the optimum transparency. MURA therefore offers the minimum statistical error in condition of high background and avoids the systematic term due to the cross-talk between sources in the FOV.

Finally, they are suited for use in the mosaic form. Indeed, as will be seen in the next chapter, the IBIS mask is a mosaic of 2×2 MURAs of order 53.

3.3 Imaging using a mask

Let's assume a sky source with photon intensity distribution $f(\vec{x})$ in the object space $\vec{x}$ incident to an instrument. Due to the properties of the detection system, photons are modulated giving rise to a distribution $d(\vec{\omega})$ in the image space $\vec{\omega}$. The detector PSF is the function that transforms $f(\vec{x})$ into $d(\vec{\omega})$.

The detected image is then degraded with respect to the object. Two sources of degradation can be roughly distinguished: the process of image formation and that of image detection. The degradation due to the first process is usually denoted by blurring, while that introduced by the second one is denoted by noise. While blurring is deterministic and, in most cases, one has a sufficiently accurate mathematical model for its description, noise is a statistical process so that one can, at most, assume a knowledge of its statistical properties.

To reconstruct the observed sky in the object space, several deconvolution algorithms are used. Their choice depends on the specific aim and on the type of instrument configuration. This section gives a description of the classical way to deconvolve coded mask images. It is the cross-correlation technique between the shadowgram D and a decoding array G derived from the mask pattern.

A correlation $(f \star g)$ is identical to a convolution $(f * g)$ plus a reflection:

$$f \star g = f(t) * g(-t) = f(-t) * g(t), \tag{3.3}$$

where f and g are real-valued functions and $g(-t)$ and $f(-t)$ are the time-reversed of $g(t)$ and $f(t)$ respectively. While the convolution involves the reversing of a signal, its shifting and multiplication times another signal, the correlation only involves its shifting and multiplication (no reversion).

The discrete convolution is defined as:

$$d_{mn} = (f * P)_{mn} = \sum_{k=0}^{M-1} \sum_{l=0}^{N-1} P_{kl} f_{m-k,n-l}, \tag{3.4}$$

where $f, P \in \Re^{M \times N}$.

In coded mask systems (see Fig. 3.3), the discrete spatial cross-correlation is defined as:

$$d_{mn} = (f \star P)_{mn} = \sum_{k=0}^{M-1} \sum_{l=0}^{N-1} P_{kl} f_{m+k,n+l}. \tag{3.5}$$
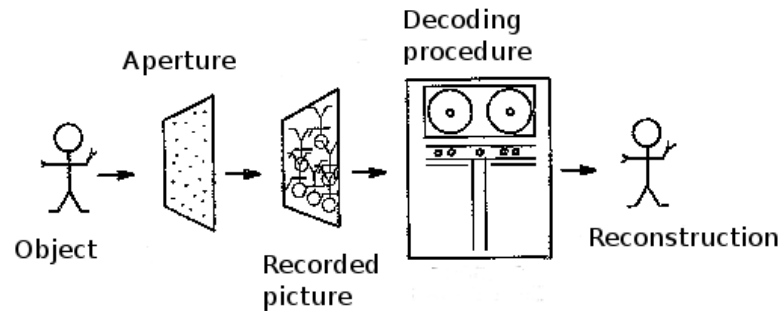
Figure 3.3 Schematic illustration of the basic procedure for coded aperture imaging. Taken from [28].

The cross-correlation is not commutative as is the convolution operation. If either f or P is an even function, cross-correlation and convolution are identical operations since flipping an even function before the convolution has no effect.

Let introduce the following important property of the cross-correlation and deconvolution operations. The cross-correlation of the convolution of f and h with a function g is the convolution of the correlation of f and g with the kernel h:

$$(f * h) \star g = h(-) * (f \star g). \tag{3.6}$$

It is clear as the imaging formation and reconstruction processes can be equivalently described either by convolution or by cross-correlation. For further details see [30], [47] and [23].

The standard method to reconstruct the true distribution of the source

intensity in coded mask systems is the cross-correlation.

In the following, the correlation operator will be employed to describe the image formation process. This guarantees that the reconstructed image is the actual distribution of the intensity in the source rather than a reflected version [30].

3.3.1 Image creation process

Imaging with coded masks is a linear process. The image formation equation relating the data to the object can be written as

$$\int p(\vec{\omega}, \vec{x}) f(\vec{x}) d\vec{x} + b = d(\vec{\omega}), \tag{3.7}$$

where $p(\vec{\omega}, \vec{x})$ is the modulation function, i.e. the response coefficient of the instrument to a point $\vec{x}$ of the object space during an observation $\vec{\omega}$. In general, it depends on the location of the source. The background term b is, in first approximation, constant.

For detection system made of a PSD, the data space $\vec{\omega} = \vec{x'}$ corresponds to the object space $\vec{x}$. Thus the data $d(\vec{x'})$ is the image of the object $f(\vec{x})$. If the modulation function is space-invariant, it is a function of the difference of $\vec{x} - \vec{x'}$, i.e. $p(\vec{x'}, \vec{x}) = p(\vec{x'} - \vec{x})$. Then Eq.3.7 can be written as a convolution

$$\int p(\vec{x'} - \vec{x}) f(\vec{x}) d\vec{x} + b \equiv p * f + b = d(\vec{x'}). \tag{3.8}$$

The effect of the detection process is the addition of a noise contribution to data and background mean values, i.e. $d = \bar{d} + n$ and $b = \bar{b} + n$.

The detector information is recorded as the number of photons interacting in each detector pixel during the measurement. The discrete nature of the data lends itself to a convenient representation as a bidimensional matrix D with elements D_{ij} representing the number of counts registered in the (i, j)th detector pixel. The aperture M is described by a matrix of 1 (transparent) and 0 (opaque to the incoming radiation) elements so it may be considered as a series of step functions.

The coded image D will be the convolution of the sky image S with M plus an unmodulated signal-independent background term B:

$$D = S * M + B, \tag{3.9}$$

or, in the discrete form,

$$D_{kl} = \sum_i \sum_j S_{ij} M_{i-k,j-l} + B_{kl}, \tag{3.10}$$

where sums are extended up to the limit of the FOV.

The object distribution inside the FOV is represented by the matrix S. Each element of S has angular sizes given by the theoretical angular resolution of the instrument, i.e.

$$\Delta\alpha \approx \arctan\frac{H}{L}, \tag{3.11}$$

where $\Delta\alpha$ in the angle subtended by one mask element at the detector.

Dividing the object space in q bins, for p observed values d_i, $i = 1, \ldots, p$, the coded process of Eq.3.10 may be expressed in terms of a linear system of algebraic equations [15]:

$$d = Pf + b, \tag{3.12}$$

where d, f and b are respectively p, q and p arrays obtained by a lexicographic reordering of D, S and B, while the $p \times q$ matrix P has the block Toepliz form (i.e. each descending diagonal from left to right is constant, $P_{ij} = P_{i-1,j-1}$). The matrix P contains the characteristic pattern of the mask cyclically shifted.

In general, since it is quite common to process images of the order of several mega-pixels, this is a large scale problem. The following chapter will deal with this formulation of the image formation equation. It will be seen how non linear numerical analysis can help to deconvolve sky images overcoming some of the problem with which the CC deconvolution deals.

3.4   Image reconstruction process

The image reconstruction process consists in the removal of all corruptions induced by the image formation and detection processes. An inversion technique solves the Eq.3.9, i.e. demodulates the detected image to reconstruct the object S. In the cross-correlation method, an estimate of the object S can be obtained by demodulating the shadowgram D with a suitable decoding function G:

$$\widehat{S} = D \star G = (S * M) \star G + B \star G, \tag{3.13}$$

and using the property in Eq. 3.6,

$$\widehat{S} = R(S) * (M \star G) + B \star G = S * R(M \star G) + B \star G, \qquad (3.14)$$

where R is the reflection operator. In the last equality the following property of the convolution operation is used:

$$\overline{(f * g)} = \overline{f} * \overline{g}. \qquad (3.15)$$

The image quality depends on the choice of the aperture M and this affects the properties of G. To guarantee that the reconstructed sky $\widehat{S}$ is perfect, the mask M and, as consequence, the decoding array G, must be chosen in such a way that the correlational inverse G is $M \star G = \delta$, where δ is the delta function. In this case, Eq.3.14 will be

$$\widehat{S} = S * \delta + B \star G = S + B \star G. \qquad (3.16)$$

$\widehat{S}$ differs from S only by the $B \star G$ term, which, for a flat and uniform array B is a constant level that can be measured and removed. Moreover, the background depends on the energy and the position on the detector.

Coded masks based on MURA arrays exhibits this ideal behaviour. Futhermore, square MURAs are invariant to 180° rotations around the central element, the R operator disappears, so reconstructing by convolution is equivalent to reconstruct by correlation.

The cross-correlation distribution $\widehat{S}$ of the data is only an image of the object intensity distribution, ignoring the information included in Eqs.3.13 and 3.9. Indeed, there may exist regions with negative $\widehat{S}$, called sidelobes, even if the object is defined only in a positive space.

Decoding with a weighting array G is termed balanced cross-correlation due the different weight given to opaque elements of M. Various weighting techniques exist. An example is the decoding array G with same dimension as the mask built in such a way that:

$$G_{jk} = 1 \;\; if \;\; M_{jk} = 1,$$
$$G_{jk} = \frac{\tau}{(\tau - 1)} \;\; if \;\; M_{jk} = 0 \qquad (3.17)$$

where the weight $\tau = \alpha/N$ is the overall transparency of the mask basic pattern, α is the number of pixels corresponding to a transparent element and N the total number of elements in the basic pattern. In this way, the sum

of the G elements is equal to zero, so any d.c. background is automatically removed by the reconstructed image [26].

MURAs have the remarkable property that their cyclic autocorrelation gives a delta function. For them, and then for the IBIS/INTEGRAL, G is a square matrix with odd dimensions defined by $\rho = 0.5$, so Eq. 3.17 becomes $G = 2M - 1$ (i.e., $G = +1$ for $M = 1$, $G = -1$ for $M = 0$) apart from the central element which is set to 0. This choice allows to reproduce the suorce distribution superimposed on a positive d.c. background level.

Applying to G the same reordering method used to construct P from the mask pattern, the bidimensional estimate $\widehat{S}$ of Eq.3.16 is derived by:

$$\widehat{f} = \overline{P}d = \overline{P}Pf + \overline{P}Pb, \tag{3.18}$$

where $\overline{P}$ is a $p \times q$ block-Toepliz-like matrix built from G. In the case of balanced cross-correlation $\overline{P}$ takes the form

$$\overline{P} = (1 + \rho)P^T - \rho U, \tag{3.19}$$

where U is the unit matrix and ρ is the ratio between the number of transparent and opaque elements (i.e. $\rho = \alpha/(N - \alpha)$). The absolute value of the elements of $\overline{P}$ is always 1 or ρ.

3.4.1 Ghosts and coding noise

The deconvolved image of a point source in the FCFOV has a main peak at the source position, flat sidelobes in the FCFOV and coding noise with up to 8 main false peaks, called "ghosts", in the PCFOV. For a PCFOV point source, other than the main peak at the source position and up to 5 ghosts, coding noise can extend all over the total FOV. The distribution of the coding noise depends on the mask pattern used. For instance, for MURA masks, due to the high degree of simmetry along the axes of the mask, the coding noise is concentrated along the image axis passing through the source peak, producing positive and negative sidelobes [39].

Ghosts are due to mosaic nature of the aperture. For example, the IBIS mask is a 2×2 cyclic repetition of a MURA basic pattern, with 11 rows and 11 columns excluded. A peak in the decoded IBIS image is, in general, consistent with at most nine different locations of the object responsible for this excess. Only one of these corresponds to the source position while the others are located at distances from the source which are multiple of the

basic pattern. In IBIS total FOV images, ghosts are located at distance of

$$\frac{53 \; pxl \times 11.2 \; mm}{4.6 \; mm} \approx 129 \; pxl. \tag{3.20}$$

Four of them are at the corner of the square of 258 pixels-side with the source at the centre, while the other four along the vertical and the horizontal axes passing through the source. In the cross-correlation ghost intensity is the same intensity of the source and their location follows always this distribution.

Balanced cross-correlation

Cross-correlation is able to reconstruct sources in both the FCFOV and the PCFOV. The balanced cross-correlation [29] is an extension to the PC-FOV of the standard technique. The sampling of the decoding array G is performed in such a way to weight the detector pixels with the fraction of transparent and opaque area projected by the mask elements. The correlation is balanced in the sense that, in absence of sources and with a constant background term, the decoded images are flat.
The sky image S is derived from D by applying the following operation for each (i, j) sky pixel [39]:

$$S_{ij} = \sum_{kl} G^+_{i+k,j+l} W_{kl} D_{kl} - b_{ij} \sum_{kl} G^-_{i+k,j+l} W_{kl} D_{kl}, \tag{3.21}$$

where the sums run over all k, l detector pixels. The balance array is

$$b_{ij} = \frac{\sum_{kl} G^+_{i+k,j+l} W_{kl}}{\sum_{kl} G^-_{i+k,j+l} W_{kl}}. \tag{3.22}$$

The two decoding arrays G^+ and G^- are obtained projecting the mask (M) and the antimask $(1 - M)$ arrays over a detector pixel grid and padding the zones outside the them with zeros. In this way, the statistical error at the source position and the significance of the ghost peaks are minimized. In the FCFOV we obtain the same result as the standard cross-correlation.
The weighting array W is used to weight properly the detector array before correlating it with G^+ and G^- arrays, in order to consider effects such as satellite drift corrections, dead areas or other specific conditions. It is set to 0 for dead and noisy pixels and to 1 for the active good ones.
In the FCFOV the variance is approximately constant and equal to the total number of counts on the detector. In PCFOV this is no longer true, so it is

computed accordingly to [36]

$$V_{ij} = \sum_{kl} \left(G^+_{i+k,j+l} W_{kl} \right)^2 D_{kl} + b^2_{ij} \sum_{kl} \left(G^-_{i+k,j+l} W_{kl} \right)^2 D_{kl}. \qquad (3.23)$$

Obviously, the variance behaviour affects also the sensitivity in the PCFOV. The values computed in Eqs.3.21 and 3.23 are then renormalized such that the intensity images are in units of cts s^{-1}.

Hint to other decoding procedure

When mask elements are larger than the detector pixels as in the IBIS case, G must be resampled to the detector pixel size by projection and redistribution of its values before deconvolving. For non integer sampling of pixel elements, G will assume continuous values from -1 to 1. In this way, the finite spatial resolution and the not correct binning of the mask elements are taken into account.

Unless the source is just in the middle of the sky pixels, the reconstructed peak will be spreaded over different detector elements and there is a loss of efficiency, called imaging loss. To reduce it, the detector must have spatial resolution better than the mask element size. PSD pixels, that give the resolution, over-sample the mask elements, so in this case the decoding can take the form of:

- Fine cross-correlation. While in balanced cross-correlation each transparent element is represented by one resolution element in the decoding array, in the fine cross-correlation more samples per resolution element are required to form G, M and S matrices. All sub-pixels of a resolution element have the same value as the corresponding original array.

- Delta-decoding. It is similar to fine cross-correlation, with each sub-pixel of a resolution element in G set to 0 expect for one set to 1 or -1. For further details see [27].

For further details about these decoding techniques, see [29] and references therein.

Chapter 4

Non-focusing Imaging Satellites

Sect.2.4 shortly dealt with focusing optics for X ray telescopes. The main alternative for hard-X/γ rays imaging is the multiplexing technique.

Multiplexing technique can be of temporal (as in the High Energy instrument aboard of HXMT) or spatial type (as in the IBIS/INTEGRAL). At the beginning of the 1990s, the Chinese scientist T.P.Li and his collaborators proposed the DD deconvolution technique to deconvolve HXMT data. Thank to its versatility, it has been used to analyze data from various type of space telescopes.

After a short description of the HXMT temporal modulation passive collimators, this chapter will deal with the IBIS/INTEGRAL coded mask telescope. Chapter 7 will show the results of the application of the LR method to the data provided by the ISGRI detector of the IBIS/INTEGRAL imager.

4.1   Modulation collimators

Passive collimators are principally employed in X ray (> 10 keV) energy band, where photon focusing techniques are still under development. They are composed by rectangular or square cells of height h. The cell walls are made of a material that absorbs X ray radiation crossing the walls.

The High Energy (Fig. 4.1) instrument aboard HXMT uses non-position-sensitive collimated detectors to realize high sensitivity and high resolution hard-X ray imaging surveys. The HXMT detector consists of 18 identical cylindrical NaI(Tl)/CsI(Na) phoswich scintillator devices.

The FOV of HXMT is $5.71^{\circ} \times 5.71^{\circ}$ (FWHM), and since the image reconstruction is based on the DD, it is composed by 18 non-symmetric FOVs
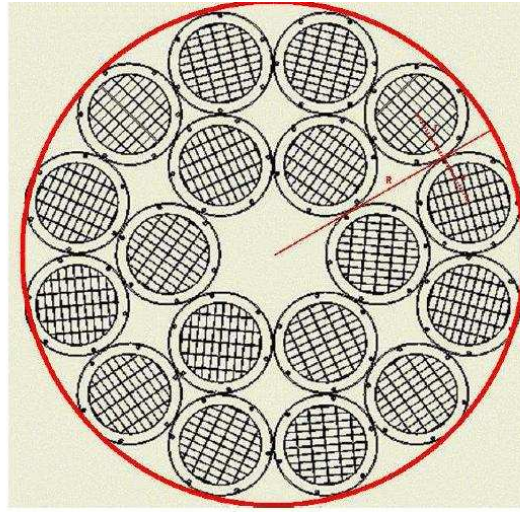
Figure 4.1 The FOVs of the 18 mechanical collimators aboard HXMT.

of $5.71^{o} \times 1.12^{o}$ related to each of the 18 collimators. The directions of the long axes of the 18 FOVs vary with a step size of 10°.

When a sky region is observed, the number of counts per second is detected as a function of time and usually has a triangular shape. The maximum of the triangle corresponds to the sky position of the source along the collimator direction and its level to the source flux. To compute the HXMT angular response, those of all 18 collimators must be combined together.

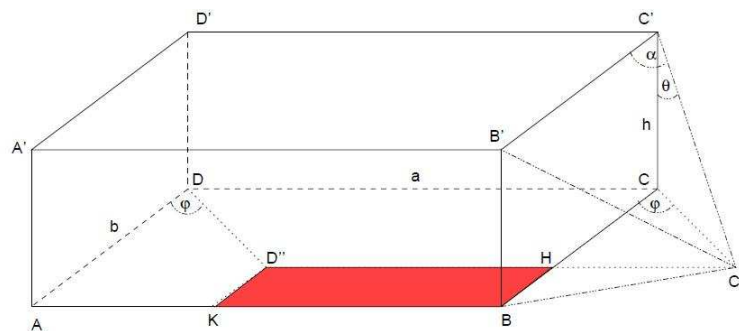Fig.4.2 shows a sketch of a collimator cell, with the shadows of its walls cast on its interior.

Figure 4.2 Schematic view of the collimator cell, together with the viewing angles θ, ϕ and α. In red the area left illuminated by the shadows cast by the collimator walls.

If the collimator walls are assumed to be perfectly opaque to the X ray radiation, the collimator angular response will be [62]

$$R(\theta, \phi) = \left[1 - \frac{h}{a} \tan \theta \sin \phi\right] \left[1 - \frac{h}{b} \tan \theta \cos \phi\right],$$ (4.1)

where a and b are the sizes and h the collimator cell height, θ and ϕ are the viewing angles for a given direction of the source flux.

By means of Eq.4.1, it is possible to build the HXMT total angular response function (a sort of PSF) by summing up all the 18 collimator angular responses. The result is shown in Fig.4.3, where in red are marked the FWZI and the FWHM (the latter being equal to 1.604^o). The angular response integrated in ϕ, that is a slice along a $\phi =$ constant direction, is shown in Fig.4.4. The shape is similar to a Lorentzian curve.
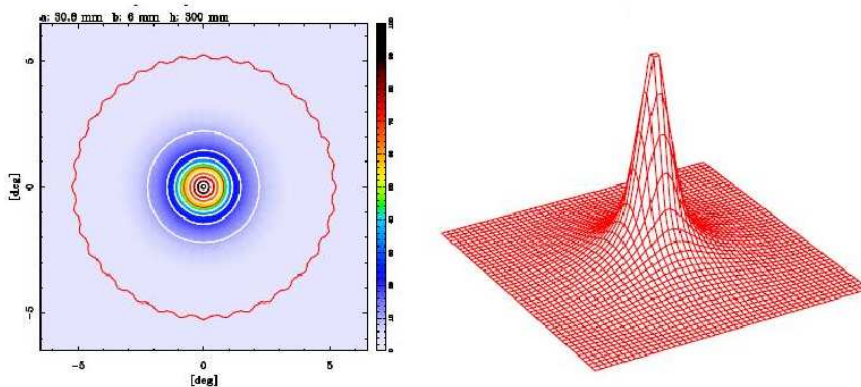
Figure 4.3 The HXMT angular response integrated for all the 18 HXMT collimators. Left: contour plot (in red the FWZI and FWHM; the latter being 1.604^o). Right: 3-dimensional plot.

Shen and Zhou [71] described an Accelerated DD (ADD) version and applied it to image restoration of data of the whole 18 High-Energy collimators simultaneously.

4.2 The INTEGRAL telescope

The INTEGRAL satellite [86] is a γ ray observatory mission that performs simultaneous observations in the γ rays (15 keV - 10 MeV), X rays (3-35 keV) and optical (V band, 550 nm) band, allowing to observe for the

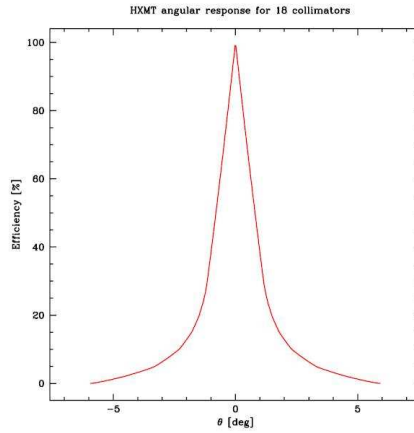Figure 4.4 The HXMT angular response integrated in ϕ. It has been obtained by slicing Fig.4.3 along a $\phi =$ constant direction. The measured FWHM is 1.604^{o}.

first time a single astronomical source simultaneously in all these energy bands.

The mission, managed by ESA with contributions from 16 European countries, as well as from Russia (with the PROTON launcher) and from NASA (with the Deep Space Network ground stations), was launched on October 17, 2002 from Baikonur in Kazakstan. INTEGRAL was designed for a nominal lifetime of 5 years, but in October 2009 it was decided to extend the mission at least up to the end of 2012.

The satellite was placed in a highly eccentric orbit, inclined at 51.6 ^{o} at launch, so allowing long uninterrupted observations with a practically constant background, far from the radiation belts around the Earth. The revolution period of the orbit is 3 sideral days (slightly less than 72 hours), so that the perigee occurs always at the same geographical point on Earth.

The scientific goals of INTEGRAL are achieved thanks to the high resolution spectroscopy (2.5 keV FWHM at 1 MeV) with fine imaging and accurate positioning of celestial γ ray sources. The fine imaging capability of INTEGRAL within a large FOV (total FOV of $29^{o} \times 29^{o}$ at zero sensitivity and of $19^{o} \times 19^{o}$ at half sensitivity [36]) allows the identification of the position and the direction of the incident signal. Once the correct position of an object is known, it is possible to study it at other wavelengths. The FOV of INTEGRAL is ideal for survey studies over large areas of the sky, that can be mosaiced together providing an almost complete all-sky coverage. At weekly intervals, a sawtooth path Galactic Plan scan inclined at 21° with respect

	SPI	IBIS
Energy Range	20 keV - 8 MeV	15 keV - 10 Mev
Detector	19 Ge detectors cooled to 85 K	16384 CdTe detectors (ISGRI) 4096 CsI detectors (PICsIT)
Detector Sensitive Area (cm^2)	500	2600(CdTe), 2890(CsI)
Spectral Resolution (FWHM)	2.3 keV @ 1.3 MeV	9 keV @ 100 keV
Field of Viev (Fully Coded)	16° (corner to corner)	$9^o \times 9^o$
Angular Resolution (FWHM)	2.5^o (point source)	$12'$
Source Location (radius)	$< 1.3^o$ (depending on the source strenght)	$< 1'$ (for 10σ source)
Absolute Timing Accuracy (3σ)	129 μs	92 μs

Table 4.1 Key performance parameters of the SPI and IBIS instruments. Taken from [17].

to the Galactic equator is made. Each scan consists of a series of exposures of 965 s each, separated by 6° along the scan path. Finally, Galactic Centre Radiant Deep Exposure, devoted to the observation of the Galactic Centre region (galactic longitudes between -30° and $+30^o$ and galactic latitudes between -10° and $+10^o$), is performed for an accumulated time of about 46 days/year.

INTEGRAL main scientific objectives are [86]:

- studies of compact objects (BHs, NSs, WDs);

- analysis and monitoring of high energy transient sources;

- studies of the stellar nucleosynthesis (novae and supernovae);

- studies of the Galactic Plane and Centre;

- studies of Galactic structures (clusters, maps of the continuum and of emission lines, interstellar medium, cosmic ray distribution);

- studies of extragalactic sources (AGN, nearby galaxies, cluster of galaxies, CXB);

- detection and identification of high energy sources;

- GRBs.

4.3 Scientific payload

The INTEGRAL payload consists of two main γ ray instruments: the imager IBIS (Imager on Board INTEGRAL Satellite [80]), which operates

from 15 keV to 10 MeV and the spectrometer SPI (Spectrometer on INTE-GRAL [84]), which operates from 0.2 to 10 MeV. IBIS and SPI are differently optimized in order to complement each other and to achieve overall excellent performances. Thanks to its good angular resolution, IBIS provides the best localization of the γ ray sources, while SPI can perform studies of spectral features. Both instruments have a sensitivity of a few mCrab, thus allowing broad-band spectroscopy.
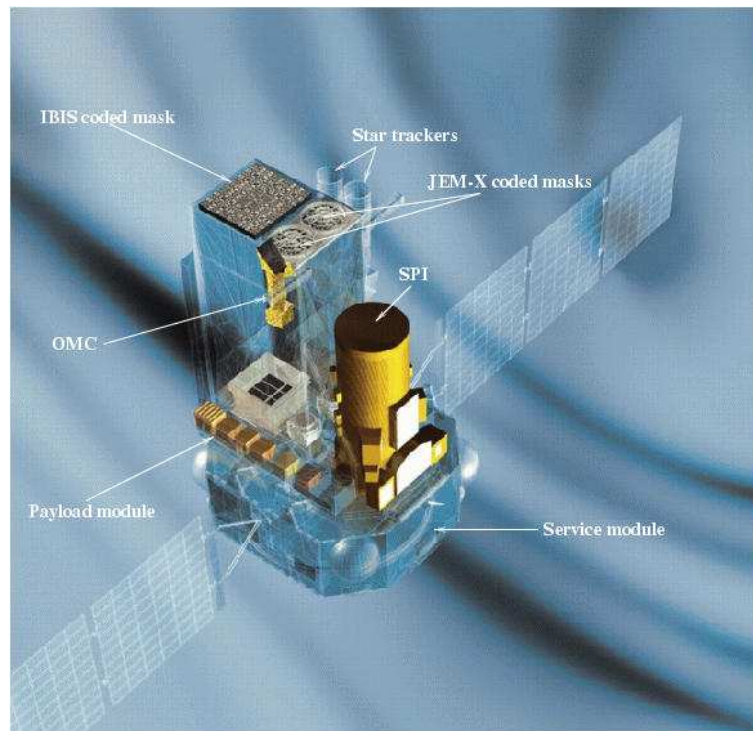
Figure 4.5 Picture of Integral Satellite. Taken from [86].

SPI and IBIS are complemented by two monitor instruments which cover the X ray and optical energy bands: the X-Ray Monitor JEM-X [58] and the Optical Monitoring Camera (OMC) [60].

SPI, IBIS and JEM-X share a common principle of operation: they are all coded-mask telescopes. A picture of the satellite is shown in Figs.4.5 and 4.6, where all the instruments are clearly visible. This chapter is devoted to describe IBIS. For further details about the other instruments see [18].

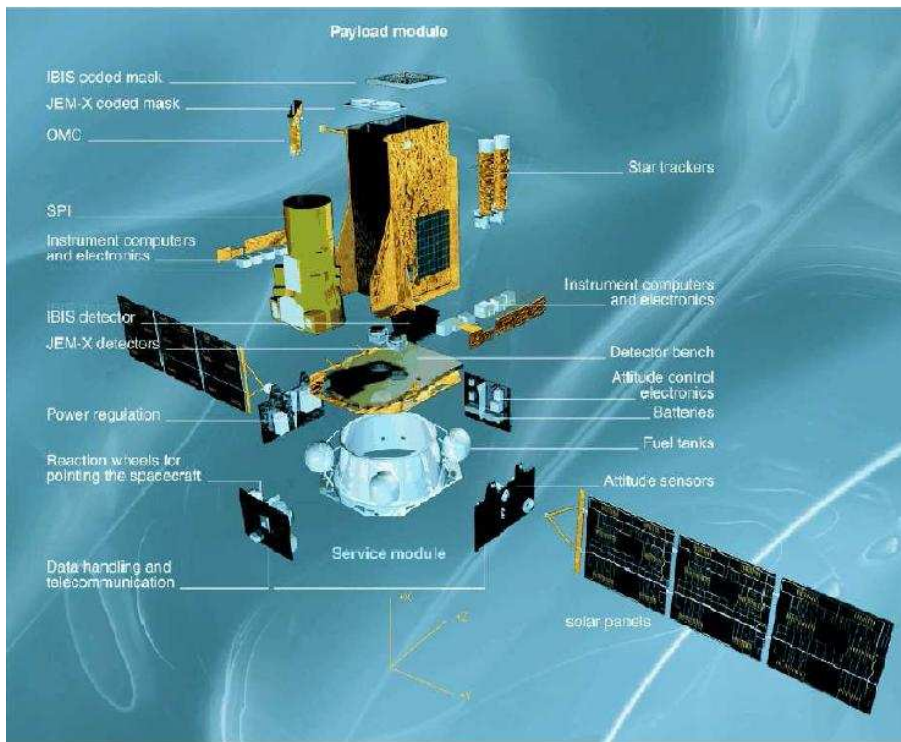Figure 4.6 A detailed view of INTEGRAL. Take from [46].

4.3.1 IBIS

IBIS is a γ ray telescope devoted to perform observations of celestial objects, in particular compact galactic and extragalactic objects. Table 4.2 gives an overview of its main features and capabilities.

It shows imaging capabilities (12' FWHM angular resolution) for source identification and spectral capabilities for the study of both continuum and broad lines in the 15 keV - 10 MeV energy range. The imager utilizes two PSD planes with a large number of spatially resolved pixels, implemented as physically distinct elements: ISGRI (INTEGRAL Soft Gamma Ray Imager [53]), that covers the 15 keV - 1 MeV energy band, and PICsIT (Pixellated Imaging CsI Telescope [52]), that covers the 200 keV - 20 MeV energy band. In Fig. 3.2, a picture of IBIS instrument optical design was shown. A $9^{o} \times 9^{o}$ FCFOV and a $29^{o} \times 29^{o}$ PCFOV are clearly distinguished. ISGRI pixel size corresponds to 5'×5', while PICsIT pixel size to 10'×10'.

Above the detector planes, IBIS has coded mask at a distance of about 3200 mm for ISGRI detector. The mask is optimized for imaging with both low and high energy photons.

The instrument is also equipped with anticoincidence system in order to

Energy resolution (FWHM)	9% @ 100 keV
	10% @ 1 MeV
Effective area	ISGRI: 960 cm^2 at 50 keV
	PICsIT: 870 cm^2 at 300 keV (single events)
	PICsIT: 275 cm^2 at 1 MeV (multiple events)
Field of view	9° × 9° (fully coded)
	19° × 19° (partially coded, 50%)
Point source location accuracy	30" @ 100 keV
(90% error radius)	< 5' @ 1MeV
Continuum sensitivity	3.8 × 10^{-7} @ 100 keV
photons cm^{-2} s^{-1} keV^{-1}	5.7 × 10^{-7} @ 1 MeV
(3σ, Δ E= E/2, 10^6 s integration)	
Narrow line sensitivity	1.3 × 10^{-5} @ 100 keV
photons cm^{-2} s^{-1}	3.8 × 10^{-4} @ 1 MeV
(3σ, 10^6 s integration)	
Absolute timing accuracy (3σ)	ISGRI: 61 μs (for E<1MeV and Compton)
	1 ms (Spectral timing, no imaging)
	2000s (E≥175 keV with imaging)
	PICsIT: 0.976-500 μs (selected from ground)

Table 4.2 Scientific parameters of the IBIS imager. Taken from [17] and [80].

reject unwanted events due to cosmic rays and background photons produced inside the satellite itself. A collimation system limits the IBIS low energy angular response (≤ a few hundreds of keV).

4.3.2   Further details on ISGRI

As said, IBIS is made of two position sensitive independent detectors: ISGRI on the top and PICsIT at the bottom with respect to the coded mask. Since ISGRI is the detector providing the highest resolution images and the most detailed studies of complex fields, we deconvolved IBIS data assuming that only ISGRI detector was on. Here further useful details only about ISGRI are added.

A detector is characterized by three main parameters: spectral range, energy resolution and number of pixels in the detector associated with the imaging capability. Spatial resolution and detection efficiency are the criteria for the quality of image detectors.

ISGRI is made of a solid state CdTe (Cadmium Telluride) detector array. CdTe is a semiconductor with high atomic number ($Z = 48$-52), operating at room temperature ($0^o \pm 20\ ^oC$). When photons hit the detector electron-hole pairs are generated. The electrons are then collected by anodes under the action of an external electric field. The amount of generated electric charge is essentially proportional to the energy of the incident photons, after that a correction for the collection time of the electrons is performed.

ISGRI comprises 8 identical Modular Detection Units (MDU), each having 32×64 pixels for a total of 16384 pixels (left panel of Fig. 4.7). The pixel size is 4.6×4.6×2 mm, so the total sensitive area of the detector is 2621 cm^2. They are smaller than the mask elements. With their small area, the CdTe
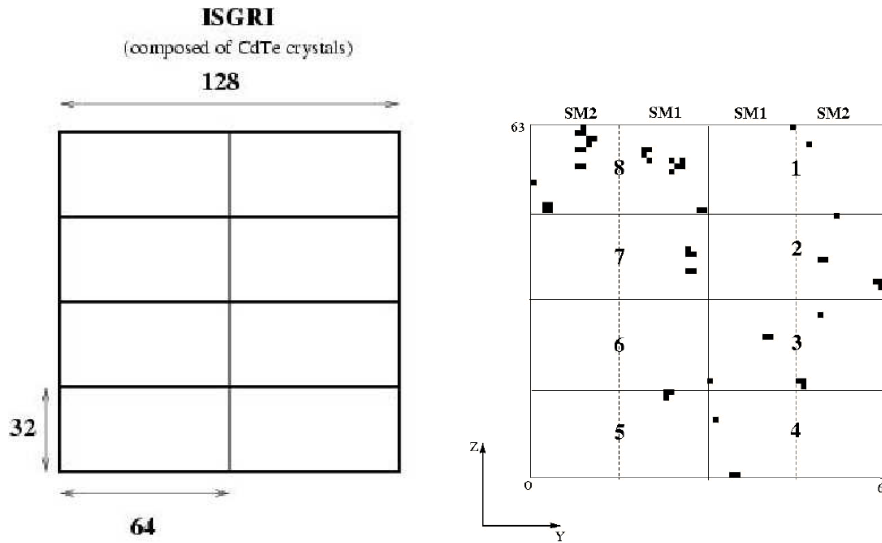
Figure 4.7 ISGRI detector representation (left) and location of the killed pixels (right).

detectors are ideally suited to build an image with good spatial resolution of 4.6 mm (separation between pixel centers).

ISGRI MDUs are mounted on a support grid. The pixels of this grid are not sensitive to the hard-X/γ ray radiation. So, each data file is composed by a 128×128 pxl array of counts, but, before deconvolving, it must be extended to 130×134 pxl geometrical grid.

It is possible that some of the ISGRI pixels become noisy. If the particular pixel countrate is much higher than that of their module pixels, the onboard electronics switch it off. The onboard software that detects and switches OFF noisy pixels periodically recovers them. The overall killed pixels are less than 1% (right panel of Fig. 4.7).

4.3.3   The Mask

The IBIS Mask Assembly is composed by three main subsystems: the coded pattern, the support panel and the peripheral frame. The support panel transparency should be taken into account in the data analysis, as it absorbs part of the flux. On the other hand, the peripheral frame supports whole system.

Ideally, a coded mask should have a null thickness and be totally opaque and transparent to radiation elements. In IBIS the closest configuration to the ideal situation has been achieved in the following way. In order to have the

maximum opacity, tungsten has been used. This metal has a high atomic number (Z=92), is very dense (ρ=19.3 g cm^{-3}) and is very opaque to high energy photons. As far as the mask is concerned, its thickness has been set to 16 mm in order to maximise the weight while avoiding auto-collimation effects that attenuate the incoming radiation.

In the previous chapter it was stated that, from a mathematical point of view, the mask can be considered as a matrix of 1 and 0, representing transparent and opaque elements, respectively. In reality, however, the mask elements are neither totally transparent nor completely opaque to γ ray photons. Each coded mask system has, in fact, a characteristic opacity (or transparency) curve, which describes the capability of the instrument to modulate the radiation as a function of energy, position and interaction of the photon with the mask.

The IBIS basic coded pattern (left panel of Fig. 4.8) is a square array of size 1064×1064 mm^2, made up of 95×95 individual square cells of size 11.2×11.2 mm^2. The mask coded pattern chosen is a mosaic of a 2×2 cyclic replication of MURA of order 53, minus 11 lines and 11 columns in order to avoid ambiguity in the signal decoding procedure. The properties of the MURA patterns are described by e.g. [38] and [76].
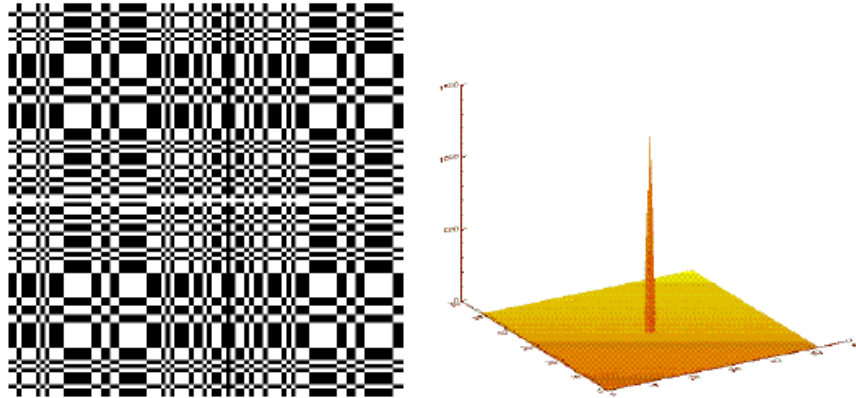

Figure 4.8 The IBIS mask pattern of 95×95 elements (left) is formed by a replicated 53×53 MURA basic pattern, whose cyclic autocorrelation (right) is a δ function. Remember that autocorrelation is the PSF in the FCFOV. Taken from [36].

The mask is about 1.8 times larger than the detector. This configuration

allows for the use of smaller detectors, thus limiting the γ ray background. Approximately half of the mask cells are opaque to photons in the operational energy range of the IBIS instrument, offering a 70% opacity at 1.5 MeV. The other half of cells are open, with an off-axis transparency of 60% at 20 keV.

4.3.4 The Instrumental Background in IBIS

Since the intensity for most sources is very faint, γ ray observations are highly affected by background radiation. The main background components in IBIS are the cosmic diffuse γ ray background, relevant at low energies ($E < 100$ keV) and the internal background due to cosmic rays interacting with the satellite materials. While the first component impacts the ISGRI observations, the second mainly affects the PICsIT results.
Other effects can influence the detector background, such as the solar activity and the anticoincidence system performance.
The reduction of the background counts by the anticoincidence system has been evaluated about 50%, with respect to the case when anticoincidence system is switched off.
IBIS is positioned close to SPI and JEM-X. Since γ ray photons are highly penetrating, it is possible for them to pass through the satellite, instruments and coded masks, thus being detected by all the instruments. Off-axis γ rays (generally above 300 keV) passing through the SPI coded mask can produce a shadowgram of the SPI mask on the IBIS detectors. Although in this case the IBIS FOV is enhanced, a bright γ ray source adds additional counts and modulation to the IBIS measurements, complicating the image reconstruction.
In order to suppress systematic effects due to spatial and temporal background variations and to take into account the not always perfectly coded signal, an opportune dithering observation strategy is employed [21]. It consists in a series of pointings 2° off-axis with respect to the target of the observation. Dithering increases the number of measurements helping to reduce the systematic errors in the deconvolution process. There are two different types of dithering, schematized in Fig. 4.9.

- The rectangular dithering employs a square pattern centered on the target position (one on-axis pointing and 24 off-axis pointings, each separated by 2° in a $5^o \times 5^o$ rectangular pattern). This mode is used when there are several point sources in the FOV, sources with unknown

positions and diffuse extended emission.

• The hexagonal dithering employs a hexagonal pattern centered on the target position (one on-axis pointing and 6 off-axis pointings, each separated by 2° on the six verteces of an hexagon). This mode is used only for observations of point or isolated sources, with known positions, where no contribution from off-axis sources is expected.
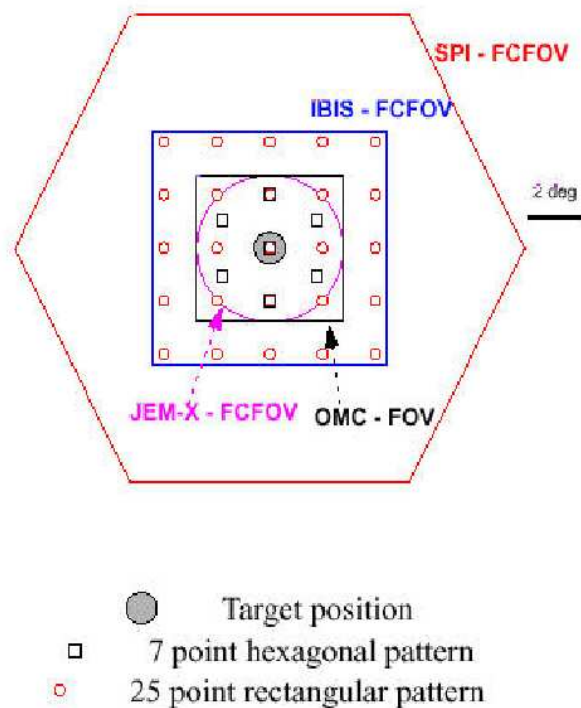
Figure 4.9 Dithering strategy for IBIS/INTEGRAL. The central circle is the position of the observation target, squares indicates the hexagonal pattern and circles the rectangular one.

4.4 Detector properties

When a mask-detector configuration is chosen, the detector should satisfy some requirements on its spatial response to make a proper recording of the shadowgram. The accuracy in the location of a source in the FOV is determined by the detector ability to distinguish as well as possible all parts of the shadowgram. Fixed the mask/PSD separation, the finite spatial resolution of the PSD is the basic limiting factor for both point source location

accuracy (PSLA) and angular resolution of the instrument. In a coded mask system, the detector spatial resolution is defined by the detectors pixel size. PSLA parameter expresses the capability of the detector to localize sources. It depends on both the angular resolution of the coded mask system and the finite spatial resolution of the detector. Caroli [15] showed how the theoretical PSLA depends on the detector performances as:

$$PSLA = \frac{\arctan(H/L)}{SNR},$$ (4.2)

where L is the mask-detector distance.

Gros [39] showed how the the absolute localization in ISGRI is less than 1' for sources detected at a significance level higher than 20σ and 3' for sources at a significance level of about 7σ. Using data od the 4th soft-γ ray survey catalog [6], S. Scaringi et al. [68] found that the PSLA has improved significantly since the study of Gros et al. [39] and this can be attributed to improvements in the OSA software.

The angular resolution firstly depends on the angle subtended by a mask element at the PSD and, hence, on the mask element size. However, the maximum resolution achievable is dictated by the positional resolution of the PSD. Indeed, for a given positional resolution, the smaller the mask elements are, the higher will be the effect of the random errors in the positioning of the detected photons [61].

At hard-X/γ ray energy where diffraction is negligible, assuming the same size for detector pixels and mask elements, the theoretical angular resolution (i.e. the minimum angle at which two nearby sources are distinguishable) depends both on the linear dimension of the mask elements H and on their distance from the detector L. For a on-axis object one will have

$$d\alpha = \arctan \frac{H}{L},$$ (4.3)

for the PSF. Each pixel in the deconvolved image has angular size (FWHM) of approximately H/L.

If the source is off-axis of a certain angle ϕ, the angular resolution is:

$$d\alpha = \arctan \left(\frac{H}{L} \cos^2 \phi \right).$$ (4.4)

The angular resolution is consequently determined by the H/L ratio; since in IBIS H=11.2 mm and L=3200 mm, it turns out to be 12' for on-axis sources and higher for off-axis ones.

However, in the IBIS case, mask elements are bigger than detector pixels. The ratio R between their dimensions is $R = H/s_d = 2.43$ for ISGRI. To better sample the shadowgram, the decoding array G must be resampled at the ISGRI's pixel size. Data counts must be redistributed according to the fraction of pixel area covered by a given projected mask element. The resulting coded image has pixels of the ISGRI pixel angular size, i.e. ≈ 4.94'. The theoretical PSF peak in the FCFOV is space-invariant and given by the convolution of two square-pyramidal functions with FWHM equal to mask element size and linear pixel size, respectively. Using the central limit theorem, the convolution of these functions can be approximated by a bi-dimensional Gaussian with a width of $s_{PSF} \approx \sqrt{H^2 + s_d^2}$. So, the corresponding angular resolution [39] is:

$$d\alpha = \arctan\left(\frac{\sqrt{H^2 + s_d^2}}{L}\right) = 13.26',$$

(4.5)

which is a bit worse than $\arctan(H/L) = 12'$.

4.5 The System Point Spread Function (SPSF)

In this thesis, the definition of the PSF contains only the geometrical component of the image system response to a point source in the middle of the FOV. The PSF is the decoding array employed for both CC and LR.

The SPSF is the spatial response of the imaging system to a point source also considering the decoding process. In this section the SPSF resulting from the balanced cross-correlation seen in Sect.3.4.1 used in the IBIS data analysis will be discussed.

The SPSF of an optimum coded mask system is independent on position in FCFOV and given by the convolution of a block function (describing the peak of the delta function) with one describing the kind of decoding applied and then with a function which describes the detector spatial resolution.

The result of the object reconstruction depends on both the mask pattern M and decoding array G. The quality of any choice can be evaluated by studying the $SPSF = G * M = \overline{P}P$ [30], where $\overline{P}$ and P were described in Sect.3.3. The correlation method does not suffer for the problem of amplification of the noise term, because the matrix has finite elements.

On the other hand, using the correlation method, the SPSF is no longer in general a delta function. The SPSF of the balanced correlation in total

FOV for the IBIS MURA and for an on-axis source is a δ function over a flat level in the FCFOV plus at most eight ghosts and secondary lobes in the PCFOV (see Fig. 4.11). This degradation depends on the structure of the SPSF and not on the statistical quality of the data. It cannot be reduced by increasing the exposure time.

The variance (Fig. 4.10) associated to the reconstructed sky image is constant over the FCFOV, but decreasing (increasing in relative value) in the PCFOV.

Since in our analysis a different decoding process was employed, the LR deconvolution will show a different SPSF.
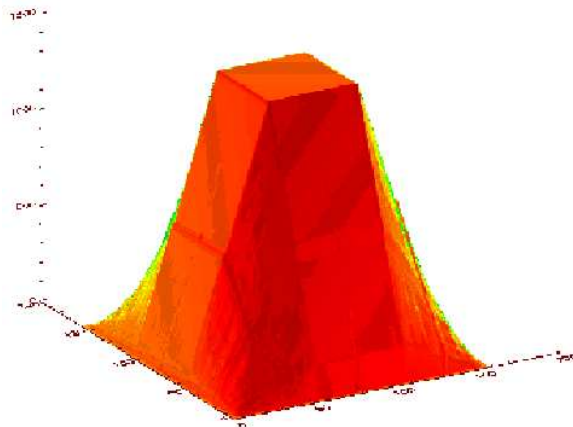

Figure 4.10 Variance associated to the reconstructed sky image is constant over the FCFOV while decreases (increases in relative value) in the PCFOV. Taken from [36]

4.6   Signal-to-Noise Ratio

The evaluation of image goodness is an age-old problem: for a given mask design, the quality of the restored image is closely related to the decoding technique employed. The ability of each deconvolution method to reconstruct faithfully the source flux that is a good estimate of the real one must be checked.

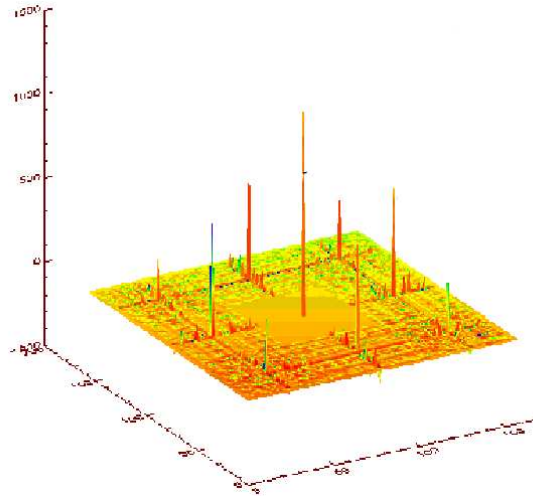One parameter which may be employed to define the quality of the recon-

Figure 4.11 The SPSF of the balanced cross-correlation over the total FOV for the IBIS/ISGRI telescope for a 53×53 MURA Optimum System and an on-axis source. A delta function in FCFOV and coding noise plus 8 ghosts can be recognize in the picture. Taken from [36]

struction is the Signal-to-Noise Ratio (SNR) which determines the minimum detectable source intensity.

Caroli et al. [14] have shown how the balanced cross-correlation deconvolution performed by $G = 2M - 1$ ensures a direct subtraction of the constant background from each pixel of the image, so directly giving the estimate of the source photons coming from each element of FOV. Unfortunately, since the variance associated to each pixel has a constant value only in the FCFOV, the direct background subtraction is guaranteed only in the FC-FOV. Futhermore, the background contribution to the errors is uniformly distributed over the FCFOV.

Since the IBIS INTEGRAL MURA has a large number N of basic pattern elements, the average root mean square error, σ, for all pixels in the restored image [14] is approximately the square root of the total counts detected during the observation period, $\sqrt{S + B}$, i.e.

$$\sigma \approx \sqrt{\frac{N + 1}{N - 1}} \sqrt{\frac{S}{S + B}}. \tag{4.6}$$

The IBIS/INTEGRAL mask basic pattern is a MURA of odd order 53, so the fraction of transparent elements is $(N + 1)/2$. Due to the excess of one transparent element, the flux estimated from a generic direction k in the

FCFOV using this correlation operator, is $S_k + B_k$. i.e. the background is not automatically subtracted.

Furthermore, the condition of uniform background over detector plane is usually not totally verified. The decoding process magnifies these background fluctuations, so it is needed to correct the non-uniform background spatial distribution.

Another source of systematic noise is the non perfect coding (sidelobes) due to non ideal system (dead zones, geometrical effects, etc). Coding noise is proportional to the source flux.
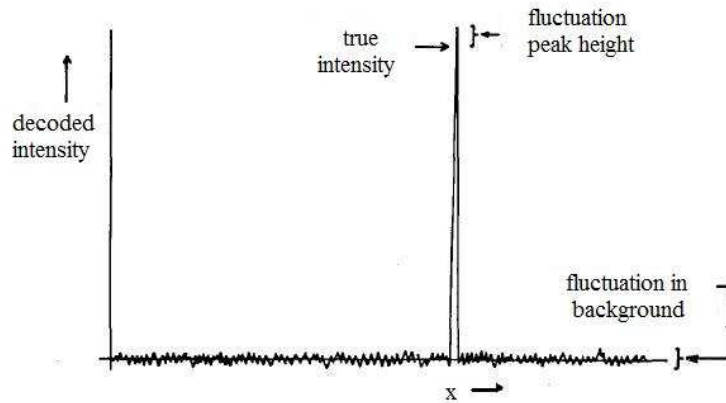

Figure 4.12 A monodimensional slice through a reconstructed point source. The SNR is defined to be the peak height divided by the expected size of the fluctuations of the peak and the background. Taken from [26].

In the perfect case, the standard error in the count rate in any one pixel is determined uniquely by the total number of detected counts [26], and, for a background dominated situation as the γ ray sky, is virtually independent of source counts. The expected theoretical source significance tss will be given by

$$tss = \frac{S}{\sqrt{S + B}}.$$ (4.7)

Since the expected sensitivity must take into account the non-uniform background against which any source must be detected, the expected tss will be only a theoretical upper limit for the sensitivity of a point source S over the background B. For a complete derivation of this equation see Appendix A. The sensitivity depends also on the detector spatial resolution. An imaging efficiency factor must be applied to this maximum SNR, as can be seen in

[15] and [75].

In the practical case, source signal cannot be measured independently from the background. Only $S' = S + B$ is available for a deconvolved source. So only in simulation an estimate of S can be derived by the difference between total data and background distribution, i.e. $S' - B$. Since all data counts are employed to reconstruct the FCFOV and, on the other hand, all data errors must be added in quadrature because of the propagation of errors rule, the maximum measured SNR will be given by:

$$SNR_{max} = \frac{S' - B}{\sqrt{S'}}. \qquad (4.8)$$

Detected SNR is computed by dividing the peak height by the standard deviation, assuming all the background variation due to statistical effects only [77]. Necessarily, this value will be less than the expected SNR in Eq.4.7.

The SNR definition employed in our analysis is slightly less rigorous, i.e. in terms of the theoretical source significance (in σ number) at which source flux would be reconstructed in a perfect imaging system. So, the actual measured SNR was defined as:

$$SNR_{det} = \frac{max - \mu}{\sigma}, \qquad (4.9)$$

where max is the value of peak flux, μ and σ are mean and standard deviation of the background values in the deconvolved images (Fig. 4.12). Significances are distributed as a Gaussian: a measure of its width provides an estimate of residual systematic noise.

4.7   INTEGRAL data and OSA scientific analysis

The INTEGRAL Science Data Centre (ISDC) released the Off-line Scientific Analysis (OSA) software [79] based on an evolution of the cross-correlation technique described in Sect.3.4.1 and in [37], [36] and [39]. This section briefly decribes the structure of the INTEGRAL data and the main steps of the analysis made by OSA.

Our iterative code based on the Lucy-Richardson algorithm is only a first approach to image deconvolution analysis. Indeed, it only takes into consideration the geometrical features of coded mask image formation. OSA software represents the state-of-art image quality, because it considers a larger class of phenomena that could affect IBIS data deconvolution. For

this reason, OSA outputs will be used as a validation mean for our results.

4.7.1 Science Window and Observation Groups

Because of the dithering, an observation is made of many pointings (i.e. periods during which the spacecraft axis pointing direction remains stable) of about 30 minutes separated by slews (i.e. periods during which the spacecraft is moved from one pointing to another). Each pointing and slew, or a part of them if they are too long, is called a Science Window (SCW).
Usually, the observation consists of several SCWs. All data produced during a pointing or a slew are stored into a set of FITS files. They are grouped together into a Science Window Group (SWG) containing all the data belonging to this SCW.
The data structure contains also:

- observational catalogs of high energy and optical sources useful for the data analysis. Currently, version 30 of the catalog contains about 1703 objects brighter than approximately 1 mCrab in the 1 keV - 10MeV band and all new IGR sources up to March 12, 2009 [79].

- data relating to the calibration and operation of the instruments.

4.8 The Scientific Analysis

The OSA scientific analysis transforms the prepared data into the final high-level products: sky images, source positions, fluxes, spectra and lightcurves [36]. Its pipelines are made of one independent component for each of the INTEGRAL instruments. Here the main steps in the case of the IBIS/ISGRI will be briefly described.
The first step consists in the identification and the collection of the relevant pointings. Once the list of SCWs is available, an Observation Group (OG) can be created.
For each SCW, intensity (in units of cts s^{-1} renormalized to FCFOV), significance, variance and residuals maps are obtained and then iteratively searched for sources and cleaned from the source side lobes. In this iterative process the source peaks are fitted with a bi-dimensional Gaussian and finely located. The images are rotated, projected and summed after being weighted for the variance.
The OSA scientific script for IBIS analysis consists of three smaller ones: the first two work on a SCW basis, while the third on the whole OG.

For our analysis pourpose, only the ISGRI data were employed and only the sky maps were reconstructed. The first sub-script is devoted to the correction of SCWs. It is composed by the following tasks.

- COR (Data Correction) locates noisy pixels, corrects the photons for rise time and temporal variation of the gain and, finally, transforms channels to energy.

- GTI (Good Time Handling) excludes times of stream gaps, high background, instrument anomalous behavior, etc ..., so creating a good time interval (GTI) which must be used to select good events.

- DEAD (Dead and Live Times) computes dead time (i.e. the time during which the instrument is not able to collect photons), within the GTI.

- BIN_I (Event Binning for Imaging) defines the energy bins to be used for imaging, selects good events within the GTI and creates event arrays. For each energy range, the intensity shadowgram and a corresponding efficiency map are created.

- BKG_I (Background Model Generation for Imaging) derives estimated background from models. Background models are built from a large sample of empty fields or from high latitude pointing observations. Then, IBIS shadowgrams are corrected for efficiency and the background is subtracted.

After these steps the high-level analysis is performed. The second script takes the whole OG just created as input and performs the following tasks:

- CAT (Catalog Source Selection) selects a list of known sources from the reference catalog and creates a source data structure, containing source locations and expected flux values.

- IMA (Image Reconstruction Analysis) generates sky images and looks for sources. The detected source list with reconstructed right ascension, declination, flux, error and significance was created.
  In the ISGRI case, shadowgrams are deconvolved, source search is performed in the single images as well as in the mosaic (i.e. combination of different images) and a list of detected sources is created. In this step, PICsIT detector is not taken into account.

The third script again works SCW by SCW. It prepares data for spectra creation, extracts spectra, products light curves for individual sources. This goes beyond the scope of this thesis.

Chapter 5

Direct Demodulation and
Richardson-Lucy algorithm

Chapters 3 dealt with the usual method to deconvolve coded mask data in high energy astrophysics: the cross-correlation. Eq.3.16 is almost optimal for the image reconstruction of coded mask system with decoding array G such that $M * G = \delta$. Another possibility is represented by nonlinear iterative techniques, an useful tool when data are noisy (low SNR).
This chapter will describe the theoretical basis of the DD method. Furthermore, it will deal with the LR algorithm, chosen to solve the imaging problem in Eq.3.12.

5.1   Introduction

The DD [55] and [56] for reliable inversion has been developed since 90's by Chinese scientists. High resolution reconstructions of complicated objects are achieved by directly solving modulation equations in iterative way under physical constraints. These algorithms operate on the result of the previous iteration and are normally slow to converge toward the final result. The iteration method used to solve the linear system could be the Gauss-Seidel method or its variant SOR (Successive Over-Relaxation), the Jacobi method or the Lucy-Richardson (LR) one [64] and [57]. The iterative algorithm most often used in image deconvolution with Poisson data is the LR. It attempts to maximize the likelihood of the restored image by using the Expectation-Maximization (EM) algorithm [82]. It requires only to know the PSF as good as possible and treating object, PSF and image as probability functions. Its recursive formula in the image space, corresponding to

$d_i = \sum_{j=1}^{q} p_{ij} f_j + b_i$, is

$$f_j^{(r+1)} = f_j^{(r)} \sum_{i=1}^{p} \left(p_{ik} \frac{d_i}{\sum_{j=1}^{q} p_{ij} f_j^{(r)} + b} \right) \qquad (5.1)$$

or, in matrix form,

$$f_j^{(r+1)} = f_j^{(r)} \left(P^T \frac{d}{P f^{(r)} + b} \right) \qquad (5.2)$$

where $i = 1, \ldots, p$ is the observation point of the detector, $j = 1, \ldots, q$ is the position of the element in the image space and r is the iteration index. The complete mathematical derivation of Eq.5.2 in absence of background radiation is given in Appendix C.2.1, so showing there is no mistery behind this method. Indeed, in astrophysics, it has been most widely used for instance for restoring Hubble Space Telescope optical data [85] and [42]. Some studies also exist in high energy range, as the work of Allain [1] and [2] on INTEGRAL/SPI, where a Bayesian approach is employed.

The DD extracts the information from the data more efficiently than conventional inversion methods. The results obtained by Chinese scientists show a significant improvement of the spatial resolution (also better than the intrinsic one) and sensitivity, decreasing the impact of background and noise. It can greatly improve the source location precision and the angular resolution. The DD has been tested on many mission data and different kinds of instruments. In this thesis we decided to apply it to the IBIS/INTEGRAL data.

In this chapter a Maximum Likelihood (ML) approach for image reconstruction is adopted. It leads to the minimization of functionals derived from the properties of the noise and from the additional information on the solution.

5.2   Classical inversion techniques

As described in Sect.3.3, the image process must deal also with the presence of the noise. It is the realization of a random process, the properties of which (mean value, variance, its probability distribution, etc) are known. These properties must be used in the formulation of the problem. In a probabilistic approach it is assumed that both the object f and the detected image d are realizations of random variables, denoted respectively by ϕ and δ. A modelling of the system requires to model the noise with its probability density, $p_\delta(d|f)$, which depends only on the object. This will be clearer in

the following sections.

The image reconstruction process described in Eq.3.12 turns out to be ill-posed in the Hadamard sense. Its solution may not exist or, when it exists, is completely deprived of its physical meaning as a consequence of error propagation and amplification. Moreover, even if an unique solution can be found, this is strongly perturbed by noise propagation with oscillations including non-physical negative values. This is also the case of the IBIS PSF. In Chapter 3 the cross-correlation technique applied to coded mask systems was discussed in details.

The discrete correlation transform of $d = Pf + b$ is:

$$c = P_c f, \qquad (5.3)$$

where $P_c = P^T P$ and $c = P^T d$. The matrix P_c is always symmetric and positive definite. This guarantees the convergence of the iterative algorithm to the exact solution. Nevertheless, the cross-correlation coefficients c are only an image of the object reconstruction, because they ignore the information included in Eqs.5.3 and 3.12.

Before describing iterative methods, a hint to the employment of Fourier transform (FT) is right and proper. The FT reduces a convolution in the image space to a simple multiplication in the Fourier space. The implementation of this technique by means of Discrete Fourier transforms (DFT) can produce noise amplification due to small values in the DFT of P, also in high SNR situations (≤ 100). The presence of small or null terms in the DFT of P appears to be a quite general property of the binary matrices as those representing coded masks.

5.3 Constrained optimization and DD

Generally, when dealing with a linear inverse problem $Pf = d$, it happens that the inverse of the linear operator P either does not exists (i.e., the problem is ill-posed), or is nearly singular, giving highly noise-sensitive solutions (i.e., the problem is ill-conditioned). In order to deal with this nature of the problem, a large number of linear and nonlinear methods has been developed. Most linear methods are based on regularization, while nonlinear ones, as the LR code, are developed under Bayesian framework and are solved iteratively.

Constrained optimization deals with minimization or maximization of some real-valued objective function F with equality and/or inequality constraints

on the solutions, e.g.:

$$\min F(x) \tag{5.4}$$
$$s.t. \quad Qx + b = d,$$
$$x \geq 0$$

Both the source flux and the noise are unknowns. In Eq.5.4, $x = (f, n)^T$ and $Q = [P|I_m]$, where I_m is the identity matrix of the same dimension of the noise. To solve the system in Eq.5.4, a minimum nonlinear problem with linear constraints in x (i.e. in n and f) must be written. The DD solves this minimum problem imposing linear constraints on the intensity, i.e.

$$low_j \leq f_j \leq up_j, \tag{5.5}$$

where low_j and up_j are the lower and the upper bounds for the source flux. The definition of the objective function F must be established in accordance with the noise statistics and the upper and the lower bounds must be included into it. Y.Chen, T.P.Li and M.Wu [16], proposed the following form for F:

$$F(f, n) =$$
$$\left[\left(\sum_{i=1}^{N} \frac{n_i^2}{d_i} - N \right)^2 + \rho \left(\sum_{i=1}^{N} n_i \right)^2 \right] - \beta \sum_{i=1}^{M} \left(\ln(f_i - low_i) + \ln(up_i - f_i) \right) \tag{5.6}$$

where N is the number of bins of the observational data and M is the number of sky bins. The constraint condition is:

$$\sum_{i=1}^{M} p_{ji} f_i + n_j = d_j \quad j = 1, \ldots, N \tag{5.7}$$

where p_{ij} is the (i, j) element of the PSF P and n_j is the jth element of the noise array. The term between square brackets is connected with the Poisson noise statistics, i.e. with its mean and its variance. The term $\rho \left(\sum_{i=1}^{N} n_i \right)^2$ is the expectation value of the noise, assumed to be zero, where ρ is a regularization parameter. The term $\left(\sum_{i=1}^{N} \frac{n_i^2}{d_i} - N \right)^2$ is the variance of the data and it should be equal to the number of data N. For a complete description of these terms, see Appendix B.

Finally, the logaritmic term is a barrier function. Its values increase to infinity as approaching the boundary of the feasible region (i.e. the space of

all candidate solutions), so becoming more and more negligible except close to the boundary. It is used as a penalty term for the violation of constraints. β is the barrier parameter.

The LR algorithm could be used to solve minimization problem in Eq.5.4. It was applied to the modulation equation, being known both data and PSF. The PSF used in our analysis is of geometrical type. It is the shadowgram obtained by the geometrical projection of the coded mask aperture assuming a point source in the middle of the FOV.

In a second step, we would like to implement Eq.5.6, but the big sizes of the arrays involved in the computation prevent us to do it for the moment. This is an important key-point to check in the near future.

5.3.1 Background lower bound

The LR does not explicitly compute the inverse of the coefficient matrix P, so this algorithm can be used to solve the image formation equation with rectangular coefficient matrix. The use of the background as lower bound for the source intensity is a key component of the DD. It is needed to estimate it from the observed data.

If the object consists of strong discrete sources and the background is weak the lower bound can simply be equal to the average background. If the background is structured or there are extended sources in the FOV, a continuum background map must be produced, including structured background and diffused sources. This map must be employed for the background subtraction before the deconvolution.

First a recursive procedure similar to the CLEAN routine [43] can be used. It subtracts the contribution of point sources with intensities greater than the minimum intensity of point sources to be reconstructed and derives the background. Iteratively solving the correlation equations for the background the continuum background is finally obtained.

Because of its nonlinear nature, the direct error estimation for the DD is difficult to perform. The error depends on the PSF shape, the iteration number, the total counts of the observation, the distribution of the source, the background level and so on. It is better applying the bootstrap method [24] and [22] for uncertainties estimation.

5.4   Statistical image deconvolution

Due to the random nature of noise, the recorded image is the realization
of a random process, so a statistical approach to the reformulation of the
image deconvolution problem is desirable.

An ill-posed problem creates a set of approximate solutions that contains
not only physically acceptable objects, but also randomly oscillating objects.
To limit the possibility of finding bad solutions, some kind of regularization
is necessary. For the deconvolution, constraints on the feasible region of
the solution and statistical information (the so-called "prior") about the
unknown object are used.

Nonlinear methods use Bayes theorem to regularize the ill-posed imaging
problem and solve it iteratively. Following a statistical approach, the object
statistical properties are a set of parameters that give some kind of a priori
information about the object itself. The following application of the ML
method for the parameters estimation reduces the image deconvolution to
the minimization of a suitable objective function.

Some simple considerations on convexity lead to the existence and unique-
ness of the ML problem solution in the Poisson noise case with zero back-
ground. However, the obtained estimate usually is not stable with respect
to noise fluctuations. The total flux conservation constraint (i.e. the total
number of counts of the rth reconstruction is equal to the total number of
the image counts) is automatically satisfied only in the case of zero back-
ground. However, this constraint partially reduces but not suppresses noise
fluctuations in presence of background radiation. If there is background, the
total flux conservation must be introduced as an additional constraint in the
minimization problem. If P is normalized in such a way that the sum of all
entries of each column is equal to 1, the total flux constraint is written as:

$$\sum_{j=1}^{N} f_j = \sum_{i=1}^{M} (d_i - b_i) \equiv c, \qquad (5.8)$$

where c is the flux constant.

ML methods, in general, lead to a reformulation of the problem which is
still ill-posed because only information about the noise and non-negativity
constraint are used. Some further regularization is necessary.

The instabilities in the solution appear when the iteration number increases
too much. The first possible regularization approach is the employment
of a suitable early stopping of the iterations. The iteration number must

be chosen in such a way to guarantee the right trade-off between image resolution and stability of the solutions.

However, due to the statistical setting of the ML, the most general approach to the regularization is provided by a complete employment of the Bayesian statistics.

5.4.1 Expectation-Maximization solution

In statistics, given a set of data d, an EM algorithm is a method for finding ML or MAP (Maximum A Posteriori) estimates of the unknown parameters. The EM is an iterative method that alternates between performing

- Expectation step: computation of the expectation of the log-likelihood evaluated using the current estimate for the hidden variables.

- Maximization step: computation of parameters maximizing the expected log-likelihood found on the E step.

The estimates of these parameters are then used to determine the distribution of the hidden variables in the next E step.

The EM was first applied to image reconstruction by Shepp and Vardi [73] in the field of medical imaging. Their algorithm was identical to those independently obtained by Richardson [64] and Lucy [57]. While the LR method makes no assumption about the noise, the EM stipulates Poisson noise in data and seeks the optimal solution under noise degradation. For the Richardson's derivation look at Appendix C.

Shepp and Vardi [73] proved that the algorithm iteration converges to the ML solution for Poisson statistics in the data, while it keeps the reconstructed image non-negative. The convergence of this algorithm to the ML estimate is guaranted if all components of the initial guess are positive. A proof could be found for instance in [82].

The next section, following the Shepp's and Vardi's approach, derives the LR recursive formula:

$$f^{(r+1)} = f^{(r)} \left(P^T \frac{d}{Pf^{(r)} + b} \right) \quad r = 0, 1, \ldots. \tag{5.9}$$

5.4.2 The ML in the case of Poisson noise

In the following, greek letters will be used to indicate random variables. Let d_i the number of photons detected at the detector pixel i. If its mean intensity $(Pf+b)_i$ is time-independent, the fluctuations in the photon counting process obey to Poisson statistics. The noise n and the data d are considered as a realization of r.v. ν and δ. The image formation equation (Eq.3.12) relates them by

$$\delta = (Pf + b) + \nu. \tag{5.10}$$

If source and background photons are statistically independent, their contribution to δ is a Poisson r.v. with expected value given by:

$$E\{\delta\} = (Pf + b)_i. \tag{5.11}$$

All the δ_i associated to the different detector pixels, are statistically independent, so that:

$$p_\delta(d; f) = \prod_{i=1}^{M} p_{\delta_i}(d_i; f) = \prod_{i=1}^{M} \frac{e^{-(Pf+b)_i}(Pf + b)_i^{d_i}}{d_i!}. \tag{5.12}$$

Let $p_\delta(d; f)$ the known probability density of the data. Since the unknown object appears as a set of parameters, the image reconstruction problem appears as the classic parameter estimation problem. The standard approach is the ML estimation. The data density function is defined as the likelihood function

$$L(f) = p_\delta(d; f). \tag{5.13}$$

For a given detected image d, the only unknown in $L(f)$ is f. The ML estimate f_{ML} is the object which maximizes the probability of obtaining the observed image, i.e.

$$f_{ML} = \arg\max L(f). \tag{5.14}$$

Usually the likelihood function is the product of a very large number of factors, so that it is convenient to take the logarithm of $L(f)$. Moreover, if we consider the negative logarithm (the so-called neg-log), the maximization problem becomes a minimization one, i.e.

$$f_{ML} = \arg\min - \ln L(f), \tag{5.15}$$

Given the image d, using the Stirling's formula, we can approximate the neg-log of $L(f)$ with the Kullback-Leibler (KL) divergence $J_0(f; d)$ of the expected value $Pf + b$ from the data d:

$$- \ln L(f) = \sum_{i=1}^{M} [-d_i \ln(Pf + b)_i + (Pf + b)_i + \ln(d_i)!] \tag{5.16}$$

$$\approx \sum_{i=1}^{M} \left[-d_i + (Pf + b)_i + d_i \ln \frac{d_i}{(Pf + b)_i} \right] \equiv J_0(f; d).$$

It is a convex nonnegative functional, so that minimizers exist and are global. Furthermore, the minima of $J_0(f; d)$ coincide with those of $L(f)$.

Normalizing the PSF P in such a way that the sum of all the entries of each columns is equal to 1, the gradient and the Hessian matrices of $J_0(f; d)$ are given by:

$$\nabla J_0(f; d) = 1 - P^T \frac{d}{Pf + b}, \quad \nabla^2 J_0(f; d) = P^T \ diag \ \frac{d}{(Pf + b)^2} P \tag{5.17}$$

where for a cyclic matrix P, the arrays with the sum of the entries of each column of P are equal, because obtained by means of permutations of the elements of array P.

Thanks to the convexity of $J_0(f; d)$, the Karush-Kuhn-Tucker (KKT) conditions are necessary and sufficient for f_{ML} to be a global minimum of $J_0(f; d)$. From the stationarity condition $\nabla J_0(f; d) = 0$, one gets

$$f_{ML} \nabla J_0(f_{ML}; d) = 0 \Leftrightarrow f_{ML} = f_{ML} P^T \frac{d}{Pf_{ML} + b} \tag{5.18}$$

$$f_{ML} \geq 0 \qquad \nabla J_0(f_{ML}; d) \geq 0. \tag{5.19}$$

Now, Eq.5.18 can be written as a fixed point equation. The minima of $J_0(f; d)$ must be solutions of the following nonlinear equation:

$$(f_{ML})_j = (f_{ML})_j \left(P^T \frac{d}{Pf_{ML} + b} \right)_j, \quad j = 1, \ldots, N. \tag{5.20}$$

Eq.5.20 is the recursive formulation of the LR algorithm in presence of background radiation. In this case, the nonnegativity constraint is active only when this form of the iteration is used. Otherwise, ringing effects may appear in the reconstructed image.

By applying the method of successive approximations to Eq.5.20, the LR (or EM) iterative method is obtained:

$$f^{(r+1)} = f^{(r)} P^T \frac{d}{Pf^{(r)} + b}, \quad r = 0, 1, \ldots \tag{5.21}$$

5.4.3   Issues on LR algorithm

The iteration is, in general, initialized with a non-negative constant array. At each iteration, the reconstructed f will be non-negative. This property is linked to the superresolution, the capability to restore information beyond the diffraction limit. Furthermore, if a component of the solution is set to zero or becomes zero, it remains zero for all successive iterations.

An important property concerns the manner in which information is extracted from the data d as the iterative algorithm proceeds. The method is observed to converge rapidly on long wavelength features in the restored image f, while several thousand iterations are sometimes necessary to resolve high frequency detail [44] and [45].

Complete recovery of the object requires a large iteration number. In absence of noise, the procedure tends toward a perfect restoration. Due to noisy observation, the noise amplifies as iterations increase, so damaging the restored image from one iteration to another. Hence, restored image may become unacceptably noisy and unreliable for a large number of iterations. An analytical analysis of the noise amplification for nonlinear methods is difficult.

5.5   Bayesian methods

The classical formulation of ML problem seen in the previous section employs only information about the noise. No additional information about the object is considered, then the problem results to be still ill-posed.

Additional information may consist in bounds on the solution. They can be introduced in the problem as constraints in the objective function formulation. For example, this can be seen in the logaritmic term of Eq.5.6.

However, the completely probabilistic Bayesian approach includes the additional information ("prior") in the form of statistical properties of the unknown object. Priors allow the regularization of the classical ML solution f_{ML}.

In the Bayesian approach, other than the noise n and the data d, also the object f is a realization of a r.v. ϕ. Looking at the image formation equation (Eq.3.12), they are related by

$$\delta = (P\phi + b) + \nu. \tag{5.22}$$

The a-priori information is encoded into the prior probability density of ϕ, $p_\phi(f)$. It is the marginal density function of ϕ, i.e.

$$p_\phi(f) = \int p_{\phi\delta}(f, d)dd. \tag{5.23}$$

The most frequently used functions are Gibbs priors, i.e.:

$$p_\phi(f) = \frac{1}{Z}e^{-\mu\Omega(f)}, \tag{5.24}$$

where Z is a normalization constant, μ is the regularization parameter and $\Omega(f)$ is a functional describing prior information about the object. Examples of Gibbs priors are:

- $\Omega(f) = ||f||_2^2$ white noise prior;

- $\Omega(f) = ||\Delta f||_2^2$ smoothing prior;

- $\Omega(f) = ||f||_1$ impulse noise prior;

- $\Omega(f) = ||\nabla f||$ total variation prior.

The conditional probability density of δ when the r.v. ϕ assumes the value f (i.e. $p_\delta(d|f)$), can be deduced from the known statistical properties of the Poisson noise. If also the prior $p_\phi(f)$ is given, a complete knowledge of the

total probability $p_{\phi\delta}(f, d)$ is found.

Following the derivation in Appendix D, the conditional probability density of ϕ, called "a-posteriori" probability density, is given by:

$$P_d^{\phi}(f) \equiv p_{\phi}(f|d) = L(f)\frac{p_{\phi}(f)}{p_{\delta}(d)}, \qquad (5.25)$$

where $L(f)$ is the likelihood function of the previous section. The a-posteriori probability density provides all information we can get about the unknown object when we know its a-priori probability density $p_{\phi}(f)$ and the data. From the set of all possible estimates of the unknown object with their relative probabilities, an estimate of the object is provided by Eq.5.25.

In Bayesian statistics, a MAP estimate can be used to obtain an estimate of an unknown object on the basis of empirical data. The objective function $J(f; d)$ used in MAP optimization problem (Eq.5.26) incorporates a prior distribution over the quantity one wants to estimate. The choice of the regularization parameter μ influences the optimum image reconstruction.

The optimization problem to be solved for obtaining the f_{MAP} estimate of the unknown object is:

$$\min J(f; d) = J_0(f; d) + \mu J_R(f) \qquad (5.26)$$
$$s.t. \quad f \geq 0$$
$$\sum_{j=1}^{N} f_j = c,$$

where $J_0(f; d)$ comes from the neg-log likelihood function and $J_R(f)$ from the neg-log prior function. In Eq.5.26, the total flux consevation is introduced as a constraint. If $\mu = 0$, Eq.5.26 is just the ML problem, so we find the classical LR iterative formula (Eq.5.21).

From this point forward, thanks to the convexity of $J(f; d)$, the KKT conditions for a point f_{MAP} to be a global minimum can be employed to solve the MAP optimization problem (Eq.5.26) in the same way employed in ML.

Chapter 6

Results

At this point of this thesis, we have the theoretical basis to understand the results. The IBIS/ISGRI data using a pure geometrical PSF were simulated and decoded. The PSF takes into consideration only the effects of photon propagation through the aperture. Chapter 3 described the geometrical features of coded mask systems in detail. Chapter 4 was devoted to the system comprising the IBIS/ISGRI detector and the IBIS coded mask.

The choice of the decoding method used to restore the sky images affects the quality of the reconstruction. The achievable sensitivity and the maximum angular resolution must be checked to define the goodness of the restored image.

After a short description of the LR code, the deconvolved images obtained with both these methods will be shown and analysed. While in this chapter only the simulated IBIS/ISGRI data are dealt with, in the next one the real IBIS/ISGRI data will be deconvolved.

6.1 Deconvolution codes

The main drawback of the coded mask system telescopes for γ ray astronomy is their limited resolution. The usual technique used to deconvolve coded masks data is the cross-correlation. In the 90's T.P.Li and his collaborators proposed a new way to reconstruct γ ray sky images, the DD, based on a nonlinear optimization problem with linear-equality constraints.

To solve this optimization problem, Y. Chen et al. [16] proposed an interior point method. After the implementation of different techniques for the solution of the inverse problem, great attention was devoted to the Lucy-Richardson approach.

The CC IDL-based code was previously developed by J.B. Stephen of the

INAF-IASF of Bologna. Thanks to the precious collaboration with S. Bonettini and G. Zanghirati of the Mathematics Department of the University of Ferrara, the LR code was developed. Since Matlab offers a huge amount of optimization routines and in order to collaborate with the numerical optimization researchers in our University, Matlab was chosen to implement the CC and it was used as the working environment.

6.1.1   Data and decoding array

The CC deconvolves the data with a decoding array obtained by the $95{\times}95$ elements aperture. In input, data are given in units of cts cm^{-2} s^{-1} for both the simulated and real cases.

A typical simulated data distribution is shown at the left hand side of Fig. 6.1. It consists of a $128{\times}128$ array of photon counts over a $130{\times}134$ physical support (due to the gaps between element modules). The data take into account also dead pixels, i.e. the bad working pixels which are switched off. The flux at the module gaps and dead pixels is posed equal to 0.
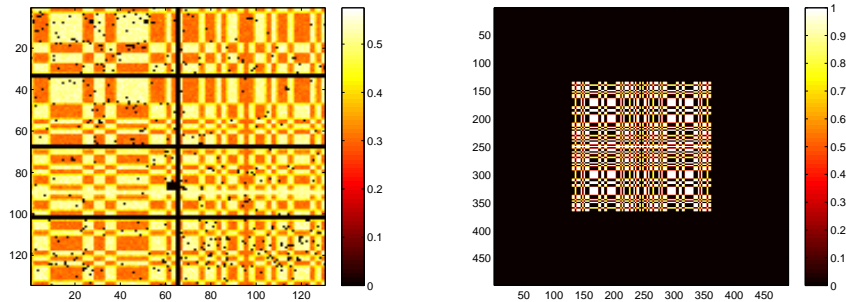
Figure 6.1 A typical data distribution (left) and the PSF (right) of the IBIS instrument. Data are also called shadowgram and PSF decoding array.

The CC code can simulate more than one source in the FOV, for each of which the position in the sky and the flux can be chosen. Data are resampled to the mask element FCFOV resolution.

The Poisson background distribution is created giving as input the mean value around which it is built in units of cts s^{-1}. Before adding the background to the simulated data, both these radiations must have the same units of cts in each detector pixel, so the data initial value must be multiplied by the ISGRI pixel area (i.e. $0.46^2{=}0.2116$ cm^2) and the observation time (i.e. 2150 s). For instance, a value of 0.03 cts s^{-1} cm^{-2} becomes 13.97

cts for each pixel.

The initial background value must be multiplied by the observation time and divided by the number of ISGRI pixels (i.e. 128×128=16384 without gap between modules but including dead pixels). For instance, the input value of 5000 cts s^{-1} is normalized to:

$$BKG = \frac{5000 \times 2150}{16384} = 656.13 \ cts \tag{6.1}$$

for each pixel. Around this normalized background value the Poisson distribution is created. It will be the "usual background" used in all simulated data of this chapter.

After the addition of the background radiation to the source, the resulting data must be renormalized to the units of cts s^{-1} before proceeding with the balanced cross-correlation deconvolution.

The PSF (right hand side of Fig. 6.1) is obtained by the mask pattern resampled at the same level as the data, zero-padded to the correct size.

6.1.2 The LR code

Since the deconvolved images must be in the same units in both CC and LR, before using the LR, data must be normalized to cts s^{-1} cm^{-2}, so the input data to the LR were divided for the area of one ISGRI pixel.

As said, the value of the source peak deconvolved with CC is a good estimate of the source real flux. Given that the LR code belongs to the class of non-linear techniques, the source flux estimation with this decoding algorithm represents a huge problem, mainly due to the choice of the correct iteration number. Too many iterations could amplify noise fluctuations to the detriment of the goodness of source flux estimate and, as a consequence, of the quality of the reconstruction. In advanced numerical analysis, stopping criteria, mainly based on the residuals analysis, are developed even if the choice of a general stopping rule remains today an open issue in Non-Linear optimization Problems (NLPs).

Furthermore, an iteration number which could be optimum for a source of given flux, may not be for a fainter one. This situation could be met in crowded sky regions as, for example, the Galactic Centre.

Extreme care must be used when we deal with the PCFOV. The shadow-gram of a PC source contains less data counts (i.e. less statistics), so the reconstruction of a PC source could be less precise. Furthermore, coding noise from both FC and PC sources is diffused also over the PCFOV.

As said in Chapter 5, there are two main inputs to be provided to the LR code: an initial sky image and the iteration number.

As an initial point, the LR takes an image of the decoded sky size with all positive entries. To simplify the computation, it is normalized in such a way that the sum of the entries of each column is equal to 1.

Also the background b must be initialized. For real data, the initial b is chosen to be 90% the mean value of all data counts. In the simulation, instead, the input b value is normalized to the ISGRI pixel area, in units of cts s^{-1} cm^{-2} as the data.

The initial estimate of the correct iteration number was found by trial and error. Two hundred LR iterations were found to provide a good trade-off between image reconstruction and noise propagation with both simulated and real data. In the following, 200 LR iterations were performed for all analysis. The LR restores the $(r+1)-th$ image, $f^{(r+1)}$, as

$$f^{(r+1)} = f^{(r)} P^T \frac{d}{Pf^{(r)} + b},$$ (6.2)

where $f^{(r)}$ is the deconvolved image of the previous iteration or, for the first iteration, the initial image.

The LR code exploits the properties of the Fourier transform to compute the convolution $Pf^{(r)}$ by Fast Fourier Transform (FFT), so allowing to save computation time.

6.2 Flux reconstruction

The nonlinear nature of the LR affects the quality of the deconvolved images. The number of iterations performed is the limiting factor to the goodness of the reconstructed source flux. The 200 LR iterations used in all this thesis were chosen by trial and error, so it is necessary to know when this iteration number is able to well reconstruct the source real flux.

To do it, the behaviour of the deconvolved source flux as the source becomes brighter was studied. The system of a point source of increasing flux (i.e. from 0 to 0.1 cts s^{-1} cm^{-2}) superimposed on a 1.45 cts s^{-1} cm^{-2} Poisson background is decoded using two hundred LR iterations. For each source flux value, a sample of 100 runs was created and the mean deconvolved flux was computed.

Fig. 6.2 shows the behaviour of the reconstructed source flux as the source becomes brighter for both CC and LR.
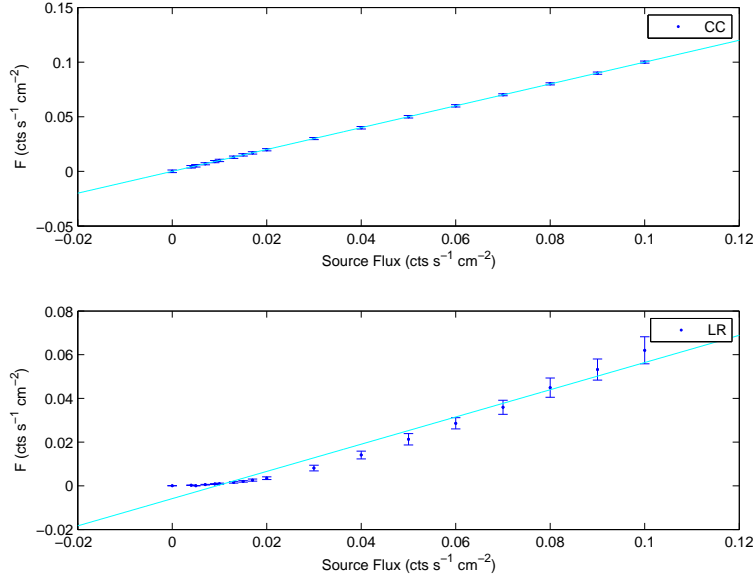
Figure 6.2 Reconstructed flux distribution in the case of a source of increasing flux for both CC (up) and LR (bottom).

The CC reconstructed flux gives a good estimate of that of the real source independently on its strength. It linearly increases as the source becomes brighter. The uncertainty of the reconstruction is independent on the real flux value.

For sources stronger than 1.4% the initial background (i.e. 0.02 cts s^{-1} cm^{-2}), the LR reconstructed flux linearly increases as the source becomes brighter. For sources fainter than 0.02 cts s^{-1} cm^{-2}, the LR evaluation is more variable. An exponential model better describes the recovered flux in the whole real source flux interval, even if, for sources stronger than 0.02 cts s^{-1} cm^{-2}, the fit residuals of the linear model are of the same order of magnitude as those of the exponential one. The followed linear fit model is expressed as

$$p_1 x + p_2. \tag{6.3}$$

Tab. 6.1 reports the fit coefficients with their 95% confidence bounds for both deconvolution algorithms.

For sources fainter than 7% the background (i.e. 0.1 cts s^{-1} cm^{-2}) and 200 LR iterations performed, the reconstructed source flux always underes-

Algorithm	p_1	p_2
CC	1 (0.998, 1.001)	$3.49\ 10^{-5}$ ($-3.25\ 10^{-5}$, $1.02\ 10^{-4}$)
LR	0.62 (0.57, 0.68)	$-5.87\ 10^{-3}$ ($-8.44\ ^{-3}$, $-3.3\ ^{-3}$)

Table 6.1 The fit coefficients of the distributions in Fig. 6.2. Between round brackets there are their 95 % confidence bounds.

timates its real value. For example, the reconstructed source flux of the 0.1 cts s^{-1} cm^{-2} source (i.e. 7% the initial background) is 60% its real value. Preliminary results show as two thousand LR iterations give a reconstructed flux 93% its real value.

To better compare the deconvolved fluxes obtained with both techniques, the normalized residual flux is computed as:

$$F_{norm} = \frac{F_M - F_R}{F_R},\qquad(6.4)$$

where F_M and F_R are reconstructed and real flux, respectively.

Fig. 6.3 shows normalized flux distributions for both CC (red) and LR (blue). They fit the exponential model defined as

$$a\exp(bx),\qquad(6.5)$$

whose coefficients with their 95% confidence bounds are reported in Tab.6.2.

Algorithm	a	b
CC	0.13 (-0.07, 0.34)	-375.1 (-694.7, -55.56)
LR	-1.00 (-1.01, -0.99)	-10.35 (-10.87, -9.82)

Table 6.2 The fit coefficients of the normalized fluxes of Fig. 6.3. Between round brackets there are their 95 % confidence bounds.

Again, it is clear as the CC reconstructed source flux is a good estimate of its real value. The CC normalized residual flux always does not gain or lose flux. For sources fainter than 1.4% the initial background radiation, its value is more uncertain than that obtained for stronger sources. On the other hand, the LR normalized residual flux always underestimates its real value for two hundred LR iterations.

Preliminary results show as for a 21% the initial background radiation source (i.e. 0.3 cts s^{-1} cm^{-2}), the normalized residual flux is about zero and its reconstructed flux is 93% its real value. As the source real flux approaches 69% the background radiation (i.e. 1 cts s^{-1} cm^{-2}), the normalized residual flux exponentially approaches the zero value.
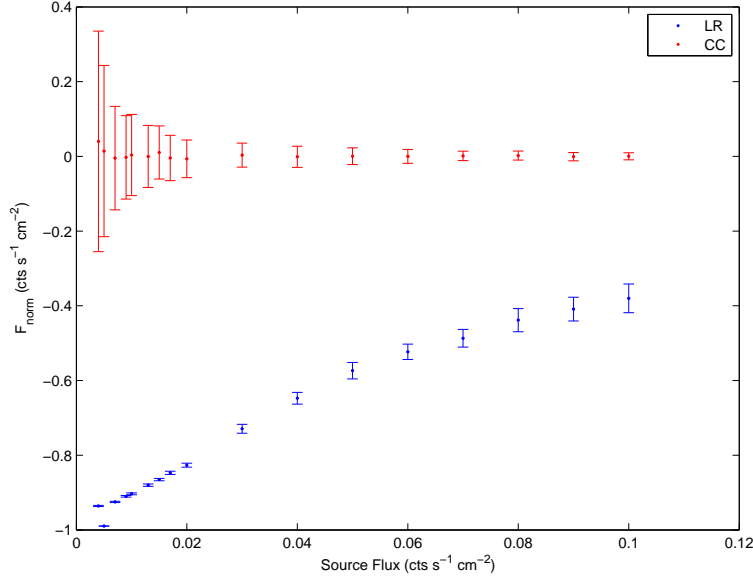
Figure 6.3 Normalized source residual flux F_{norm} as a function of the source real flux for both CC (red) and LR (blu).

The sources analysed in this section (i.e. fainter than 7% the input background) are in the ascending part of the exponential model describing the 0-1 cts s^{-1} cm^{-2} flux interval. For them, two hundred LR iterations are not enough to give a good evaluation of their real flux.

6.2.1 Impact of the iteration number

The correct choice of the iteration number affects the reconstructed flux values. This is true in both source and ghost peaks case. In this section the source flux behaviour is analised, while Sect. 6.5 will go into details of that of the ghost total flux.

The reconstructed flux as the number of iterations increases from 1 to 2000 is analysed simulating the system of a source of constant 0.1 cts s^{-1} cm^{-2} flux (7% the initial background) superimposed on the usual Poisson background. The deconvolved source flux normalized to its real value (see Fig. 6.4) follows the sum of two exponentials model, defined as

$$a \exp(bx) + c \exp(dx). \tag{6.6}$$

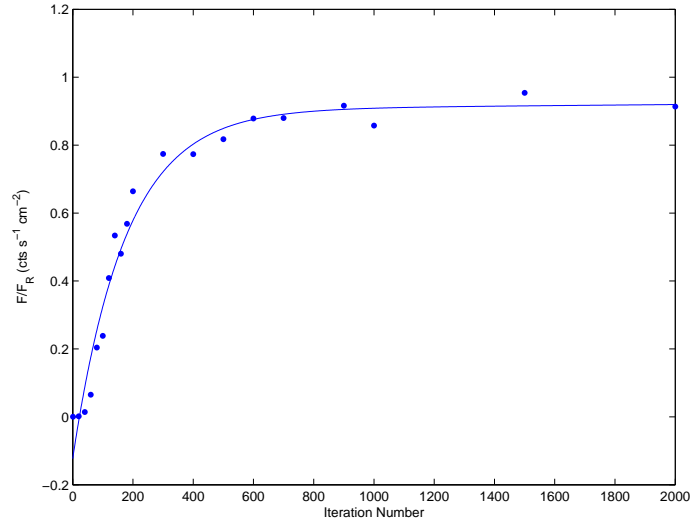The fit coefficients with their 95% confidence bounds are reported in Tab.6.3.

Figure 6.4 Reconstructed source flux normalized to its real value.

a	b	c	d
0.90 (0.75, 1.05)	$8.21 \ 10^{-6}$ ($-1.23 \ 10^{-4}$, $1.4 \ 10^{-4}$)	-1.03 (-1.18, -0.87)	-0.006 (-0.007, -0.004)

Table 6.3 The fit coefficients of the source reconstructed flux in Fig. 6.4. Between round brackets there are their 95 % confidence bounds.

For a source of flux equal to 7% the initial background, two hundred LR iterations reconstruct only 60% its real flux. As the iteration number increases, the reconstructed flux approaches its real value. One thousand LR iterations recover about 90% the source real flux. The flux reconstruction in the LR is slow, so a big number of iterations is necessary to be able to give a good estimate of the real flux.

It is reasonable thinking that, to accurately reconstruct the flux of faint sources, more iterations are necessary, while a good flux estimate of strong sources needs less computation time. For instance, 2000 LR iterations require about 6 minutes time, while 200 about 30 seconds.

6.2.2   Minimum detectable flux

In hard-X/soft-γ rays, background radiation is of the same order of magnitude as the source signal. By the analysis shown in previous sections, the capability of two hundred LR iterations to reconstruct faint objects could be faced up.
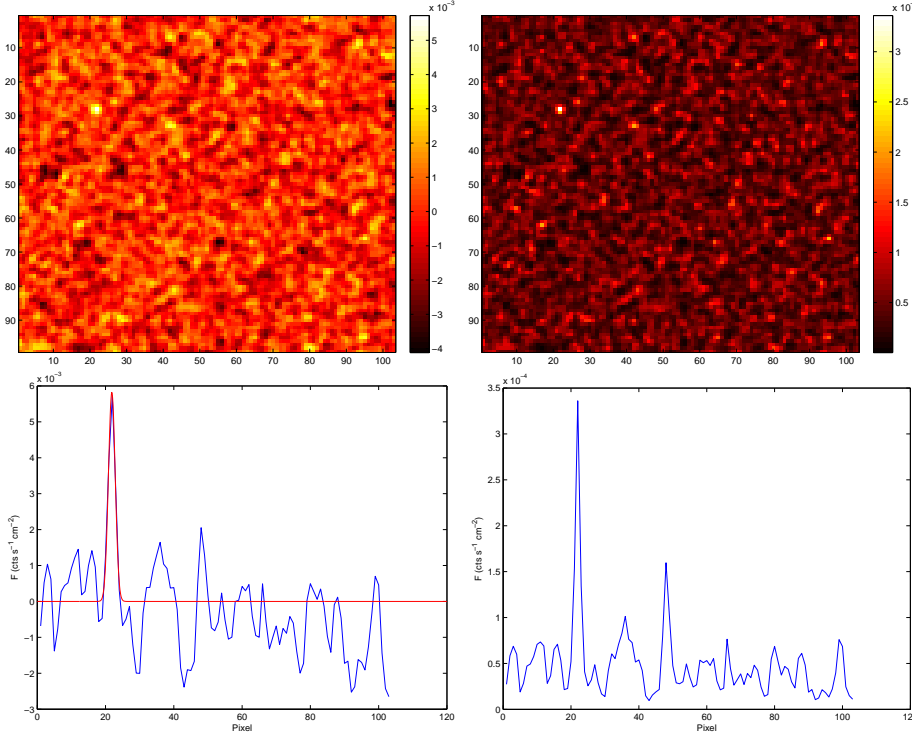
Figure 6.5 Upper panel: deconvolved FCFOV images in the case of minimum detectable source. Bottom panel: source profiles. At the left hand side there are CC results, while at the right hand the LR one.

Independently on the reconstructed source flux, two hundred LR iterations are able to restore a 0.005 cts s^{-1} cm^{-2} source (i.e. of 0.3% the initial background) superimposed on the usual Poisson background, whose sensitivity is around 5.6σ. As can be seen in Sect. 6.4, while the CC found SNR (see Eq.4.9) is consistent with the sensitivity, the LR underestimates it. This is mainly due to the fact that two hundred LR iterations are able to recover only 8% real source flux, while CC gives a confident estimate. Fig. 6.5 shows the deconvolved FCFOV images for both CC (left) and 200 LR iterations (right). The source profiles in Fig. 6.5 fit the Gaussian model defined as

$$a \exp\left(-\frac{(x-b)^2}{2\sigma^2}\right), \qquad (6.7)$$

where the fit coefficients a, b and σ give the flux, the position and the 1σ error from the position of the reconstructed source, respectively. The fit coefficients with their 95% confidence bounds are reported in Tab. 6.4. A

narrow interval around the LR peak must be selected to guarantee the fit convergence, with a consequent increase in the location accuracy uncertainty (i.e. σ parameter in Tab. 6.4).

Algorithm	a (cts s^{-1} cm^{-2})	b (pxl)	σ (pxl)
CC	5.83 10^{-3} (3.75 10^{-3}, 7.89 $^{-3}$)	21.85 (21.44, 22.26)	0.99 (0.59, 1.40)
LR	2.87 10^{-4} (2.03 10^{-4}, 3.72 10^{-4})	22 (21.64, 22.36)	1.05 (0.69, 1.40)

Table 6.4 The fit coefficients of the profiles in Fig. 6.5. Between round brackets there are their 95 % confidence bounds.

The probability to reconstruct fluctuations as if they are real sources increases as the source flux becomes fainter. A source flux equal to 0.3% the initial background radiation is the limiting flux for which the LR algorithm is able to unequivocaly reconstruct and locate the source peak (see the b parameter in Tab. 6.4), independently on the reconstructed flux. Indeed, false peaks are not reconstructed neither in CC nor in LR FCOFV images (Fig. 6.5). Both deconvolution codes locate the source at the correct position with the same location accuracy.

A look at the total FOV reveals the existence of ghost peaks superimposed on the fluctuating reconstructed background. Fig. 6.6 shows the total FOV profiles taken along the horizontal axis crossing the source for both CC (left) and LR (right). Ghosts are visible at pixels 22 and 280, while the source is at pixel 151 in both cases. The CC left hand side ghost is confused between the noisy boundary of the total FOV. It is not strange that this region shows spikes due to an increase in uncertainty. At the total FOV boundary, statistics are poorer, so error increases. The ghost behaviour will be studied in Sect. 6.5.

6.3   The background in reconstructed images

To estimate the SNR, an evaluation of the mean and the standard deviation of the background used in all simulated analysis must be computed. Furthermore, the statistical nature of the reconstructed background radiation in the LR decoded images must be verified.

In images of sparse objects the majority of the pixels contains only background. The distribution of the counts of the deconvolved FCFOV images (see Fig. 6.7) follows the expected Gaussian shape. The standard deviation from the position of the Gaussian peak (i.e. the σ and b parameters in Tab. 6.5) give us an estimate of the background dispersion in the restored images
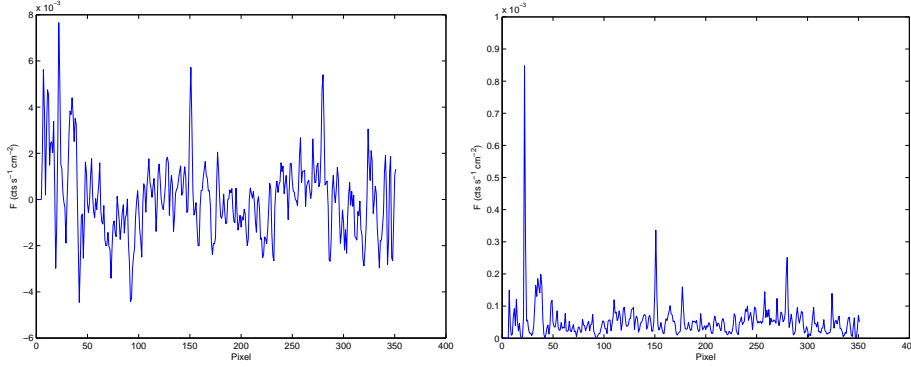
Figure 6.6 Total FOV profiles in the case of minimum detectable source for both CC (left) and LR (right). The source is located at pixel 151, while the ghosts at pixels 22 and 280.

[81]. If sources are present, they are located at the right hand side of the background Gaussian peak.

The input background radiation in the simulated fields of this thesis was kept to the constant value of 656 cts for each of the 16384 ISGRI pixels (see Eq. 6.1). By definition, the balanced cross-correlation applies weights to the decoding array in such a way that the mean value of the background flux is reduced around zero value. For ideal detector and perfect mask sampling (i.e. without gaps, dead pixels, ecc), the purely statistical expected standard deviation from the mean background should be equal to

$$\sqrt{16384 \times 656} = 3279 \; cts \tag{6.8}$$

or, equivalently,

$$\frac{3279}{2150 \times 16384 \times 0.21} \approx 4.4 \; 10^{-4} \; cts \; s^{-1} \; cm^{-2}. \tag{6.9}$$

However, the PSF used in our codes is far from a pure δ function. The decoding array (i.e. the PSF) includes dead pixels and gaps between modules. Furthermore, in the theoretical case, the decoding array should have integer values equal to +1 or -1. The multiplication by the weighting factor W in Sect. 3.4.1 changes the integer value of the decoding array elements into a not-integer one between -1 and +1. Both these issues cause an increase in the expected standard deviation of Eq. 6.9.

The background distribution was fitted with the Gaussian model defined in Eq. 6.7, where the fit coefficients a, b and σ now give the amplitude, the

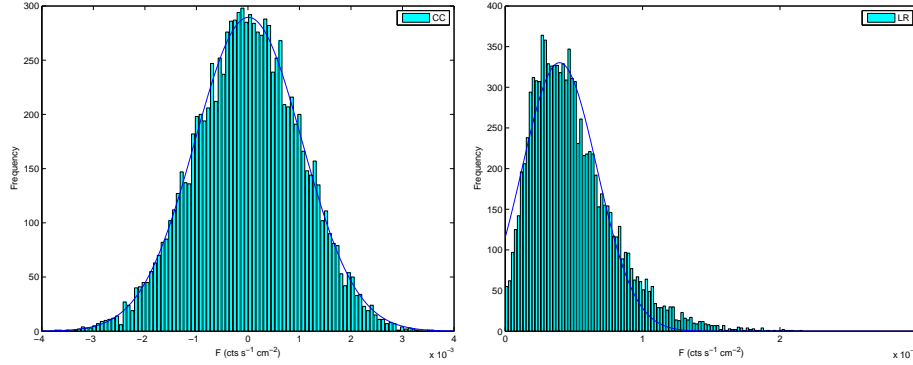position and the 1σ error from the position of the background distribution, respectively.

Figure 6.7 Distribution of FCFOV counts for a pure background field deconvolved with both CC (left) and 200 LR iterations (right).

Algorithm	a	b (cts s^{-1} cm^{-2})	σ (cts s^{-1} cm^{-2})
CC	289.5 (285, 294)	1.07 10^{-5} (-7.86 10^{-5}, 2.93 10^{-6})	1.04 10^{-3} (1.02 10^{-3}, 1.06 10^{-3})
LR	330.3 (317.2, 343.3)	3.96 10^{-5} (3.82 10^{-5}, 4.09 10^{-5})	2.73 10^{-5} (2.58 10^{-5}, 2.87 10^{-5})

Table 6.5 The fit coefficients of the distributions in Fig. 6.7. Between round brackets there are their 95 % confidence bounds.

While the CC background distribution is well fitted by a symmetric Gaussian model, in the LR it is asymmetric. However, with a smaller number of iterations (see Fig. 6.8), the LR background distribution has a more symmetric shape. By decreasing of the number of iterations, the mean increases while the standard deviation decreases (see Tab. 6.6).

Iter. Numb.	a	b (cts s^{-1} cm^{-2})	σ (cts s^{-1} cm^{-2})
100	317 (309.8, 324.1)	5.05 10^{-5} (5.00 10^{-5}, 5.10 10^{-5})	1.84 10^{-5} (1.79 10^{-5}, 1.87 10^{-5})
50	302.3 (297.8, 306.8)	5.24 10^{-5} (5.33 10^{-5}, 5.35 10^{-5})	6.27 10^{-6} (6.16 10^{-6}, 6.38 10^{-6})

Table 6.6 The fit coefficients of the distributions in Fig. 6.8. Between round brackets there are their 95 % confidence bounds.

Looking at σ in Tab. 6.5, the CC standard deviation is two and a half times bigger than the expected value in Eq. 6.9. The LR standard deviation is a factor of 100 smaller than that found with CC. The LR background fluctuations are smaller than the CC one and, as a consequence, the background is flatter.
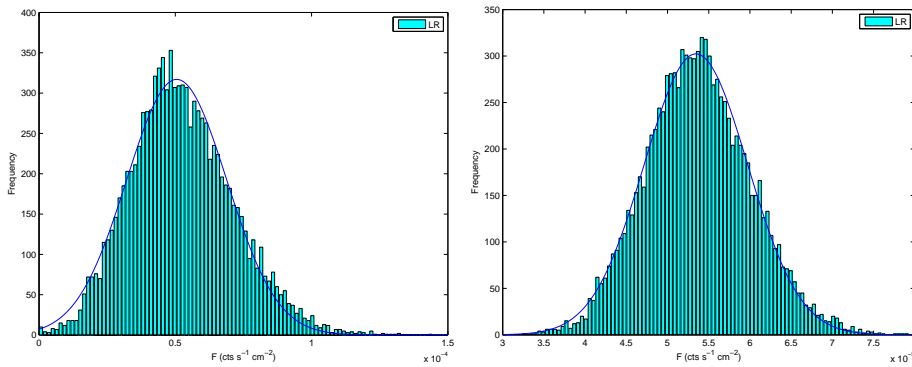
Figure 6.8 LR distributions of FCFOV counts for a pure background field deconvolved by 100 (left) and 50 (right) LR iterations.

To understand the statistical nature of the background radiation in LR deconvolved images, i.e. if the standard deviation in Tab. 6.5 is an estimate of the statistical fluctuations due to the background, the behaviour of the same pixel in a sample of 100 independent runs is studied. Also in this case, each pure background field was deconvolved with two hundred LR iterations. Fig. 6.9 shows the frequency distributions of the same pixel flux obtained over 100 independent runs for both CC (left) and LR (right).
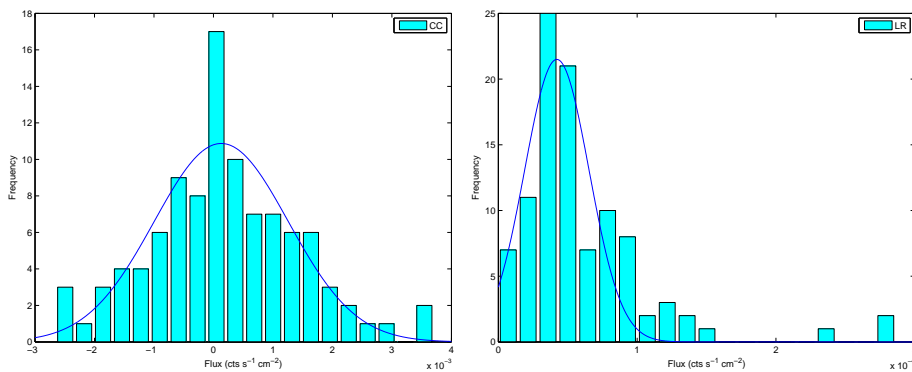

Figure 6.9 Frequency distributions of the statistical uncertainty in the case of pure background field for both CC (left) and LR (right).

The 1σ error of the single run (see Tab. 6.5) gives the interval inside which the mean in Tab. 6.7 must be found. This is true in both algorithms, as can be seen comparing the mean b in Tab. 6.7 and the standard deviation σ of the single run in Tab. 6.5.

Algorithm	a	b (cts s^{-1} cm^{-2})	σ (cts s^{-1} cm^{-2})
CC	10.87 (8.83, 12.91)	1.31 10^{-4} (-1.14 10^{-4}, 3.75 10^{-4})	1.1 10^{-3} (9 10^{-4}, 1.4 10^{-3})
LR	21.49 (16.95, 26.04)	4.21 10^{-5} (3.64 10^{-5}, 4.79 10^{-5})	2.33 10^{-5} (1.72 10^{-5}, 2.93 10^{-5})

Table 6.7 The fit coefficients of the frequency distributions in Fig. 6.9. Between round brackets there are their 95 % confidence bounds.

This confirms that the standard deviation in the CC and LR is an estimate of the statistical uncertainty. The data are statistically independent, as their deconvolved images.

The LR standard deviation of the single run is too small to describe the statistical behaviour of the Poisson background in the deconvolved images. The analysis of the pixel with the maximum reconstructed flux could give information about this. The maximum flux pixel in the deconvolved image could be a fluctuation that is reconstructed as if it is a real source. If the standard deviation of the single run is representative of that obtained from the distribution of the maximum flux pixel, the deconvolution algorithm has statistical meaning and the maximum flux pixel does not represent the reconstruction of a fluctuation.

The maximum flux pixel distribution over 100 independent runs found with our codes are shown on the right hand side of Figs. 6.10 and 6.11, while their fit parameters with their 95% confidence bounds are reported on the second line of Tabs. 6.8 and 6.9.

Assuming that the standard deviation σ of the single run has statistical meaning, the expected Gaussian distribution over a sample of 100 independent runs is created. By the comparison of the expected fit parameters and those obtained from the real distribution (see Tab. 6.8) it can be seen as the CC mean and standard deviation have the expected values. This confirms the statistical nature of this deconvolution method.

	a	b (cts s^{-1} cm^{-2})	σ (cts s^{-1} cm^{-2})
Expected Dist.	18.28	3.91 10^{-3}	2.05 10^{-4}
Real Dist.	13.66 (11.23, 16.08)	3.91 10^{-3} (3.85 10^{-3}, 3.97 10^{-3})	2.77 10^{-4} (2.19 10^{-4}, 3.34 10^{-4})

Table 6.8 The fit coefficients of the CC distributions in Fig. 6.10.

However, this is not the LR case. Indeed, the standard deviation of the expected and the real distributions (left and right hand side of Fig. 6.11, respectively) differs of a factor of

$$D = \frac{8.98 \ 10^{-5}}{7.86 \ 10^{-6}} \approx 11.42. \tag{6.10}$$
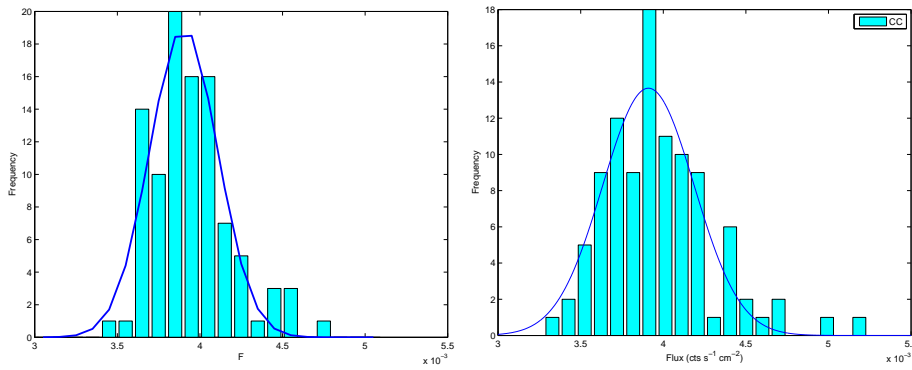
Figure 6.10 Left panel: the expected CC frequency distribution of the maximum flux pixel for 100 runs. Right panel: the real CC frequency distribution of the maximum flux pixel for 100 runs.

The LR algorithm shows statistical behaviour but the nonlinear nature of this algorithm makes the background too flat. When the standard deviation of the background distribution is used to compute the SNR, the LR 1σ value in Tab. 6.5 will be multiplied by the factor D.
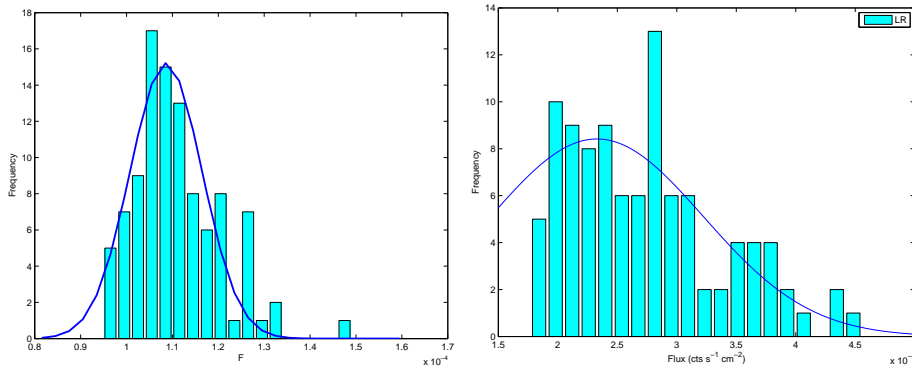

Figure 6.11 Left panel: the expected LR frequency distribution of the maximum flux pixel for 100 runs. Right panel: the real LR frequency distribution of the maximum flux pixel for 100 runs.

For a 1.45 cts s^{-1} cm^{-2} initial Poisson background distribution, the statistical uncertainty due to background radiation in the deconvolved images is of the order of 10^{-3} cts s^{-1} cm^{-2} for CC and, if two hundred LR iterations are performed, of a few $2.73\ 10^{-5} \times 11.42 \approx 3.12\ 10^{-4}$ cts s^{-1} cm^{-2} for LR. However, the analysis of the background standard deviation and of the D factor requires to be more accurately studied, in particular when a source

Algorithm	a	b (cts s^{-1} cm^{-2})	σ (cts s^{-1} cm^{-2})
Expected Dist.	14.45	1.09 10^{-4}	7.86 10^{-6}
Real Dist.	8.42 (6.714, 10.12)	2.33 10^{-4} (1.88 10^{-4}, 2.77 10^{-4})	8.98 10^{-5} (4.81 10^{-5}, 1.31 10^{-4})

Table 6.9 The fit coefficients of the LR distributions in Fig. 6.11.

of given flux is present in the FOV.

Furthermore, since the estimate of the background distribution parameters depends on the number of iterations (see Tab. 6.6), this factor must be computed every time the iteration number is changed.

6.4   Sensitivity

To measure the quality of a deconvolution method, the behaviour of the SNR (Eq.4.9) as a function of source flux must be studied. The system of a point source of increasing flux (i.e. from 0 to 0.1 cts s^{-1} cm^{-2}) superimposed on the usual Poisson background is analysed. For each source flux value, a sample of 100 independent runs was created. For each run, two hundred LR iterations are performed.

Fig. 6.12 show the found SNR (Eq.4.9) as a function of the source flux for both CC and LR. The red points are the expected theoretical source significance (Eq.4.7) as a function of the source increasing flux.

On the whole flux interval analysed in this section, the CC found SNR follows the expected linear increase as the source becomes brighter. For sources brighter than 1.4% the initial background (i.e. 0.02 cts s^{-1} cm^{-2}), also the LR found SNR is well described by a linear model as the source flux increases. For sources fainter than 1.4% the initial background, the LR found SNR underestimates the expected tss. The coefficients of the linear fit (see Eq.6.3) with their 95% confidence bounds are reported in Tab.6.10.

Algorithm	p$_1$	p$_2$
CC	930.8 (925.5, 936.3)	0.44 (0.18, 0.69)
LR	1458 (1316, 1601)	-11.52 (-18.18, 14.86)

Table 6.10 The fit coefficients of the distributions in Fig. 6.12. Between round brackets there are their 95 % confidence bounds.

In a perfect imaging system, the CC gives reconstructed flux less significant than the expected value. The CC error on the evaluation of the found SNR is independent on the source real flux.
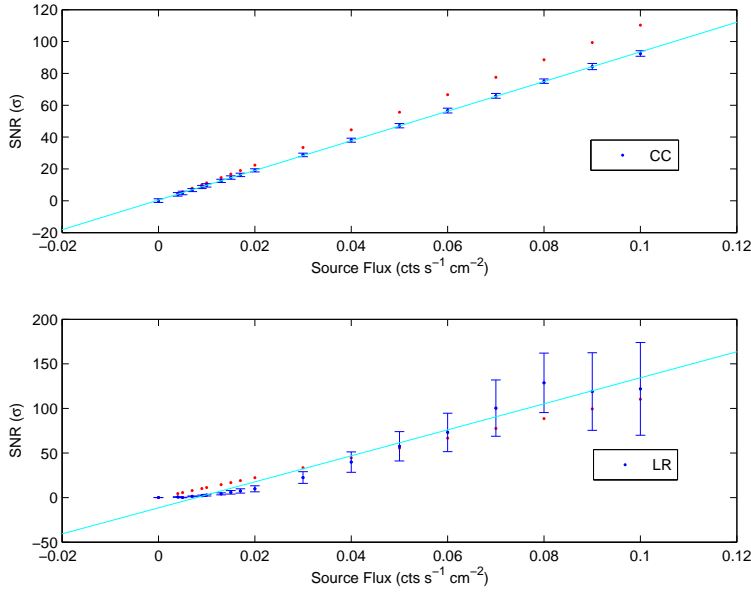
Figure 6.12 Found SNR distribution for the simulation of a source of decreasing flux for both CC (up) and LR (bottom). In red is the expected tss.

The LR found SNR is corrected for the D factor in Eq. 6.10, i.e. the expected value of the background standard deviation is used. For sources fainter than 1.4% the initial background (i.e. 0.02 cts s^{-1} cm^{-2}), the found SNR underestimates the expected value. This is probably due to the fatc that the reconstructed flux is underestimated more for these sources than for the stronger one.

For sources stronger than 1.4% the initial background, the found SNR is of the same order of magnitude of the expected sensitivity, even if its uncertainty increases as the source becomes brighter.

For example, for 200 LR iterations, the expected sensitivity and the CC found SNR for a 0.1 cts s^{-1} cm^{-2} source (i.e. 0.7% the intial background) are around 110σ and 93σ respectively, while the LR found SNR is around 130σ with error bars of 50σ.

For the field of a 1 cts s^{-1} cm^{-2} flux source superimposed on the usual Poisson background, two hundred LR iterations give a good estimate of the source flux. Preliminary results show that the LR found SNR is around 800 ± 53 σ, while the expected tss is around 996σ.

6.5   Ghosts

Ghosts appear for both FC and PC sources. While the ghosts of a FC source are in the PCFOV, sources in the PCFOV could give rise to ghost peaks also in the FCFOV. The choice of a deconvolution method affects the ghost strength, while their location is ruled only by the mask geometry, independently on the decoding algorithm used. They appear in both CC and LR deconvolved images. The implementation of their removal requires to study the behaviour of their intensity.

Fixed the iteration number to 200, by the simulation of a source of increasing flux (from 0.01 to 1 cts s^{-1} cm^{-2} or from 0.7% to 70% the background flux) superimposed on the usual Poisson background, it is clear as the source flux affects the total strength of ghosts. Fig. 6.13 shows the ghost total flux normalized to the source real flux as a function of the source real flux itself. For sources fainter than 7% the background (i.e. 0.1 cts s^{-1} cm^{-2}), the ghost total flux is more than 50% the real source. It exponentially decreases as the source becomes brighter. The coefficients of the exponential fit (Eq. 6.5) with their 95% confidence bounds are reported in Tab. 6.11.

Sources brighter than 70% the initial background radiation are not representative of the common situation found in the X ray sky. Indeed, using the same background radiation and increasing the source flux until 10 cts s^{-1} cm^{-2}, the reconstructed source flux gives a good estimate of its real value and ghost total flux is negligible.
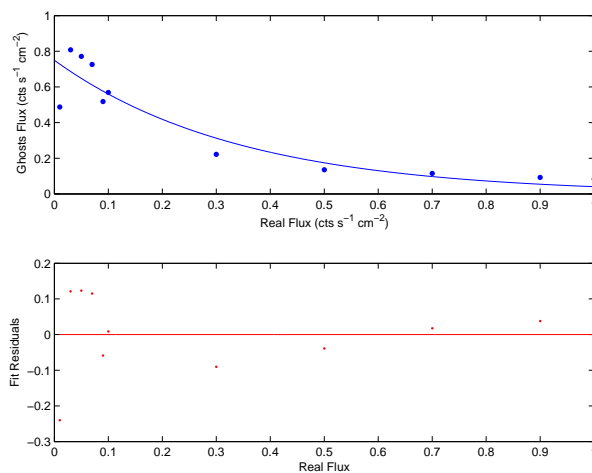

Figure 6.13 Normalized ghost total flux distribution for the simulation of a decreasing flux source. At the bottom, fit residuals are shown.

a (cts s^{-1} cm^{-2})	b
0.75 (0.63, 0.87)	-2.91 (-4.30, -1.52)

Table 6.11 The fit coefficients of the distribution in Fig. 6.13. Between round brackets there are their 95 % confidence bounds.

If another source of constant 0.01 cts s^{-1} cm^{-2} flux (called B) is added to the previous field of the increasing flux source A superimposed to the usual Poisson background, the behaviour of the source A ghost total flux does not change so much (see Tabs.6.11 and 6.12). It is not affected on the presence of another resolved source in the FOV.

Fig.6.14 shows the ghost total flux for both sources A and B as a function of the source A real flux. Both these distributions fit the exponential model of Eq. 6.5, whose coefficients with their 95% confidence bounds are reported in Tab. 6.12.

	a (cts s^{-1} cm^{-2})	b
A	0.84 (0.73, 0.95)	-3.51 (-4.84, -2.18)
B	0.57 (0.45, 0.69)	-0.78 (-1.42, -0.15)

Table 6.12 The fit coefficients of the distributions in Fig.6.14 for both source A and B. Between round brackets there are their 95 % confidence bounds.

As the source A flux increases, the ghost total flux of both sources becomes fainter more quickly for source A than for source B. The ghost total flux of source A becomes negligible respect to its real flux at about 1 cts s^{-1} cm^{-2}, while that of source B is about 10% of the real source A flux.

6.5.1 Impact of the iteration number

The LR has not information about the false nature of the ghosts, so it reconstructs them as if they are real sources. While in Sect. 6.2.1 was shown the impact of the iteration number onto the goodness of the source reconstructed flux, this section studies at the same way what happens to the ghost flux.

The same simulation of Sect. 6.2.1 was performed (i.e. the system of a source of constant 0.1 cts s^{-1} cm^{-2} flux superimposed on the usual Poisson background as the number of iterations increases from 1 to 2000). For details about the reconstructed source flux see Fig. 6.4 and Tab. 6.3.

As the iteration number increases, the ghost total flux normalized to the source real flux (in red in Fig. 6.15) follows the sum of two exponentials
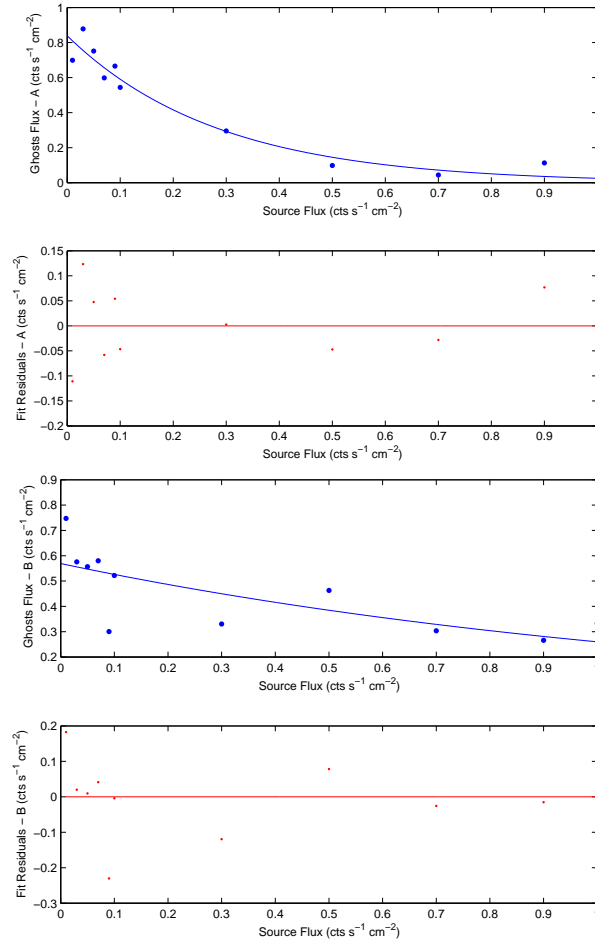
Figure 6.14 Ghost total flux distribution for sources A (up) and B (bottom). At the bottom, fit residuals are shown.

model as the source reconstructed flux (in black in Fig. 6.4), but with different fit coefficients (see Tab. 6.13).

As said, the CC ghosts have the same strength as the deconvolved source and, since the CC always gives consistent estimates of the real source, the CC false peaks have the same flux as the source. On average, each of the 8 LR ghost is fainter than that of the CC false peaks.

The ghost total flux exponentially increases until the reconstructed flux of the source is 70% its real value and, then, it slowly decreases going asymptotically to zero.

For two hundred LR iterations, the ghost total flux is around 65% the real source, i.e. each false peak is about 8% the real source. The reconstructed source flux is about 50% its real value. When the LR reconstructed about
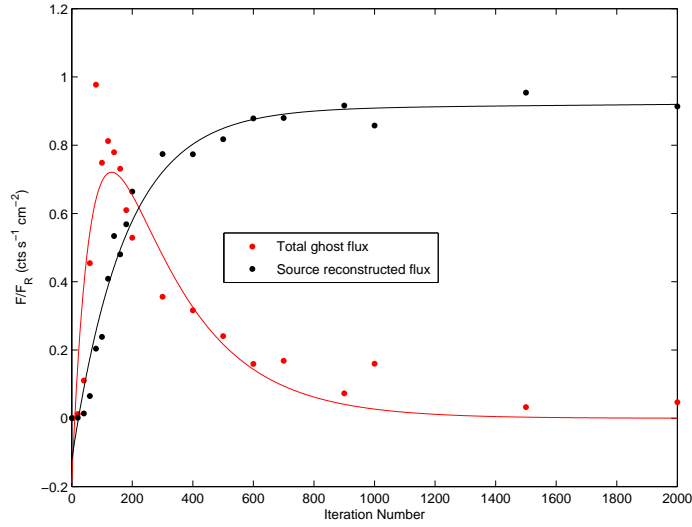
Figure 6.15 Ghost total flux (red) and reconstructed source flux (black) both normalized to the source real flux.

a	b	c	d
-1.96 (-4.48, 0.55)	-0.01 (-0.03, 0.001)	1.77 (-0.82, 4.37)	-0.004 (-0.008, -3.57 10^{-4})

Table 6.13 The fit coefficients of the ghost total flux in Fig. 6.15. Between round brackets there are their 95 % confidence bounds.

90% the source real flux (i.e. for 1000 LR iterations), the ghost total flux is negligible with respect to the real source flux.

For the moment, the ghost flux behaviour after the complete recovery of the source flux was not studied yet. It will be one of our future work.

6.6 Reconstruction capability in the PCFOV

Both CC and LR are able to reconstruct source and ghost peaks in the PCFOV. This section studies the LR imaging capability in this part of the FOV.

Two hundred LR iterations are a good choice if the source flux is at least 20% the initial Poisson background. They are able to recover the 87% source real flux. To obtain a realiable flux estimate for fainter sources, more iterations have to be performed.

An interesting example is represented by the simulation of the field of one PC plus one FC source of 1 and 0.3 cts s^{-1} cm^{-2} flux, respectively, both superimposed on a 1.45 cts s^{-1} cm^{-2} Poisson background. Their fluxes are

70% and 21% the initial Poisson background.

Due to the location of the simulated sources, we expect in the FCFOV a peak in correspondence of the source position plus 8 ghosts and coding noise in the PCFOV. Instead, we expect that the PC source should give rise to a peak in correspondence of its position plus 5 ghost peaks, all in the FC-FOV. The PC source should cause a diffusion of coding noise also over the FCFOV, distributed along the axes passing the PC source itself.

Fig. 6.16 show the deconvolved FCFOV images obtained by the CC (left) and 200 LR iterations (right). At the bottom of Fig. 6.16, the FC source profiles are fitted with the Gaussian model of Eq. 6.7, where the fit coefficients a, b and σ give the flux, the position and the 1σ error from the position of the source peak, respectively. Tab. 6.14 reports the coefficients of the Gaussian fits with their 95% confidence bounds.
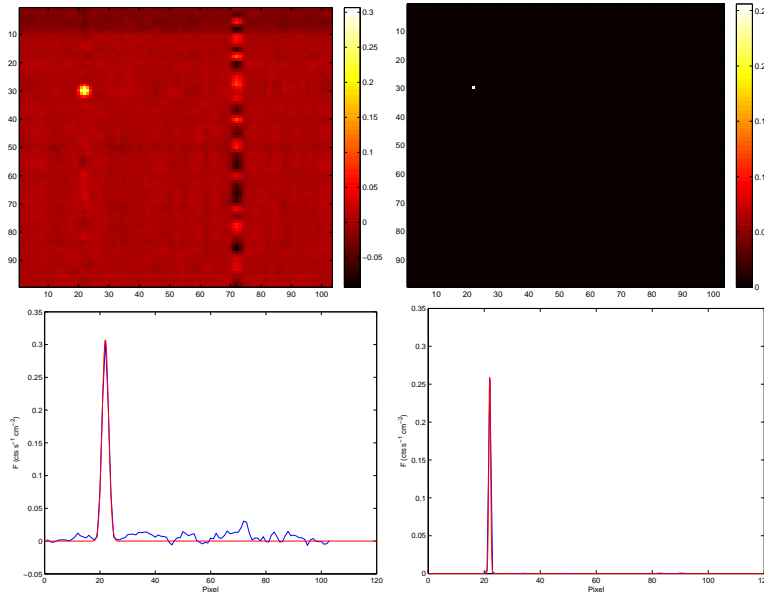

Figure 6.16 Top panel: deconvolved FCFOV images of the system of one PC (1 cts s^{-1} cm^{-2}) and one FC (0.30 cts s^{-1} cm^{-2}) source. Bottom panel: horizontal profiles of the FC source for both CC (left) and LR (right).

Algorithm	a (cts s^{-1} cm^{-2})	b (pxl)	σ (pxl)
CC	0.30 (0.29, 0.32)	21.98 (21.91, 22.04)	1.17 (1.11, 1.24)
LR	0.28 (2.79 10^{-1}, 2.80 10^{-1})	22 (21.98, 22.02)	0.30 (0.30, 0.31)

Table 6.14 The fit coefficients of the FC source profile in Fig. 6.16. Between round brackets there are their 95 % confidence bounds.

Both algorithms resolve the FC source, with deconvolved flux of 0.30 and 0.28 cts s^{-1} cm^{-2} for CC and LR, respectively. The source is correctly located in both cases. The standard deviation of the LR reconstruction is about one fourth than that obtained with the CC. The LR shows a great improvement in source location accuracy. Only ghosts along the vertical and horizontal axes crossing the FC source appear, with about 1% real FC source flux each.

The PC source is correctly reconstructed in both deconvolution methods. Fig. 6.17 shows the PC source profiles for both CC (left) and LR (right). Tab. 6.15 reports the coefficients of the Gaussian fits with their 95% confidence bounds.
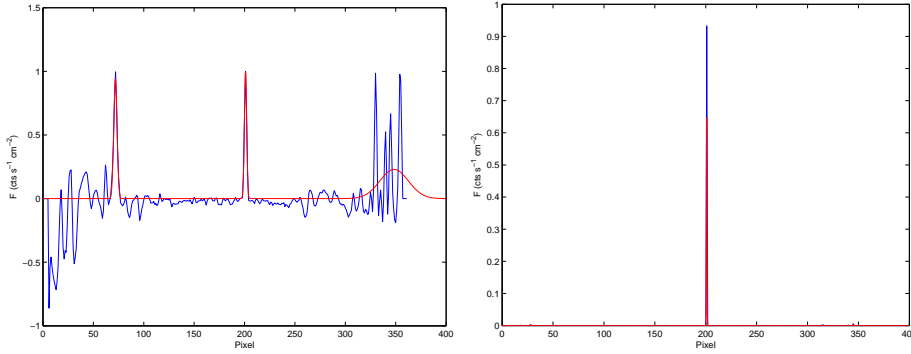

Figure 6.17 Total FOV profiles of the PC source for both CC (left) and LR (right). Here, the PC source has 1 cts s^{-1} cm^{-2} flux and the FC one 0.3 cts s^{-1} cm^{-2} flux.

Algorithm	a (cts s^{-1} cm^{-2})	b (pxl)	σ (pxl)
CC$_G$	0.95 (0.70, 1.20)	71.9 (71.4, 72.41)	1.64 (1.14, 2.14)
CC$_S$	1.00 (0.70, 1.31)	201 (200.6, 201.4)	1.13 (0.73, 1.52)
CC$_G$	0.23 (0.14, 0.32)	348.4 (339.3, 357.5)	14.06 (4.38, 23.74)
LR$_S$	94.42 10^{-2} (94.38 10^{-2}, 94.45 10^{-2})	201 (200.9, 201.1)	0.23 (0.20, 0.26)

Table 6.15 The fit coefficients of the profiles in Fig. 6.17. CC$_G$, CC$_S$, LR$_G$ and LR$_S$ refer to the fit parameters of ghost and source peaks for both CC and LR, respectively. Between round brackets there are their 95 % confidence bounds.

In this system, the ghosts of the PC source do not appear in the LR. The CC right hand side ghost is confused between the noisy boundary of the total FOV. The CC left hand ghost, instead, has the same strength as the deconvolved source.

The LR standard deviation of the PC source is almost 5 times bigger than

the CC one. LR is able to locate with the same accuracy both FC and PC
sources. The source location accuracy is independent on the source real flux
and on the fact that the source is in the FC or in the PC FOV.

The vertical feature in the CC decoded image (left hand side of Fig. 6.16)
is clearly related to the position of the PC source: it is the coding noise due
to it. In the CC this feature is a factor of 100 stronger than that in the LR
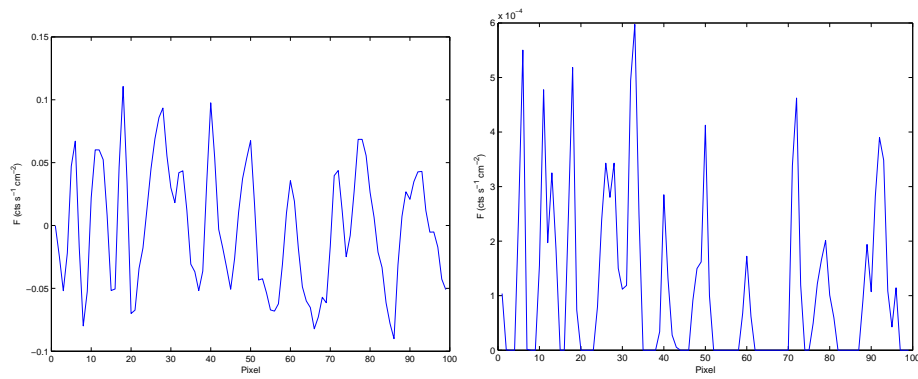deconvolved FCFOV image (see Fig. 6.18).

Figure 6.18 Profiles of the coding noise feature for both CC (left) and LR
(right). Here the PC source has 1 cts s^{-1} cm^{-2} flux.

The deconvolution of the field with only the 1 cts s^{-1} cm^{-2} PC source su-
perimposed on the usual Poisson background confirms that this feature is
the coding noise due to the PC source. The source is clearly and correctly
reconstructed with fit parameters consistent with those in Tab. 6.15 (see
rows CC$_S$ and LR$_S$).

As a further check, the source fluxes in the previous simulation are reversed
(i.e. a 1 cts s^{-1} cm^{-2} FC source and a 0.3 cts s^{-1} cm^{-2} PC one). Tab.
6.16 reports the coefficients of the Gaussian fit with their 95% confidence
bounds.

 For this field, the LR reconstructs only the ghost peaks of the PC source.
It is clear as both CC and LR correctly locate both source and ghost peaks.
In the LR, ghosts are fainter than the source (around 1% and 8% of the
LR deconvolved source flux for both left and right hand side ghost, respec-
tively). Two hundred LR iterations allow the reconstruction of 87% the real
PC source flux and 98% the real FC source flux.

Source	Algorithm	a	b	σ
FC	CC	1.01 (0.98, 1.03)	21.99 (21.96, 22.02)	1.15 (1.12, 1.18)
FC	LR	$98.03\ 10^{-2}$ ($98.01\ 10^{-2}$, $98.06\ 10^{-2}$)	22 (21.92, 22.08)	0.23 (0.22, 0.25)
PC	CC_G	0.28 (0.22, 0.35)	71.92 (71.48, 72.35)	1.68 (1.24, 2.16)
	CC_S	0.30 (0.22, 0.38)	201 (200.7, 201.3)	1.11 (0.78, 1.45)
	CC_G	0.30 (0.21, 0.39)	330.1 (329.8, 330.4)	0.90 (0.60, 1.2)
PC	LR_G	$3.13\ 10^{-3}$ ($2.69\ 10^{-3}$, $3.58\ 10^{-3}$)	72 (71.04, 72.96)	0.33 (0.01, 0.66)
	LR_S	0.262 (0.262, 0.263)	201 (200.8, 201.2)	0.26 (0.21, 0.30)
	LR_G	0.017 (0.016, 0.017)	330 (329.6, 330.4)	0.31 (0.20, 0.42)

Table 6.16 The fit coefficients of the system of one PC (0.3 cts s^{-1} cm^{-2}) and one FC (1 cts s^{-1} cm^{-2}) source for both CC and LR. CC_G, CC_S, LR_G and LR_S refer to the fit parameters of ghost and source peaks for both CC and LR, respectively. Between round brackets there are their 95 % confidence bounds.

6.7 Angular resolution and location accuracy

The theoretical angular resolution achievable was studied by simulating two strong point sources of the same flux (1 cts s^{-1} cm^{-2}) superimposed on the usual Poisson background and varying their relative separation. The LR theoretical angular resolution limit depends on the ISGRI pixel size. Fig. 6.19 shows CC (left) and LR (right) deconvolved FCFOV images when the two sources are separated by only one ISGRI pixel. At the bottom, the CC source profile is fitted with the Gaussian model of Eq.6.7, while the LR one with the sum of two Gaussians model defined as

$$a_1 \exp\left(-\frac{x-b_1}{2\sigma_1}\right)^2 + a_2 \exp\left(-\frac{x-b_2}{2\sigma_2}\right)^2. \qquad (6.11)$$

In Tab. 6.17 the coefficients of the Gaussian fits with their 95% confidence bounds for both CC and LR are reported.

Algorithm	a (cts s^{-1} cm^{-2})	b (pxl)	σ (pxl)
CC	1.44 (1.42, 1.47)	21 (20.97, 21.04)	1.61 (1.58, 1.65)
LR	1.03 ($-1.20\ 10^8$, $1.20\ 10^8$)	22.87 ($-1.78\ 10^6$, $1.78\ 10^6$)	0.28 ($-1.70\ 10^7$, $1.70\ 10^7$)
	0.98 ($-2.26\ 10^8$, $2.26\ 10^8$)	21.09 ($-1.18\ 10^7$, $1.18\ 10^7$)	0.26 ($-3.98\ 10^7$, $3.98\ 10^7$)

Table 6.17 The fit coefficients of the profiles in Fig. 6.19. Between round brackets there are their 95 % confidence bounds.

While the CC sees the two sources as a unique source of 1.44 cts s^{-1} cm^{-2} located in the middle of the two real positions, the LR can resolve them with an accuracy more than 5 times better (see the σ parameter in Tab. 6.17). The deconvolved fluxes of 1.03 and 0.98 cts s^{-1} cm^{-2} obtained with the LR are a good estimate of their real values. Each of the four ghosts along the
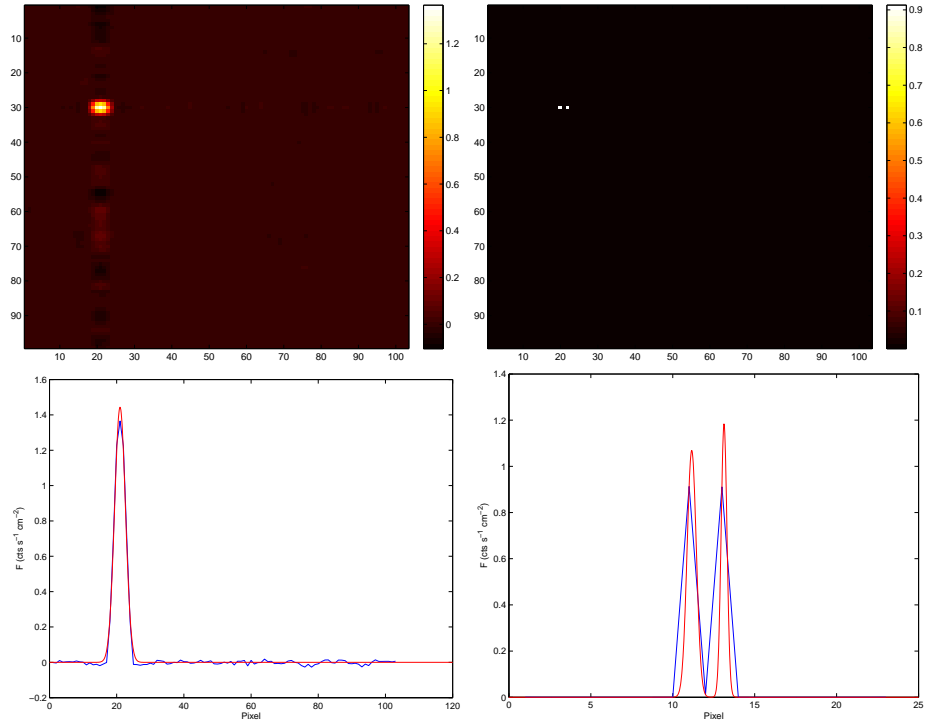
Figure 6.19 Deconvolved FCFOVs and sources profiles for both CC (left) and LR (right) in the situation where the two equal flux sources are separated by the theoretical LR resolution limit.

sources axes has streght less than 1% the source real flux. As expected, two hundred LR iterations to deconvolve this system are a good choice.

For two resolved sources at 1 ISGRI pixel distance as those in Fig. 6.19, the LR angular resolution is:

$$\Theta_{LR} = \arctan \frac{1 \ pxl \times 4.6 \ mm}{3200 \ mm} \approx 0.095^o \approx 5.73'. \tag{6.12}$$

The LR angular resolution does not depend neither on the number of iterations nor on the position of the source in the total FOV.

Chapter 7

IBIS/ISGRI data analysis

In this chapter the analysis of the IBIS/ISGRI data from Crab, Cygnus X-1 and the GRB IGR J00245+6251 was performed.

As said in Chapter 4, the IBIS 12' angular resolution is limited by the IBIS mask element size and the mask-detector distance. It does not allow sources in crowded fields as Galactic Centre to be resolved. This chapter will show the LR capability to deconvolve also Galactic Centre data.

For sake of completeness, the results obtained by our codes are compared with the state-of-art cross-correlation algorithm, decoding each SCW with the official software for INTEGRAL data analysis, OSA.

7.1 Data selection

In the previous chapter the better angular resolution and location accuracy obtained with the LR have been demonstrated. The limiting factor is the choice of the correct iteration number able to give confident reconstructed fluxes.

OSA performs the state-of-art balanced cross-correlation deconvolution. It considers all kinds of instrumental systematics in addition to the response function of the ISGRI detector. As said, our analysis was limited to consider only the geometrical features of photon propagation from the mask to the ISGRI detector, neglecting the ISGRI response function. The PSF used in our codes is different from that employed in OSA. For this reason, we compared the images restored with LR with those obtained with CC, considering the last as a reference. For sake of completeness, the comparison of the results was performed.

Each data file was singularly analysed in the 3-5000 keV energy band with

all three deconvolution algorithms. The OSA decoded total FOV images have size of 400×400 pxl and are in units of cts s^{-1} renormalized to the FC-FOV. The CC and LR codes, instead, reconstruct 361×365 pxl total FOV images in units of cts s^{-1} cm^{-2}.

Four sets of real data were chosen from the INTEGRAL archive: a set corresponding to a GRB, one set around the Crab, another around Cygnus X-1 (Cyg X-1) and, finally, another in the Galactic Centre. The ISDC identification numbers are given in Tab. 7.1.

SCW_ID	Region/Object	RA_X	DEC_X	Start Date
ID 026600780010	GRB	00 37 07.32	+65 41 32.5	12/2004
ID 010300030010	Crab	05 33 56.96	+21 59 29.1	08/2003
ID 063000360010	Cygnus X-1	20 22 21.77	+35 34 22.8	12/2007
ID 011500150010	Galactic	17 46 17.18	-28 59 58.8	09/2003

Table 7.1 The science windows selected for the real data analysis.

In the following of this chapter, the images of these SCWs deconvolved with CC and 200 LR iterations will be compared. The real data analysis confirms the results shown in the previous chapter. For strong sources as IGR J00245+6251, the Crab and Cyg X-1, 200 LR iterations are able to guarantee both better angular resolution and good flux estimation. However, for fainter sources, as those in the Galactic Centre SCW, more iterations must be performed to reconstruct their real flux. In all cases, both source and ghost peaks will be fitted with the Gaussian model of Eq. 6.7, where a, b and σ parameters give information about the reconstructed flux, the location and the accuracy in the location of the peak, respectively.

7.2 Data corresponding to GRB IGR J00245+6251

A GRB is one of the brightest sources in the sky and also occurs in a short timescale, so it should be one of the easiest sources to detect in a high X and γ ray background sky. The GRB IGR J00245+6251 was discovered with the INTEGRAL satellite in 2007 [7].

As can be seen in the deconvolved FCFOV images (Fig. 7.1), the detected source is spread over more than one pixels (i.e. 4×4 pxl in CC and 2×1 pxl in LR). The profiles along both horizontal and vertical axes crossing the maximum pixel of IGR J00245+6251 are analysed.

The OSA catalog reports the existence of two sources in this sky region: IGR J00245+6251 in the FCFOV and IGR J00291+5934 in the PCFOV. How-

ever, in the 3-5000 keV energy band only the stronger IGR J00245+6251 was detected with our codes.
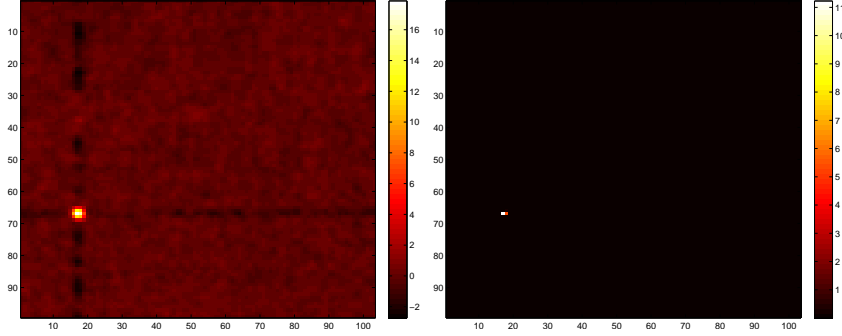

Figure 7.1 Deconvolved FCFOV images of the GRB SCW for both CC (left) and LR (right).

Fig. 7.2 shows the IGR J00245+6251 total FOV profiles. Source and ghost peaks are clearly visible. The fit coefficients with their 95% confidence bounds are reported in Tab. 7.2.

Algorithm	a (cts s^{-1} cm^{-2})	b (pxl)	σ (pxl)
Horizontal Profiles			
CC$_G$	6.20 (4.056, 8.35)	11.03 (7.53, 14.53)	7.94 (4.02, 11.85)
CC$_S$	19.15 (13.63, 24.67)	146.3 (146, 146.7)	1.12 (0.74, 1.48)
CC$_G$	18.92 (14.07, 23.76)	275.4 (275, 275.9)	1.44 (1.02, 1.87)
LR$_G$	1.48 (1.38, 1.59)	17 (7.35, 26.65)	0.22 (-1.92, 2.35)
LR$_S$	26.2 (-1.99, 54.4)	146.4 (146.3, 146.5)	0.32 (0.18, 0.47)
LR$_G$	2.11 (-20.17, 24.4)	275.6 (274.4, 276.8)	0.31 (-1.10, 1.73)
Vertical Profiles			
CC$_G$	18.51 (13.55, 23.46)	70.87 (70.43, 71.31)	1.41 (0.98, 1.85)
CC$_S$	18 (12.45, 23.56)	199.9 (199.5, 200.3)	1.12 (0.72, 1.53)
CC$_G$	18.64 (13.33, 23.94)	329 (328.6, 329.4)	1.24 (0.83, 1.64)
LR$_G$	1.62 (-7.71, 10.94)	70.61 (70.06, 71.15)	0.32 (0.48, 1.12)
LR$_S$	14.18 (-4.08, 32.44)	199.8 (199.4, 200.2)	0.25 (0.11, 0.40)
LR$_G$	2.07 (-0.57, 4.70)	329.3 (329.1, 329.5)	0.32 (0.12, 0.52)

Table 7.2 Fit coefficients of the profiles in Fig. 7.2. CC$_G$, CC$_S$, LR$_G$ and LR$_S$ refer to the fit parameters of ghost and source peaks for both CC and LR, respectively. Between round brackets there are their 95 % confidence bounds.

As can be seen from the b and σ parameters in Tab. 7.2, both CC and LR locate at the same position both source and ghosts, with more accuracy in LR than in CC (a factor of almost 5 in the horizontal profile and of almost 3 in the vertical one). The position of the left hand side ghost in the CC horizontal profile shows a greater uncertainty. This is due to its position at the noisy boundary of the total FOV.

The flux estimate (the a parameter in Tab. 7.2) is around 18 and 15 cts
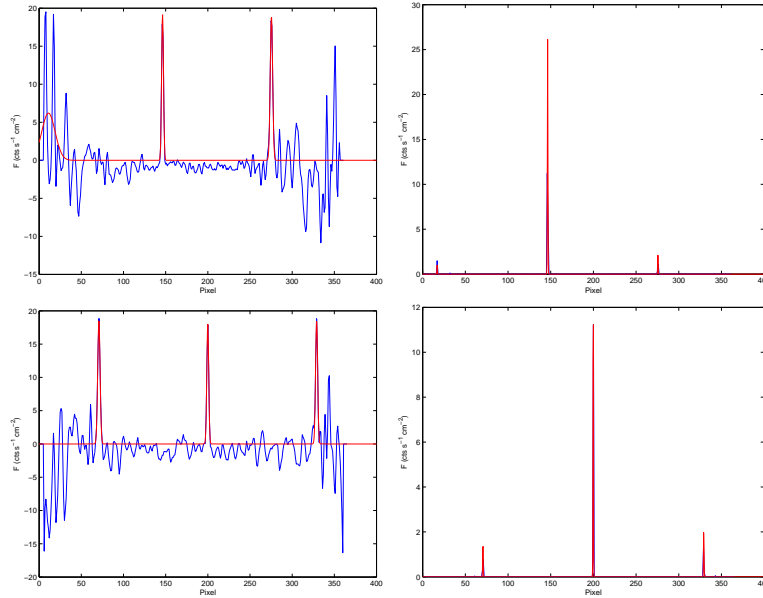
Figure 7.2 Total FOV profiles of IGR J00245+6251 for both CC (left) and LR (right). At the upper level there are horizontal profiles, while at the bottom level vertical profiles.

s^{-1} cm^{-2} for CC and LR, respectively. The overestimated source flux in the LR horizontal profile is due to IGR J00245+6251 spread over the two next pixels. The LR horizontal and vertical profile respectively overestimates and underestimates the CC reconstructed flux $a = 18$ cts s^{-1} cm^{-2} by about 7 cts s^{-1} cm^{-2}.

While in the CC ghosts have strength of the same order of magnitude as the CC deconvolved source (see the a parameter in Tab. 7.2), in the LR they are fainter (i.e. on average 7% and 13% the LR deconvolved source flux for both horizontal and vertical profiles, respectively).

Source	a_{OSA} (cts s^{-1})	b_{OSA} (pxl)	σ_{OSA} (pxl)
IGR J00245+6251	239.6 (228.3, 250.9)	198.3 (198.2, 198.4)	1.20 (1.13, 1.27)
IGR J00291+5934	10.76 (6.96, 14.56)	189.47 (189.00, 189.94)	1.15 (0.68, 1.63)

Table 7.3 Fit coefficients of the profiles in Fig. 7.4. Between round brackets there are their 95 % confidence bounds.

Figs. 7.3 and 7.4 show the deconvolved total FOV image and the horizontal profiles obtained with OSA. The fit of IGR J00291+5934 (right hand side of Fig. 7.4) converges only if a narrow abscissa interval around the source peak is selected. The fit coefficients of IGR J00245+6251 and IGR J00291+5934

with their 95% confidence bounds are reported in Tab. 7.3. Ghosts do not appear in all OSA total FOV images, since they are automatically removed.
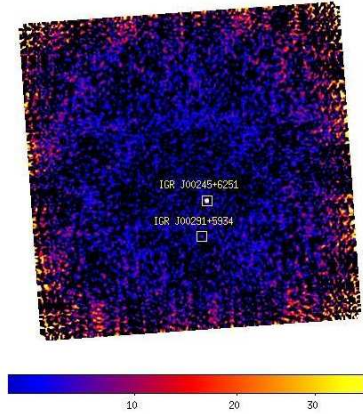

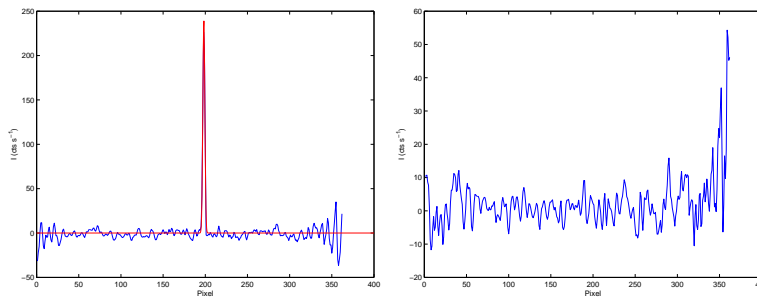Figure 7.3 OSA total FOV intensity map of the burst SCW.

Figure 7.4 OSA profiles of IGR J00245+6251 (left) and IGR J00291+5934 (right). I is in units of cts s^{-1}.

The position and the flux of IGR J00245+6251 obtained with OSA are different from those in Tab. 7.2. The different position is due to both the different size of the reconstructed total FOV images (i.e. 361×365 for CC and LR and 400×400 for OSA) and to their different orientation. The last issue will be clearer in Sect.7.7.

Flux estimates (i.e. the a parameter in Tabs. 7.2 and 7.3) are given in different units: cts s^{-1} for OSA and cts s^{-1} cm^{-2} for both CC and LR. The OSA deconvolved total FOV images must be corrected for the active area, i.e. the ISGRI area covered with only good pixels. Noisy pixels are around $n_B = 1\%$ the total number of ISGRI pixels N_{ISGRI} and one pixel area is A_p

$= 0.21$ cm^2. The active area is approximately

$$A_{act} = A_p \frac{(1 - n_B)\, N_{ISGRI}}{2} = 0.21\, \frac{(1 - 0.01)\, 16384}{2} \approx 1703.12\ cm^2,\ (7.1)$$

where the factor 2 takes into account the transparency of the mask. However, also employing this correction, the source fluxes are different. For example,

$$\frac{\frac{F_{OSA}}{A_{act}}}{F_{CC}} = \frac{\frac{239.6\ cts\ s^{-1}}{1703.12\ cm^2}}{19.15\ cts\ s^{-1}\ cm^{-2}} \approx 7.35\ 10^{-3}. \tag{7.2}$$

The ISGRI response function employed in OSA is the reason of this difference of a factor of almost 0.01. The CC overestimates the flux of IGR J00245+6251 by a factor of 100 with respect to OSA.

7.3   Data around Crab nebula.

The Crab Nebula is a supernova remnant with, at its centre, a very fast (about 30 Hz) rotating pulsar. Fig.7.5 shows reconstructed FCFOV images for both CC (left) and LR (right). The detected source is spread over 4×4 pxl in CC and 2×2 pxl in LR.
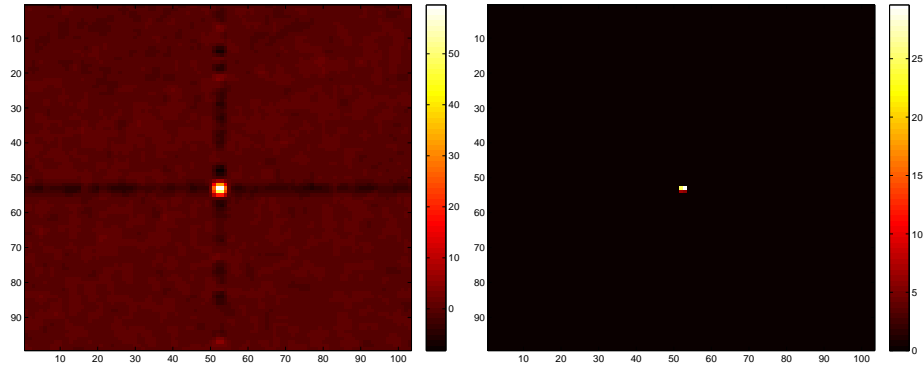

Figure 7.5 Deconvolved FCFOV images of the Crab SCW with both CC (left) and LR (right).

Fig. 7.6 shows the Crab horizontal and vertical profiles in the total FOV. They refer to the maximum pixel. The fit coefficients with their 95% confidence bounds are reported in Tab. 7.4.
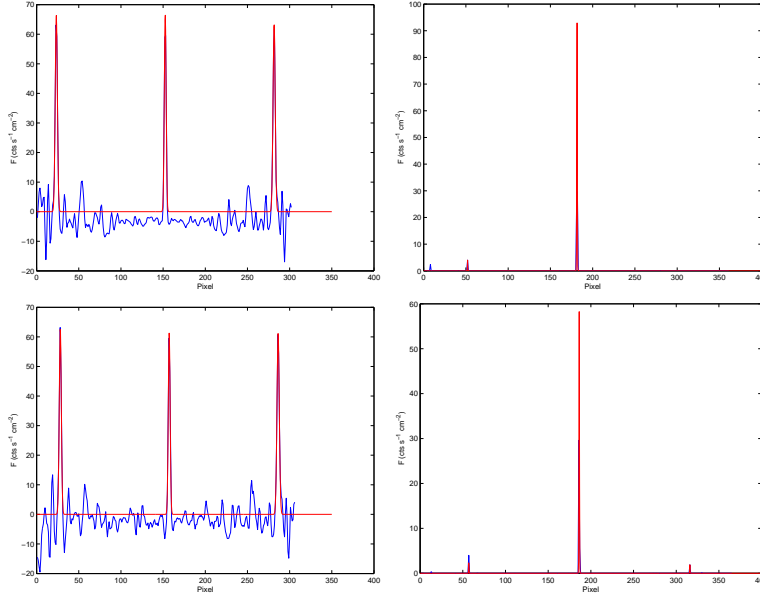
Figure 7.6 Total FOV profiles of the Crab for both CC (left) and LR (right). At the upper level are horizontal profiles, while at the bottom level the vertical profiles.

Algorithm	a (cts s^{-1} cm^{-2})	b (pxl)	σ (pxl)
Horizontal Profiles			
CC$_G$	66.4 (59.06, 73.74)	52.39 (52.22, 52.55)	1.29 (1.12, 1.45)
CC$_S$	66.62 (58.65, 74.6)	181.5 (181.4, 181.7)	1.09 (0.94, 1.24)
CC$_G$	63.43 (56.1, 70.76)	310.6 (310.5, 310.8)	1.29 (1.12, 1.46)
LR$_G$	4.01 (2.68, 5.33)	52 (-2415, 2519)	0.18 (-461.25, 461.60)
LR$_S$	96.12 (-1736, 1929)	181.5 (181.2, 181.8)	0.31 (-2.05, 2.68)
Vertical Profiles			
CC$_G$	62.75 (54.92, 70.58)	57.11 (56.94, 57.29)	1.22 (1.04, 1.39)
CC$_S$	61.5 (53.25, 69.74)	186.2 (186.1, 186.4)	1.10 (0.93, 1.27)
CC$_G$	61.24 (53.89, 68.59)	315.4 (315.2, 315.6)	1.38 (1.19, 1.57)
LR$_G$	3.99 (3.45, 4.53)	57 (-208.9, 322.9)	0.19 (-50.25, 50.63)
LR$_S$	59.01 (-58.19, 176.2)	186.4 (186.1, 186.6)	0.30 (0.06, 0.53)
LR$_G$	1.88 (0.27, 3.49)	316 (-535.9, 1168)	0.18 (-158.89, 159.31)

Table 7.4 Fit coefficients of the profiles in Fig. 7.6. CC$_G$, CC$_S$, LR$_G$ and LR$_S$ refer to the fit parameters of ghost and source peaks for both CC and LR, respectively. Between round brackets there are their 95 % confidence bounds.

Once again, the LR deconvolution shows better location precision than the CC one (i.e. a factor of 5 as can be seen by the σ parameter in Tab. 7.4). The CC source flux in the horizontal profile is 30 cts s^{-1} cm^{-2} fainter than the LR one, while source fluxes in the vertical profile are about of the same order of magnitude (i.e. around 60 cts s^{-1} cm^{-2}).
The flux difference between the two next pixel in the LR horizontal profile is more than 20 cts s^{-1} cm^{-2}. This is the reason for which the fit of the LR horizontal profile overestimates the source flux. The consistency of the flux evaluated with both CC and LR (i.e. 60 cts s^{-1} cm^{-2}) confirms as 200 LR iterations are a good choice in this case.
Again, the CC ghosts have about the same strength as the source peak (see the a parameter in Tab. 7.4). In the LR, ghosts are so faint that the detected ghost in the horizontal profile has flux 4% the reconstructed source, while those in the vertical profile are about 7% the real source flux, assumed to be 60 cts s^{-1} cm^{-2}.
Fig. 7.7 shows the Crab OSA deconvolved total FOV image and its horizontal profile. The fit coefficients with their 95% confidence bounds are reported in Tab. 7.5.
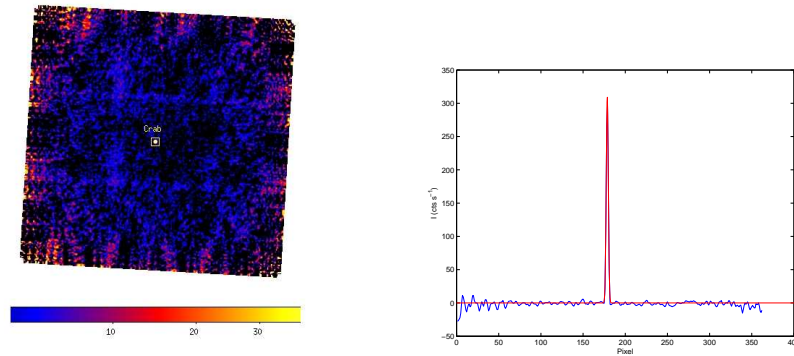

Figure 7.7 OSA total FOV intensity map (left) and Crab horizontal profile (right).

a_{OSA} (cts s^{-1})	b_{OSA} (pxl)	σ_{OSA} (pxl)
310.2 (302.6, 317.8)	178.7 (178.7, 178.7)	1.22 (1.19, 1.26)

Table 7.5 Fit coefficients of the Crab profile in Fig. 7.7. Between round brackets there are their 95 % confidence bounds.

About the different location of the source, the same considerations made in the GRB SCW analysis are valid. Being the Crab flux obtained with CC and LR equal to 60 cts s^{-1} cm^{-2}, the ratio of Eq.7.2 is 3.03 10^{-3}.

7.4 Data around Cygnus X-1

Cygnus X-1 is a BH in a HMXB system. Fig.7.8 shows reconstructed FCFOV images for both CC (left) and LR (right). The deconvolved image of Cyg X-1 is spread over 4×4 pxl in the CC and 2×2 pxl in the LR. Horizontal and vertical profiles are taken across the maximum flux pixel of the Cyg X-1 decoded image. The OSA catalog reports the existence of two sources in this sky region: Cyg X-1 in the FCFOV and Cyg X-3 in the PCFOV. In the 3-5000 keV energy band only the stronger Cyg X-1 was detected with our codes. The faint flux of Cyg X-3 prevents its detection.
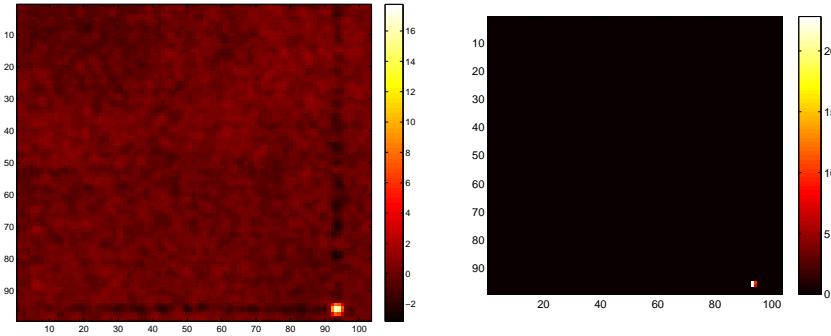

Figure 7.8 Deconvolved FCFOV images of Cyg X-1 SCW with both CC (left) and LR (right).

Fig. 7.9 shows Cyg X-1 horizontal profiles in the total FOV. The fit coefficients with their 95% confidence bounds are reported in Tab. 7.6.

Algorithm	a (cts s^{-1} cm^{-2})	b (pxl)	σ (pxl)
CC$_G$	18.37 (15, 21.74)	94.29 (94.01, 94.57)	1.32 (1.04, 1.60)
CC$_S$	18.47 (14.71, 22.23)	223.3 (223.1, 223.6)	1.07 (0.81, 1.31)
CC$_G$	18.29 (13.88, 22.69)	352.4 (352.2, 352.6)	0.83 (0.59, 1.07)
LR$_G$	2.03 (1.02, 3.03)	93.39 (93.34, 93.44)	0.32 (0.25, 0.40)
LR$_S$	14.86 (13.26, 16.46)	222.4 (222.4, 222.4)	0.32 (0.30, 0.33)

Table 7.6 Fit coefficients of the profiles in Fig. 7.9. CC$_G$, CC$_S$, LR$_G$ and LR$_S$ refer to the fit parameters of ghost and source peaks for both CC and LR, respectively. Between round brackets there are their 95 % confidence bounds.
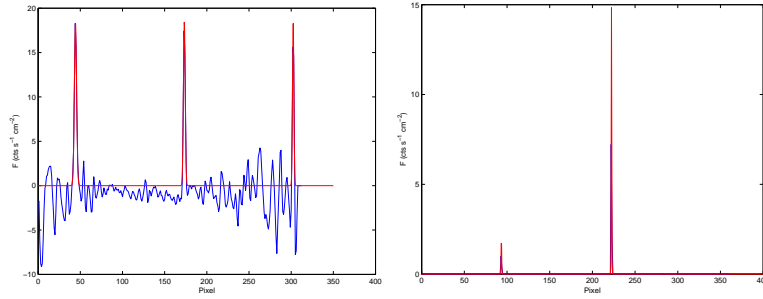
Figure 7.9 Total FOV horizontal profiles of Cyg X-1 for both CC (left) and LR (right).

Both algorithms correctly locate source and ghost peaks, but the LR with three times better accuracy (see the σ parameter in Tab. 7.6). The LR Cyg X-1 flux is about 3 cts s^{-1} cm^{-2} fainter than that obtained by CC (see the a parameter in Tab. 7.6).

While the CC ghosts show the usual behaviour, only the left hand side LR false peak is detected, with strength 14% the LR deconvolved Cyg X-1 flux. Again, the 200 LR iterations performed are a good choice. The faint ghost in the LR total FOV confirms the interconnection between the iteration number, the reconstructed source flux and the ghost peaks reconstruction. Fig. 7.10 shows the Cyg X-1 vertical profiles in total FOV, whose coefficients with their 95% confidence bounds are reported in Tab. 7.7.
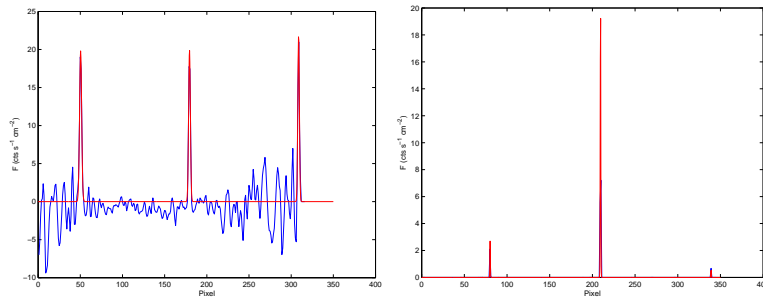

Figure 7.10 Total FOV vertical profiles of Cyg X-1 for both CC (left) and LR (right).

The LR right hand side ghost is visible, with flux only 3% the deconvolved source flux, while the left hand one has flux 13% the deconvolved source one. Cyg X-1 flux obtained with both deconvolution methods are consistent at about 20 cts s^{-1} cm^{-2} (see a values in Tab. 7.7).

Algorithm	a (cts s^{-1} cm^{-2})	b (pxl)	σ (pxl)
CC$_G$	19.82 (16.12, 23.52)	100.38 (100.11, 100.65)	1.24 (0.97, 1.51)
CC$_S$	19.91 (15.87, 23.94)	229.5 (229.2, 229.7)	1.05 (0.81, 1.29)
CC$_G$	21.87 (17.57, 26.18)	358.8 (358.6, 359)	0.91 (0.70, 1.12)
LR$_G$	2.73 (0.80, 4.65)	100.19 (99.99, 100.39)	0.27 (0.18, 0.35)
LR$_S$	20.63 (17.27, 23.99)	229.5 (229.5, 229.5)	0.32 (0.30, 0.35)
LR$_G$	0.67 (0.67, 0.68)	359 (357.3, 360.7)	0.22 (-0.14, 0.59)

Table 7.7 Fit coefficients of the profiles in Fig. 7.10. CC$_G$, CC$_S$, LR$_G$ and LR$_S$ refer to the fit parameters of ghost and source peaks for both CC and LR, respectively. Between round brackets there are their 95 % confidence bounds.

Fig. 7.11 shows the OSA deconvolved total FOV image. OSA detects two sources, Cyg X-1 and Cyg X-3, the first brighter than the second. Fig. 7.12 shows the Cyg X-1 (left) and Cyg X-3 (right) horizontal profiles. The fit coefficients with their 95% confidence bounds are reported in Tab. 7.8. For Cyg X-1, the ratio between the OSA and CC reconstructed flux (see Eq.7.2) is 7.26 10^{-3}.
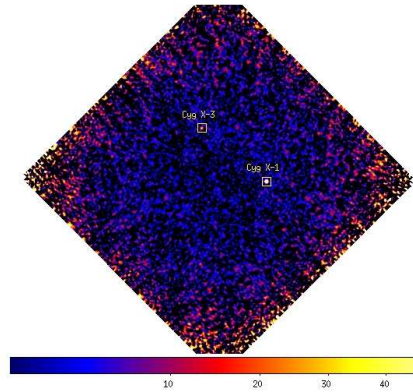
Figure 7.11 OSA total FOV intensity map of the Cyg X-1 SCW.

	a$_{OSA}$ (cts s^{-1})	b$_{OSA}$ (pxl)	σ_{OSA} (pxl)
Cyg X-1	247.2 (223.2, 271.1)	311.4 (311.2, 311.5)	1.26 (1.12, 1.40)
Cyg X-3	38.53 (27.48, 49.57)	169.1 (168.8, 169.5)	1.18 (0.78, 1.57)

Table 7.8 Fit coefficients of the profiles in Fig. 7.12. Between round brackets there are their 95 % confidence bounds.

Figure 7.12 OSA Cyg X-1 (left) and Cyg X-3 (right) profiles. I is in units of cts s^{-1}.

7.5   Data in the Galactic Centre.

In regions where the source density is high such as in the Galactic Centre, the IBIS/INTEGRAL 12' angular resolution does not always allow the resolution of nearby sources.

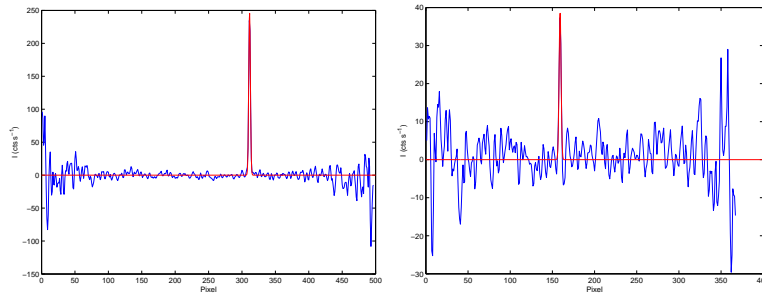Since in the previous chapter a better resolution than that of IBIS was found, the analysis of this Galactic Centre SCW would be a first look into the possible application of LR to INTEGRAL surveys.
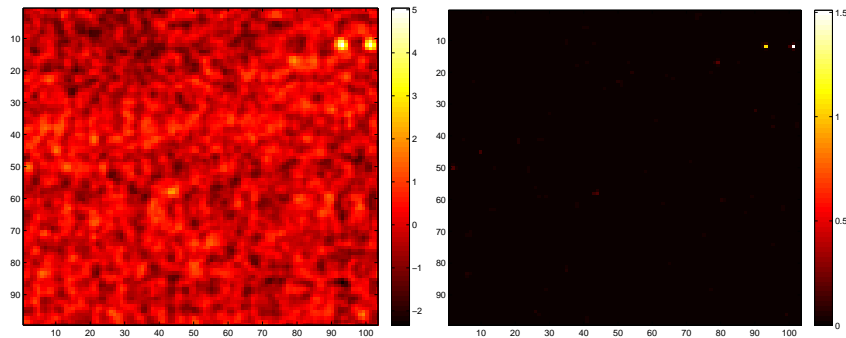
Figure 7.13 Deconvolved FCFOV images of the Galactic Centre SCW for both CC (left) and LR (right).

Fig. 7.13 shows deconvolved FCFOV images for both CC (left) and LR (right). More than one peak is detected. It must be checked if these are real sources or fluctuations before proceeding with the source identification. From the cross-check with the OSA total FOV and the user catalog, the identification of the real sources is possible. To do this, it is useful to employ a labelled version of the LR FCFOV (the upper panel in Fig. 7.14).
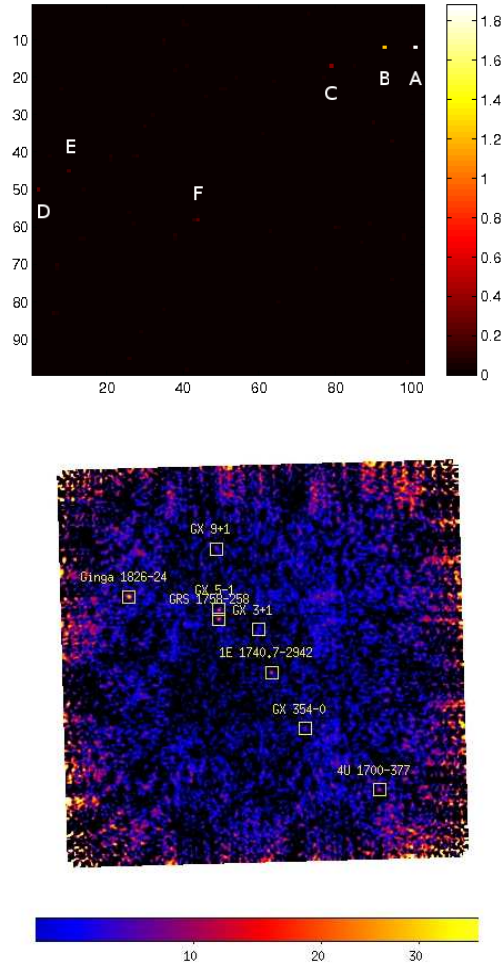
Figure 7.14 Labelled version of the LR deconvolved FCFOV image of Fig. 7.13 (up) and OSA total FOV intensity map (bottom).

Since the deconvolved sources cover only one pixel, only horizontal profiles are considered in this section.

Sources A, B and D are located at the boundary of the FCFOV. The right hand side ghosts of sources A and B and the left hand one of source D will be at the noisy boundaries of the total FOV. As said, this region is affected by greater uncertainty and, usually, it is prevented form the source searching. The ghost location in this region could be less accurate.

The LR non-linearity does not allow a standardized analysis of ghost peaks behaviour. The LR deconvolution should be stopped at the iteration num-

ber where the sources are clearly visible and ghosts are just detected. How
to do this exactly is under examination and may differ from field to field.
As will be seen in Sect.7.7, CC and LR deconvolved images have a different
orientation respect to the OSA one. To simplify the source identification, a
90° clockwise rotation of the OSA image (see Fig. 7.15) is performed. From
the relative location of the sources, the correspondence between the LR and
the OSA deconvolutions can be univocally found. Tab. 7.9 lists the position
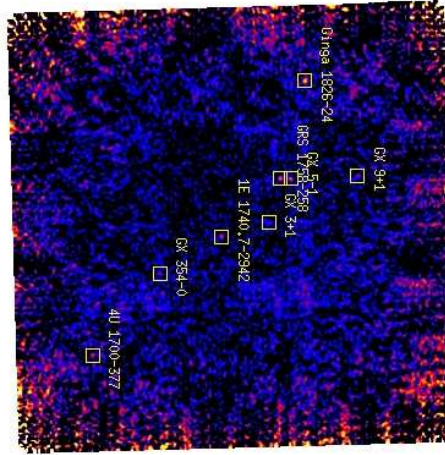and the flux of the sources in the Galactic Centre SCW taken from the OSA
catalog.

Figure 7.15 OSA 90° clockwise rotated intensity map of the Galactic Centre
SCW.

Name	R.A. (J2000)	Dec. (J2000)	$F_{3-10keV}$	$F_{10-30keV}$	$F_{20-60keV}$	$F_{60-200kev}$
Ginga 1826-24	18 29 28.2	-23 47 49	$1.19\ 10^{-9}$	$2.86\ 10^{-9}$	$2.05\ 10^{-9}$	$9.66\ 10^{-10}$
GRS 1758-258	18 01 12.7	-25 44 26	$1.19\ 10^{-9}$	$2.86\ 10^{-9}$	$2.05\ 10^{-9}$	$9.66\ 10^{-10}$
GX 5-1	18 01 08.2	-25 04 45	$2.29\ 10^{-8}$	$1.44\ 10^{-8}$	$4.53\ 10^{-9}$	$4.22\ 10^{-10}$
GX 9+1	18 01 32.3	-20 31 44	$5.37\ 10^{-9}$	$2.84\ 10^{-9}$	$8.77\ 10^{-10}$	$1.19\ 10^{-10}$
GX 3+1	17 47 56.0	-26 33 49	$6.67\ 10^{-9}$	$3.65\ 10^{-9}$	$1.13\ 10^{-9}$	$1.53\ 10^{-10}$
1E 1740.7-2942	17 43 54.83	-29 44 42.6	$3.09\ 10^{-10}$	$9.56\ 10^{-10}$	$7.19\ 10^{-10}$	$6.22\ 10^{-10}$
GX 354-0	17 31 57.4	-33 50 05	$9.48\ 10^{-9}$	$5.42\ 10^{-9}$	$1.68\ 10^{-9}$	$2.28\ 10^{-10}$
4U 1700-377	17 03 56.77	-37 50 38.9	$2.04\ 10^{-9}$	$2.37\ 10^{-9}$	$8.31\ 10^{-10}$	$1.50\ 10^{-11}$

Table 7.9 Properties taken from the OSA catalog for the sources in the
Galactic Centre SCW. *F* are the energy fluxes in the corresponding energy
bands, in units of cts s^{-1}. For further details, see [78].

7.5.1 OSA sources profiles

To proceed with source identification, the profiles of the sources detected with OSA are needed. While the fits in Fig. 7.17 converge, those in Fig. 7.16 do it if only a narrow selection around each peak is chosen. 4U 1700-377 is at the noisy boundary of the total FOV.

From the fit profiles obtained with the limited selection around the source peaks (Fig. 7.16) it results that:

- 4U 1700-377 location is at pixel 283±1.19 in Fig. 7.16 and its intensity is 17.11 (11.21, 23) cts s^{-1}.

- GX 3+1 location is at pixel 179±1.30 in Fig. 7.16 and its intensity is 6.24 (2.39, 10.1) cts s^{-1}.

- GX 9+1 location is at pixel 143±1.15 in Fig. 7.16 and its intensity is 9.97 (5.24, 14.71) cts s^{-1}.

- GX 354-0 location is at pixel 218±1.33 in Fig. 7.16 and its intensity is 9.89 (5.97, 13.82) cts s^{-1}.
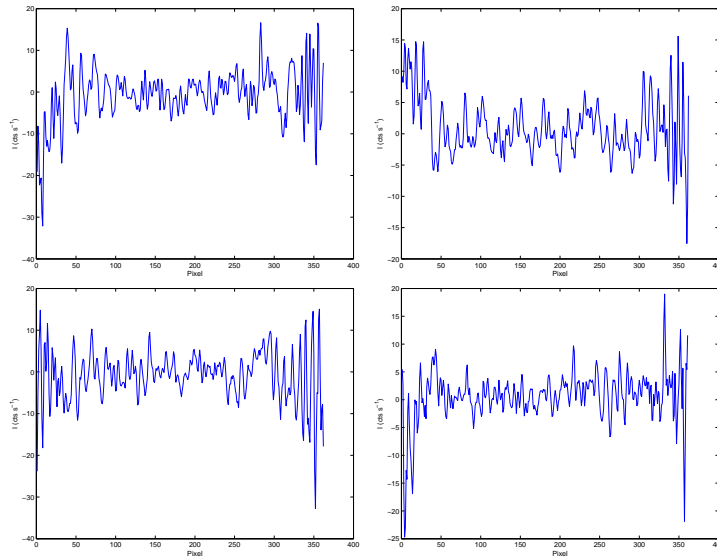
Figure 7.16 OSA profiles of the sources 4U 1700-377 (up-left), GX 3+1 (up-right), GX 9+1 (bottom-left) and GX 354-0 (bottom-right). I is in units of cts s^{-1}.

The coefficients of the fits in Fig. 7.17 with their 95% confidence bounds are reported in Tab. 7.10.

Name	a_{OSA} (cts s^{-1})	b_{OSA} (pxl)	σ_{OSA} (pxl)
Ginga 1826-24	34.75 (26.31, 43.18)	62.74 (62.29, 63.19)	1.06 (1.15, 2.06)
GX 5-1	24.43 (20.77, 28.09)	178.95 (178.74, 179.16)	1.22 (1.01, 1.43)
GRS 1758-258	24.84 (21.18, 28.50)	187.2 (187, 187.4)	1.22 (1.02, 1.43)
1E 1740.7-2942	18.31 (8.88, 27.74)	189.1 (188.3, 189.8)	1.30 (0.52, 2.07)

Table 7.10 Fit coefficients for the Galactic Centre sources in Fig. 7.17. Between round brackets there are their 95 % confidence bounds.
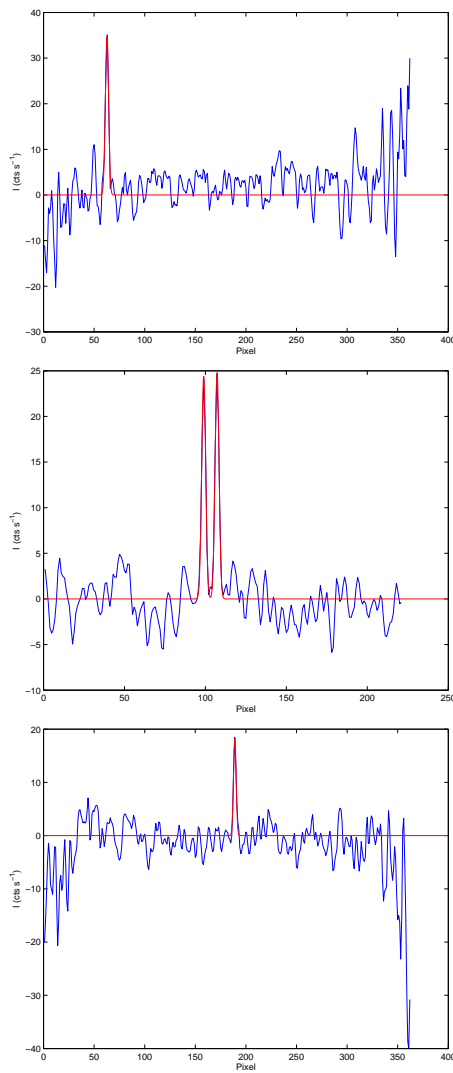
Figure 7.17 OSA profiles of the sources Ginga 1826-24 (first panel), GRS 1758-258 and GX 5-1 (second panel), 1E 1740.7-2942 (third panel). I is in units of cts s^{-1}.

7.5.2 CC and LR sources profiles

In this section, the profiles of the sources in Fig. 7.14 obtained by CC and LR deconvolutions are analysed.

Sources A and B

Fig. 7.18 shows the total FOV profiles of sources A and B for both CC (left) and LR (right). To guarantee the convergence, the CC fit is performed over a narrow interval around each peak pair. The fit coefficients with their 95% confidence bounds are reported in Tab. 7.11.
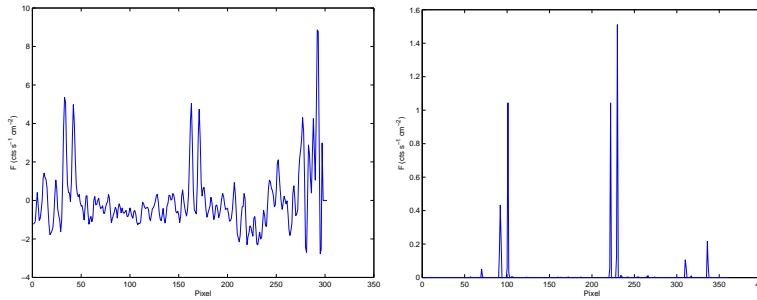

Figure 7.18 Profiles of the sources A and B in total FOV for both CC (left) and LR (right).

Algorithm	a (cts s^{-1} cm^{-2})	b (pxl)	σ (pxl)
Source A			
CC$_G$	4.94 (4.16, 5.72)	101.26 (101.01, 101.50)	1.32 (1.08, 1.56)
CC$_S$	4.85 (3.86, 5.83)	230.0 (229.75, 230.25)	1.07 (0.82, 1.32)
LR$_G$	1.05 (1.04, 1.06)	101 (100.9, 101)	0.40 (0.39, 0.40)
LR$_S$	2.43 (-7.53, 12.39)	229.7 (229, 230.5)	0.30 (-0.21, 0.81)
Source B			
CC$_G$	5.77 (4.98, 6.55)	92.35 (92.15, 92.56)	1.30 (1.09, 1.50)
CC$_S$	5.20 (4.25, 6.15)	221.7 (221.46, 221.95)	1.56 (0.91, 1.40)
LR$_G$	0.44 (0.43, 0.44)	92.09 (92.07, 92.1)	0.75 (0.73, 0.76)
LR$_S$	1.58 (-9.09, 12.24)	221.7 (220.4, 223.1)	0.28 (-0.54, 1.11)

Table 7.11 Fit coefficients of the LR profiles in Fig. 7.18. CC$_G$, CC$_S$, LR$_G$ and LR$_S$ refer to the fit parameters of ghost and source peaks for both CC and LR, respectively. Between round brackets there are their 95 % confidence bounds.

The position of sources A and B are consistent in both our deconvolution codes, with almost three times better accuracy in the LR (see the b and σ parameters in Tab. 7.11). The LR deconvolved flux underestimates that obtained with the CC (see the a parameter in Tab. 7.11).

The CC right hand side ghosts are not reconstructed due to their location

at the noisy boundary of the total FOV, while the CC left hand side ghosts are correctly located with stregth of the same order of magnitude as the CC deconvolved source flux.

Instead of the LR right hand side ghosts, two noisy peaks differently located with respect to the ghosts appear (see Fig. 7.18). These noisy peaks are reconstructed as if they are real sources instead of the ghosts. The LR left hand side ghosts are correctly located and have stregth of about one half of that of the LR respective deconvolved source.

Two hundred LR iterations are not enough for the correct evaluation of sources A and B flux. These are the strongest sources in the FCFOV of this SCW, so the number of iterations performed is not good in the case of the fainter sources.

Sources C and D

Fig.7.19 shows the total FOV profiles for both CC (left) and LR (right). The fit coefficients with their 95% confidence bounds are reported in Tab.7.12.
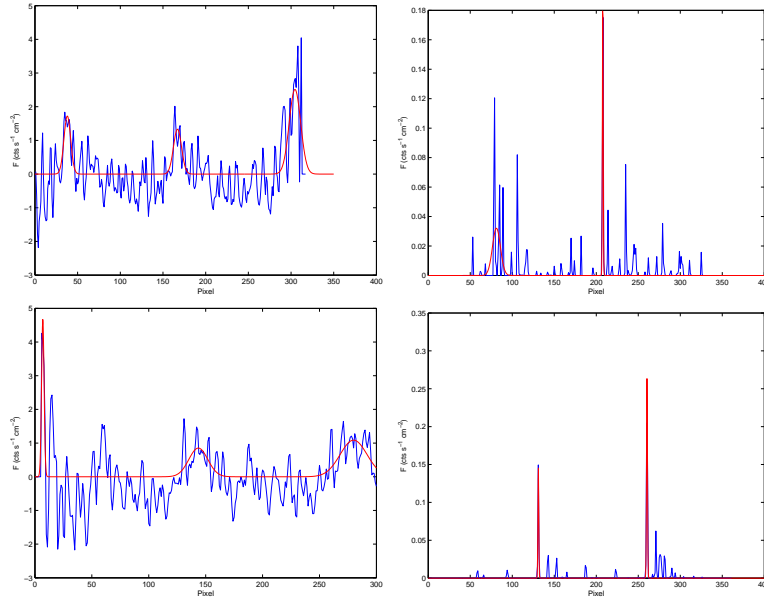
Figure 7.19 Profiles of the sources C (top panel) and D (bottom panel) in total FOV for both CC (left) and LR (right).

In CC, sources C and D are too faint to be resolved with great accuracy due to a more fluctuating background. Their positions, given by the b pa-

Algorithm	a (cts s^{-1} cm^{-2})	b (pxl)	σ (pxl)
Source C			
CC$_G$	1.72 (1.13, 2.32)	81.94 (80.36, 83.51)	3.93 (2.35, 5.50)
CC$_S$	1.33 (0.78, 1.88)	211 (208.8, 213.2)	4.71 (2.47, 6.94)
CC$_G$	2.51 (2.05, 2.97)	348.6 (347.2, 350)	6.72 (5.22, 8.24)
LR$_G$	0.03 (0.02, 0.04)	81.18 (79.67, 82.7)	4.74 (3.22, 6.25)
LR$_S$	0.19 (0.15, 0.24)	207.8 (207.6, 208)	0.49 (0.35, 0.63)
Source D			
CC$_G$	4.67 (3.43, 5.92)	6.95 (6.61, 7.29)	1.11 (0.77, 1.45)
CC$_S$	0.85 (0.39, 1.31)	143.6 (138.4, 148.7)	8.31 (3.17, 13.46)
CC$_G$	1.09 (0.70, 1.48)	280 (275, 285)	11.86 (6.50, 17.20)
LR$_S$	0.15 (0.14, 0.16)	131.1 (131, 131.2)	0.49 (0.44, 0.55)
LR$_G$	0.26 (0.24, 0.29)	260.4 (260.4, 260.4)	0.58 (0.51, 0.66)

Table 7.12 Fit coefficients of the LR profiles in Fig. 7.19. CC$_G$, CC$_S$, LR$_G$ and LR$_S$ refer to the fit parameters of ghost and source peaks for both CC and LR, respectively. Between round brackets there are their 95 % confidence bounds.

rameters in Tab. 7.12, are wrongly located and very uncertain (see the σ parameter in Tab. 7.12). This is also valid for the CC ghost peaks.

The LR correctly locates both sources with the same better 0.49 pxl accuracy. Only the left hand side ghost of source C is detected, with a strength 16% the LR deconvolved source C flux. The LR noisy peak on the right hand side of source D is not a ghost. It is a fluctuation that LR reconstructes as if it is a real source.

Sources E and F

Fig.7.20 shows the total FOV profiles for both CC (left) and LR (right). The fit coefficients with their 95% confidence bounds are reported in Tab.7.13.

Algorithm	a (cts s^{-1} cm^{-2})	b (pxl)	σ (pxl)
Source E			
CC$_G$	-0.35 (-0.73, 0.03)	22.85 (11.58, 34.12)	9.04 (-2.32, 20.41)
CC$_S$	0.59 (0.15, 1.03)	137.6 (131.7, 143.4)	6.73 (0.89, 12.57)
CC$_G$	0.91 (0.50, 1.32)	348.5 (344.1, 352.9)	8.19 (3.39, 13.00)
LR$_S$	0.15 (0.02, 0.27)	139.2 (138.8, 139.6)	0.37 (0.10, 0.64)
LR$_G$	0.12 (0.11, 0.12)	268.1 (268, 268.2)	0.53 (0.48, 0.58)
Source F			
CC$_G$	2.99 (2.13, 3.85)	41.34 (40.4, 42.28)	2.83 (1.89, 3.78)
CC$_S$	2.16 (1.00, 3.31)	172.3 (171.3, 173.2)	1.57 (0.60, 2.54)
CC$_G$	-0.68 (-1.10, -0.27)	282.2 (273.7, 290.6)	11.95 (3.51, 20.39)
LR$_G$	0.44 (0.43, 0.45)	43.15 (43.12, 43.18)	0.49 (0.47, 0.52)
LR$_S$	0.19 (0.16, 0.21)	172.6 (172.6, 172.6)	0.59 (0.50, 0.66)
LR$_G$	0.23 (0.21, 0.23)	302.1 (302.1, 302.1)	0.63 (0.60, 0.66)

Table 7.13 Fit coefficients of the profiles in Fig. 7.20. CC$_G$, CC$_S$, LR$_G$ and LR$_S$ refer to the fit parameters of ghost and source peaks for both CC and LR, respectively. Between round brackets there are their 95 % confidence bounds.

Sources E and F are correctly located in the deconvolved images obtained by both codes. However, the CC location of source E is very uncertain (see
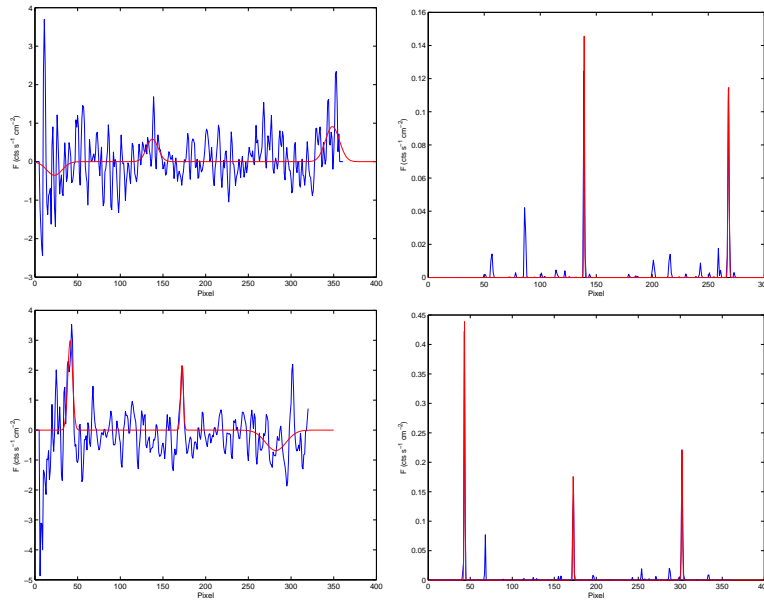
Figure 7.20 Profiles of the sources E (top panel) and F (bottom panel) in total FOV for both CC (left) and LR (right).

σ parameter in Tab. 7.13). The CC reconstructed flux of both sources does not agree with the estimates obtained from the LR (see a parameter in Tab. 7.13).

The CC ghost peaks are bad located and with bigger uncertainty (see the σ parameter in Tab. 7.13) with respect to the other sources in the Galactic Center SCW. Furthermore, the left hand side ghost of source E and that on the right hand side of source F have unphysical negative flux (see the a parameter in Tab. 7.13).

LR correctly locates both source and the ghost peaks with the usual greater accuracy. Both LR ghosts of source F are reconstructed with a strength bigger than the deconvolved source flux (see the a parameter in Tab. 7.13). Only the right hand side LR ghost of source E is reconstructed, with strength 80% the deconvolved source flux. The other peaks in the LR profiles are noisy spikes.

Tab. 7.14 summarizes the source position and the deconvolved flux of all the Galactic Centre SCW sources detected with both CC and LR. The location of all sources reconstructed with our codes are consistent, with more than three times greater accuracy in the LR. The flux estimates obtained with the CC do not agree with those obtained with two hundred LR iterations.

Source	P_{CC} (pxl)	F_{CC} (cts s^{-1} cm^{-2})	P_{LR} (pxl)	F_{LR} (cts s^{-1} cm^{-2})
A	230.0 ± 1.07	4.85	229.7 ± 0.30	2.43
B	221.7 ± 1.56	5.20	221.7 ± 0.28	1.58
C	211 ± 4.71	1.33	207.8 ± 0.49	0.19
D	143.6 ± 8.31	0.85	131.1 ± 0.49	0.15
E	137.6 ± 6.73	0.59	139.2 ± 0.37	0.15
F	172.2 ± 1.57	2.16	172.6 ± 0.59	0.19

Table 7.14 Summary of the position and the deconvolved flux of all the Galactic Centre SCW sources in Fig. 7.14 detected in both CC and LR restored images. P_{CC}, F_{CC}, P_{LR} and F_{LR} are the positions and the flux for both CC and LR, respectively.

7.5.3 Ghosts of the Galactic Centre sources

This section analyses the ghost total flux distribution of sources A, B and C in Fig. 7.14 as the iteration number increases until two hundred iterations. In real data analysis, the source flux and the ratio between reconstructed and real flux are not known.

Figs.7.21, 7.22 and 7.23 show the behaviour of the source and total ghost reconstructed fluxes of sources A, B and C, respectively. Both source and ghost distributions fit the sum of two Gaussians model of Eq.6.11, whose coefficients with their 95% confidence bounds are reported in Tabs.7.15 and 7.16.
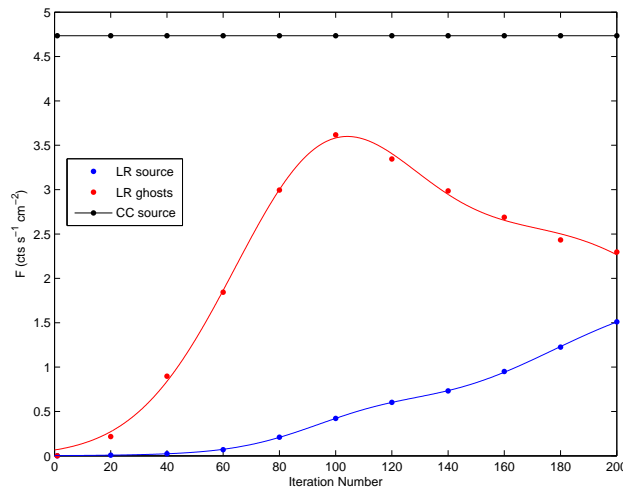

Figure 7.21 Total ghost (red) and source (blue) fluxes as a function of the iteration number in the case of the source A of Galactic Centre SCW. As a reference, in black, the deconvolved source flux obtained with CC is shown.

Figure 7.22 Total ghost (red) and source (blue) fluxes as a function of the iteration number in the case of the source B of Galactic Centre SCW. As a reference, in black, the deconvolved source flux obtained with CC is shown.

Source	a (cts s^{-1} cm^{-2})	b	σ
A	1.72 (1.62, 1.83)	233.5 (222.3, 244.6)	64.87 (56.52, 73.26)
	0.24 (0.18, 0.30)	111.9 (109.8, 114.1)	24.49 (20.52, 28.45)
B	1.04 (1.01, 1.07)	203.3 (196.7, 210)	59.32 (49.50, 69.14)
	0.18 (0.10, 0.26)	105.8 (101.9, 109.8)	23.49 (15.91, 31.07)
C	0.29 (-1.82, 2.40)	267.6 (-120.9, 656.1)	45.85 (-117.17, 208.88)
	0.08 (-0.11, 0.27)	176.5 (10.19, 342.8)	62.45 (13.68, 111.23)

Table 7.15 The fit coefficients of the reconstructed flux of the Galactic Centre sources A, B and C fluxes. Between round brackets there are their 95 % confidence bounds.

By the CC deconvolution, sources A and B have almost the same flux, while the source C is about one fourth of A (see Tabs.7.12 and 7.14). Even if the sources A and B are well resolved in both algorithms, their in line sky position could affect the estimate of both source and ghost fluxes.

For about 160 iterations, the reconstructed flux of source A is 1 cts s^{-1} cm^{-2} while that of source B is 0.8 cts s^{-1} cm^{-2}. Source B reconstructed flux is 1 cts s^{-1} cm^{-2} only after 180 iterations. Independently of the ordinate axes, the double Gaussians model has about the same shape for these two sources. What changes is the convergence velocity. However, the LR reconstructed fluxes underestimate their real values, as can be seen by the CC estimates (black curves).

If the CC deconvolved flux is considered as that of the real source, on average each of the 8 LR ghost has at most 5% the CC source flux. Ghost flux distribution shows a different behaviour after the maximum. While in

Figure 7.23 Total ghost (red) and source (blue) fluxes as a function of the iteration number in the case of the source C of Galactic Centre SCW. As a reference, in black, the deconvolved source flux obtained with CC is shown.
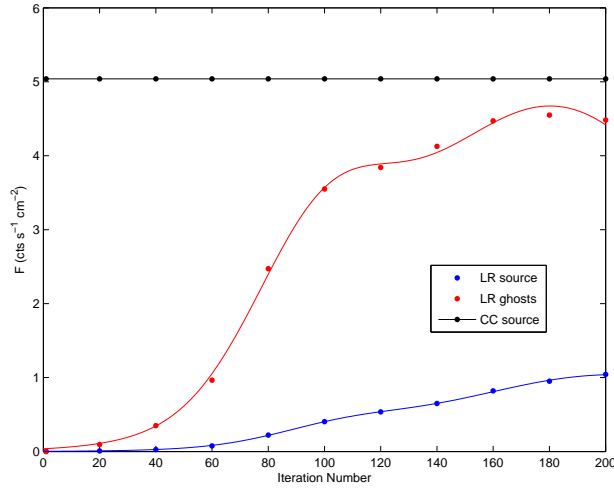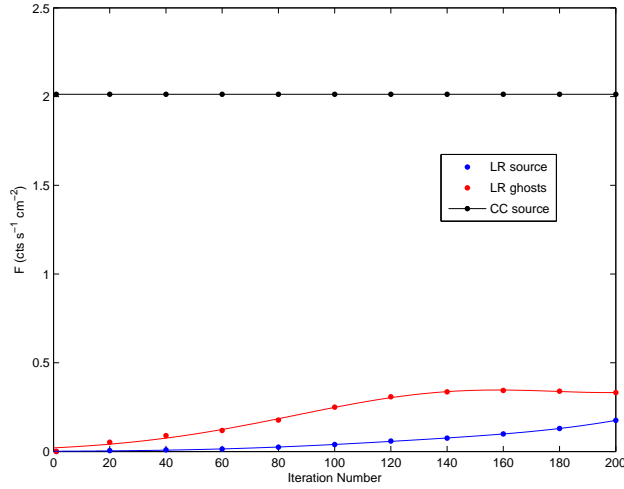
Ghost	a (cts s^{-1} cm^{-2})	b	σ
A	2.72 (-0.96, 6.40)	94.22 (81.43, 107)	33.28 (19.03, 47.53)
	2.40 (1.91, 2.90)	179.3 (128, 230.6)	56.72 (-25.83, 139.3)
B	1.80 (0.96, 2.65)	98.04 (93.76, 102.3)	24.10 (16.16, 32.05)
	4.67 (4.51, 4.83)	180.7 (172.8, 188.7)	58.00 (45.14, 70.85)
C	0.33 (-1.36, 2.02)	147.2 (-145.4, 439.8)	62.52 (-19.07, 144.11)
	6.49 (-6841, 6854)	455.9 (-6.85 10^4, 6.94 10^4)	88.88 (-1.28 10^4, 1,29 10^4)

Table 7.16 The fit coefficients of the ghost total flux for the Galactic Centre sources A, B and C. Between round brackets there are their 95 % confidence bounds.

source A it slowly decreases, in source B it continues to increase.

The source C flux continuously increases until a value of about 0.17 cts s^{-1} cm^{-2} for 200 iterations. Again, it underestimates the CC reconstructed flux. The ghost total flux increases until about 160 iterations when it reaches a saturation of 0.35 cts s^{-1} cm^{-2} until 200 iterations. If the CC deconvolved flux is considered as the real source one, on average the flux of each of the 8 LR ghosts is at most 1.3% the CC source one.

Increasing the iteration number until two thousand (see Fig. 7.24), the ghost total flux behaves in different way for the three sources. In this case, the total ghost distributions do not follow a simple fit model. Indeed, the lines in Fig. 7.24 are only the line connection between the found flux values.

As in the simulations, the study of ghost flux represents a huge problem at the moment. It requires more work to be able to remove these false peaks from the deconvolved images.
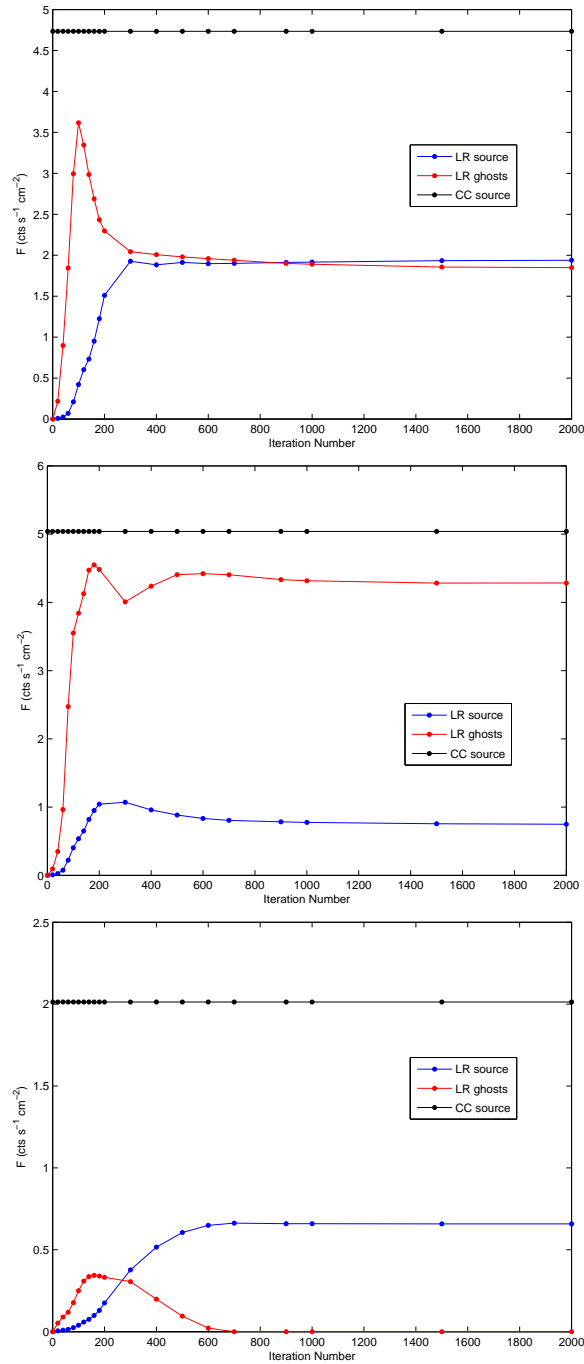
Figure 7.24 Total ghost (red) and source (blue) fluxes until 2000 iterations for source A (upper panel), source B (central panel) and source C (lower panel). As a reference, in black, the deconvolved source flux obtained with CC is shown.

7.6 Source identification

Given the consistent location of all sources in both CC and LR, their relative distance in the FOV is guaranteed. So, from the comparison of the sources in Figs. 7.14 and 7.15, the following identification results:

- sources A and B are GX 5-1 and GRS 1758-258, respectively;

- source F is 1E 1740.7-2942;

- sources C, D and E have not correspondence in the OSA image. More probably they are false peaks connected with the reconstruction of a background fluctuation.

Two hundred LR iterations are not enough to be able to reconstruct the real fluxes of all sources in the LR total FOV image of the Galactic Centre SCW.

The FC GX 3+1 and the PC GX 9+1 and GX 534-0 sources are too faint to be unequivocally localised in the LR decoded image. Ginga 1826-24, GX 9+1, GX 534-0 and 4U 1700-377 are in the PCFOV. 4U 1700-377 is at the boundary of the total FOV, so it is confused between noisy peaks.

However, Ginga 1826-24 is so strong that it is detected. Fig. 7.25 shows the Ginga 1826-24 total FOV profiles for both CC (left) and LR (right). The fit coefficients with their 95% confidence bounds are reported in Tab. 7.17.
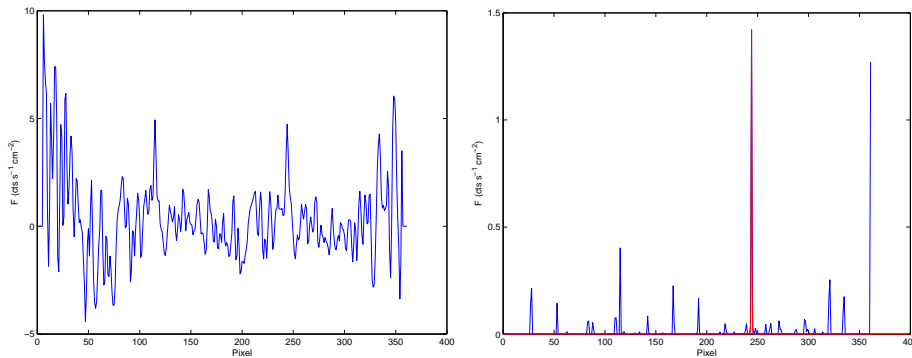
Figure 7.25 Total FOV profiles of Ginga 1826-24 for both CC (left) and LR (right).

As in the simulations, the LR is able to localize the PC sources with the same accuracy found for FC sources. Unfortunately, the source flux reconstruction remains a problem for both FC and PC sources.

Algorithm	a (cts s^{-1} cm^{-2})	b (pxl)	σ (pxl)
CC	4.25 (3.00, 5.49)	244.16 (243.6, 244.73)	1.66 (1.1, 2.23)
LR	1.43 (1.22, 1.63)	244 (243.7, 244.4)	0.38 (0.24, 0.52)

Table 7.17 Fit coefficients of the profiles in Fig. 7.25. Between round brackets there are their 95 % confidence bounds.

The ratio between OSA and CC estimated fluxes (Eq.7.2) is about 0.003 for GX 5-1 and GRS 1748-258 and 0.005 for 1E 1740.7-2942 and Ginga 1826-24. It is different also for sources in the same FOV. This confirms that the difference between the CC and the OSA reconstructed flux is mainly due to the different PSF used and to the fact that OSA considers also the response function of the ISGRI detector.

7.7   Reference System

To solve the problem of source identification in LR images, we need to employ catalogues of known sources. The easiest way to do it is to exploit the OSA reference catalog.

Figure 7.26 Spacecraft and instrument reference frame [79].

The INTEGRAL satellite has an X, Y, Z reference frame with the origin at the centre of the separation plane between spacecraft and launch adaptor. The X-axis is perpendicular to this spacecraft/launcher separation plane, 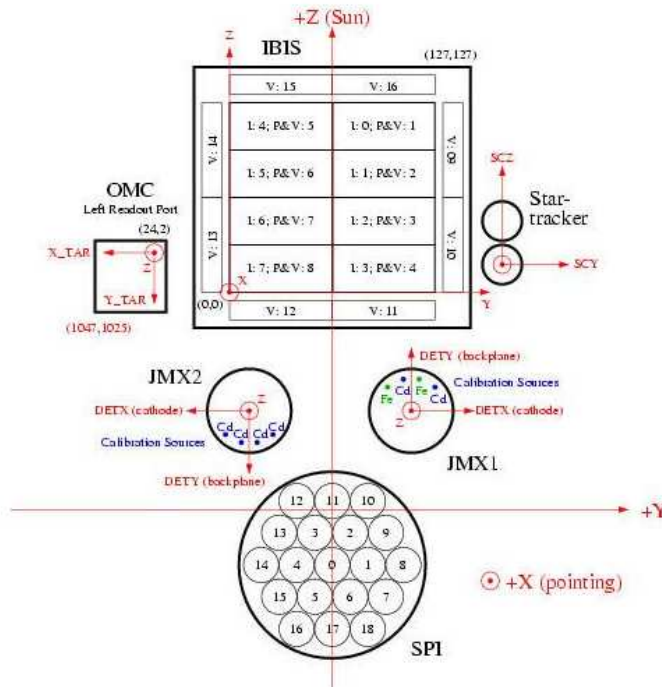pointing positively from the separation plane towards the spacecraft (i.e. the X-axis is the pointing direction). The Z-axis points positively to the Sun, that is illuminating the payload module on the IBIS side, while leaving SPI in the shadow. The Y-axis completes the coordinate system. Fig. 7.26 shows the spacecraft and instrument reference frame.

Our CC and LR reconstructions have a different orientation when compared with the OSA ones. A first problem is the different size of the deconvolved images. The CC and LR total FOV image size is 361×365 pxl, the OSA one is 400×400 pxl. So, before using OSA catalog, the CC and LR images have to zero-padded to the same dimension of the OSA one.

Furthermore, the size of the CC and LR total FOV image is odd, while the OSA one is even. An half of a pixel shift of the CC and LR images must be employed before zero-padding to the OSA image size.

We found that:

- CC images are 90° rotated with respect to the OSA ones (i.e. $X1 \rightarrow Y0$ and $Y1 \rightarrow X0$);

- LR images are 270° rotated with respect to the OSA ones (i.e. $X1 \rightarrow Y0$ and $Y1 \rightarrow -X0$).

In all previous analysis, for having a direct comparison between LR and CC deconvolved images, LR ones were 180° clockwise rotated yet. So, both CC and rotated LR images must be 90° clockwise rotated respect to the OSA.

Chapter 8

Conclusions and Future Developments

8.1 Conclusions

Astronomical imaging at energy greater than 20 keV is mainly achieved through modulation techniques. Currently, the coded mask technique is widely used with the true spatial intensity distribution reconstructed from the observational data by the cross-correlation (CC) method.

With this method and the current position sensitive detectors for hard-X ray astronomy, the hard-X ray sky cannot be imaged in high detail. This is a strong drawback in crowded fields as the Galactic Centre, where the cross-correlation is not able to resolve all the X ray sources in this region.

One possibility is to use instruments that employ the extra dimension of time modulation, as in the HXMT satellite. Another possibility to overcome this problem is to change the deconvolution method. In this thesis I have investigated this possibility.

Starting from the work by Y. Chen et al. [16], the objective of this thesis was the investigation of the real imaging capability of the Direct Demodulation (DD) method, proposed to deconvolve the HXMT time modulated data. The DD directly deconvolves incomplete and noisy data solving the inverse image formation equation. Since the Poisson statistics is a good description of the photon counts distribution in hard-X rays, the Lucy-Richardson (LR) code has been developed. It guarantees the non-negativity of the restored images.

Due to the general nature of the DD and the fact that HXMT has still not flown, the IBIS/INTEGRAL data and its PSF were used to test the

imaging capability of the LR code. The PSF used in our codes considers only the geometrical features of photon propagation from the IBIS mask to the ISGRI detector. The response function of the ISGRI detector has been neglected, even if, for sake of completeness, the real data images obtained by the CC and LR algorithms were compared with those obtained by the official software for IBIS/INTEGRAL data analysis. OSA considers all kinds of instrumental systematics in addition to the ISGRI response function.

To define the quality of the images restored with the two methods, I have evaluated the achievable angular resolution and the flux estimate. I have also studied the limit sensitivity of the LR method. The main results of this investigation are the following.

1. **Flux reconstruction**. The number of LR iterations performed is the main limiting factor to the goodness of the reconstructed flux. Two hundred LR iterations underestimate the real flux for sources fainter than 7% times the initial background radiation. For example, a number of iterations of 200 can reconstruct 60% of the real flux of a source with 7% times the initial background radiation, while preliminary results show that 2000 iterations are necessary to recover 93% of the real flux.

The fact that, to reconstruct the true flux, a large number of iterations is requested, implies high computer time. Thus acceleration techniques are desiderable.

The minimum source flux that can be reconstructed with CC, at 3σ significance level, is 0.3% times the input background level. Two hundred LR iterations can reconstruct only 8% of the source real flux and the found Signal-to-Noise Ratio (SNR) underestimates the sensitivity.

In principle, LR should be more sensitive than CC given the reconstructed background is less fluctuating (by a factor of 10) with respect to that obtained with CC. Unfortunately, the fact that the reconstructed source flux is biased (i.e. lower than the expected) decreases the method sensitivity.

Also the found SNR is a function of the number of iterations. Indeed, for example, two hundred LR iterations recover 98% of the real flux of a 70% times the initial background source, with found SNR around $(800 \pm 53)\,\sigma$, consinstent with the source sensitivity.

2. **Ghosts**. The choice of a deconvolution method affects the ghost peaks strength, while their location depends on the mask geometrical properties. With 200 iterations, a source of increasing flux (i.e. from 0.7% to

70% times the initial background radiation) exponentially has fainter total ghost flux.

The number of iterations performed strongly affects the total ghost flux. As the iteration number increases, the total ghost flux first increases and then slowly decreases toward the zero value. The maximum total ghost flux depends on the source intensity in the field and on the number of iterations. On average, each LR ghost is fainter than the corresponding CC ghost (that always has strength equal to the source deconvolved flux) but it does not follow a standard behaviour neither for sources in the same FOV nor for sources of similar flux, as can be seen from the analysis of ghost peaks of the Galactic Centre sources.

3. **Angular resolution**. The best advantage of the LR method is its better angular resolution than CC. For example, using two strong sources of the same flux, we find an angular resolution of about 6 vs. 12 arcmin found with CC. The accuracy in the peak location is at least 3 times better than that obtained in the CC.

Both better angular resolution and accuracy in the peak location are independent on the fact that the source is in the FC or in the PC FOV. The LR imaging capability in the PCFOV is equal to that obtained in the FCFOV.

4. **Analysis of real data**. The analysis of real IBIS/ISGRI data confirms the better angular resolution and location accuracy results found in the simulations. Two hundred LR performed are a good choice for the flux estimate of IGR J00245+6251, Crab and Cyg X-1. However, 200 iterations are not enough to well reconstruct the flux of the sources in the Galactic Centre.

8.2 Future developments

At this time, the simplest formulation of the optimization problem solved with the LR can be efficiently used to resolve and locate sources. The classical Maximum-Likelihood (ML) problem is ill-posed since it uses only information about the noise. It requires some kind of regularization. A smaller number of iterations can improve the image reconstruction quality and can control the noise amplification, but it does not solve the ill-posedness issue. The introduction of an objective function that gives further information about the unknown object should be added in the code. For example, Y.

Chen, T.P. Li and M. Wu [16] require that the expectation value of the noise is zero and the standard deviation of the data is one. In addition, the optimization problem should include the flux conservation constraint. This requires a code to be developed for the evaluation of the background in each field, both simulated and real.

The number of iterations is a crucial issue, given the connection between the iteration number and source reconstructed flux. The criterion to establish the best number of iterations requires more work.

Thanks to its angular resolution improvement and the better location capability, LR can be used for resolving sources in crowded sky regions as the Galactic Centre. However, due to the uncertain flux reconstruction, in the present version of the code, LR could be used in combination with another method that provides the flux estimate of the sources resolved with LR.
The convergence speed of the conventional LR method is very low. Zong-Jun Shen and Jian-Feng Zhou [72] developed a new procedure, called Accelerated DD Method (ADM), able to improve the angular resolution of coded-mask telescopes by DD and to save computational time. The angular resolution of the LR applied to the IBIS/INTEGRAL imager is limited by the ISGRI pixel size s_d. The decoding array was resampled at the detector's pixel size and the corresponding pixel size of the image is $\arctan(s_d/L) \approx 5$ arcmin, where L is the mask-detector distance. To achieve better angular resolution, smaller image pixels should be used preserving the shift-invariant property of the aperture. These authors show that dividing the data pixel into n sub-pixels the angular resolution can improve from 12 until to about 2 arcmin. Other acceleration techniques have also been proposed. For instance, M.K. Singh [74] proposed the introduction of an exponent in the correction ratio of the LR (see Eq. 5.2).

This thesis could be a help for a best exploitation of the current and future coded-mask systems instrumentation, as the Brazilian MIRAX satellite now under development, or in telescopes based on temporal modulation as the Chinese HXMT mission [54].

Appendix A

Coded mask system concepts

A.1 Cyclic difference sets

A cyclic difference set $\Delta(N, M, \lambda)$, characterized by the parameters N, M and λ, is a sequence of M residuals (integer number), modulus N, such that for any residual $\rho \neq 0 (\text{mod } N)$ the congruence $\delta_i - \delta_J \equiv \rho (\text{mod} N)$ admits exactly λ solution pairs (δ_i, δ_j) with δ_i and δ_j within Δ.

To each difference set it is possible to associate a binary sequence $\{\alpha_i\}$ of length N, wherein α_i takes the value 1 if i belongs to Δ and 0 otherwise. δ_i in turn can stand for the discretized mask pattern, assigning a transparent element to $\delta_i = 1$ and an opaque one to $\delta_i = 0$.

In order to achieve an optimum SNR, a difference between M and λ that is as large as possible is advantageous, where M determines the signal and λ the background level and its noise. The maximum difference is reached in Hadamard sets. The characteristic parameters take the form $N = 4t - 1$, $M = 2t - 1$, $\lambda = t - 1$ being t an integer. These may be classified by the value of N: if N is prime, the set is given by residuals, $(mod N)$, of the squares of the first $(N + 1)/2$ integers. Characteristic of Hadamard sets is that $M = (N - 1)/2$, i.e. for large N the mask pattern is about half open. Once the binary sequence has been generated, if its length N can be factorised into a product of two integers ($N = p \times q$), it is possible to build a two-dimensional array. For further details see [5].

A.2 The Signal-to-Noise Ratio

The theoretical SNR of a particular pixel is the ratio between the expected value of intensity in that pixel and a noise term, $SNR = S_{ik}/\sigma_{jk}$,

where the noise in pixel (j, k), σ_{jk}, will be derived in the remaining of this section.

The reconstruction technique correlates the data with a decoding array G, that is, except for a scaling factor, a replica of the aperture pattern. The only initial constraints on G, by construction, is that it is the correlational inverse of M, i.e. $M * G \equiv \delta$. If the peak intensity is normalized to the amount of open area in the aperture (or equivalently to $N = \sum_{ij} M_{ij}$, the number of transparent elements in the basic pattern), we have $M * G = N\delta$. The source is perfectly reconstructed with the exception of a background term. Indeed,

$$\widehat{S}_{ij} = NS_{ij} + (B * G)_{ij}. \tag{A.1}$$

The detector background is assumed uniform over the detector plane.

The definition of error in the computation of S is provided by the standard deviation in $\widehat{S}_{ij}$, given by

$$\sigma(\widehat{S}_{ij}) = \sqrt{\sigma^2(S_{ij}, \widehat{S}_{ij}) + \sum_{kl} \sigma^2(S_{kl}, \widehat{S}_{ij}) + \sigma^2(B, \widehat{S}_{ij})} \tag{A.2}$$

where $\sigma^2(S_{ij}, \widehat{S}_{ij})$, $\sigma^2(S_{kl}, \widehat{S}_{ij})$ and $\sigma^2(B, \widehat{S}_{ij})$ are the variances associated to the statistical variations of the flux in the direction (i, j) S_{ij}, that of the region around S_{ij} due to all the source elements within the FOV and that due to the unmodulated background respectively. S_{ij} will contribute to the variance of the flux of both source and background. For further details, see [26].

Now, assuming that measurements (source fluxes and background) obey Poisson statistics, the terms in Eq.A.2 are reduced to:

$$\sigma^2(S_{ij}, \widehat{S}_{ij}) = S_{ij} \sum_{kl} M_{kl} G_{kl}^2 \tag{A.3}$$

$$\sum_{kl} \sigma^2(S_{kl}, \widehat{S}_{ij}) = [(S * M) * G^2]_{ij} \tag{A.4}$$

$$\sigma^2(B, \widehat{S}_{ij}) = (B * G^2)_{ij} \tag{A.5}$$

where G^2 is a matrix obtained by squaring each G individual terms. This is exactly what one expects for the noise propagation with a linear operator. The first contribution of G is proportional to S_{ij} and independent on all other sources, while sources other than S_{ij} contribute to the variance of the second term, an inevitable consequence of the multiplexing process.

Furthermore, each term is weighted by the square of a decoding coefficient. If the reconstruction method leads to G_{ij}^2 with not all the same value, some S_{ij} will contribute more to the noise than others. Since in general one has not prior knowledge about S_{ij}, the best strategy to have all $(G_{ij})^2$ equal is imposing the G unimodularity.

URA and MURA Sensitivity

For the URAs and the MURAs, G is the aperture pattern itself (see [26]): its unimodularity ensures that all S_{ij} will contribute in the same manner to noise. Following Fenimore [26] and Gottesman [38] derivations, Eq.A.3-A.5 reduce to

$$\sigma^2(S_{ij}, \widehat{S}_{ij}) = NS_{ij} \qquad \text{(A.6)}$$

$$\sum_{kl} \sigma^2(S_{kl}, \widehat{S}_{ij}) = \left(\sum_{kl} S_{kl}\right)\left(\sum_{mn} M_{mn}\right)(G_{ij})^2 = N\sum_{kl} S_{kl} \qquad \text{(A.7)}$$

$$\sum_{kl} \sigma^2(B, \widehat{S}_{ij}) = \sum_{kl} B_{kl}. \qquad \text{(A.8)}$$

Eq.A.7 is a constant term for all (ij) elements resulting in a removable dc term. The optimum SNR is independent of source structure. It will be:

$$SNR_{ij} = \frac{NS_{ij}}{\sqrt{NS_{ij} + N\sum_{kl} S_{kl} + \sum_{mn} B_{mn}}}. \qquad \text{(A.9)}$$

$(C_S)_{ij} = NS_{ij}$ is simply the number of net source counts emanating from the (ij)th source element recorded by the detector, $N\sum_{kl} S_{kl}$ is the number of net counts detected from all sources and $C_B = \sum_{mn} B_{mn}$ is the total detector background counts. Thus Eq.A.9 can be rewritten as:

$$SNR_{ij} = \frac{(C_S)_{ij}}{\sqrt{(C_S)_{ij} + C_B}} \qquad \text{(A.10)}$$

Appendix B

The objective function

In this appendix a complete explanation of the objective function F proposed by Y.Chen, T.P.Li and M.Wu [16] is given. In chapter 5 it was defined as

$$F(f,n) =$$
$$\left[\left(\sum_{i=1}^{N}\frac{n_i^2}{d_i} - N\right)^2 + \rho\left(\sum_{i=1}^{N}n_i\right)^2\right] - \beta\sum_{i=1}^{M}\left(\ln(f_i - low_i) + \ln(up_i - f_i)\right)$$

The term between square brackets can also be written as

$$\left[N^2\left(\frac{1}{N}\sum_{i=1}^{N}\frac{n_i^2}{d_i} - 1\right)^2 + \rho N^2\left(\frac{1}{N}\sum_{i=1}^{N}n_i\right)^2\right]. \tag{B.1}$$

Let assume a Poisson distribution for the noise and the data. From statistics, the mean of the Poisson distribution is equal to its variance. The data can be rewritten as $d_i = \overline{f_i} + n_i$, where n_i is the noise associated to the source intensity $\overline{f_i} = Pf_i$.

The second term of Eq.B.1 is the expectation value of the noise and it is required to be zero, i.e.

$$E(n_i) = \frac{1}{N}\sum_{i=1}^{N}n_i = 0, \tag{B.2}$$

so the noise variance will be

$$\sigma_{n_i}^2 = \frac{1}{N}\sum_{i=1}^{N}(n_i - E(n_i))^2 = \frac{1}{N}\sum_{i=1}^{N}n_i^2. \tag{B.3}$$

The expectation value of the data is:

$$E(d_i) = E(f_i) + E(n_i) = \frac{1}{N} \sum_{i=1}^{N} f_i = \overline{f_i}, \tag{B.4}$$

while, from the Poisson distribution properties, the data variance is

$$\sigma_{d_i}^2 = d_i. \tag{B.5}$$

Let define χ^2 statistic. If $Z_1, \ldots, Z_k$ are independent normal standardized (i.e. with mean 0 and variance 1) r.v., the sum of their squares

$$\chi^2 = \sum_{i=1}^{k} Z_i^2 = \sum_{i=1}^{k} \frac{(x_i - \mu)^2}{\sigma_i^2} \tag{B.6}$$

is distributed according to the chi-square distribution with k degree of freedom (d.o.f.). χ^2 statistic characterizes the dispersion of the observed data from the real value. The numerator of Eq.B.6 is a measure of the spread of the observations, while the denominator is a measure of the expected spread. The χ^2 statistic for the data is

$$\chi_d^2 = \sum_{i=1}^{N} \frac{(d_i - E(d_i))^2}{\sigma_d^2} = \sum_{i=1}^{N} \frac{\left(\overline{f_i} + n_i - \overline{f_i}\right)^2}{d_i} = \sum_{i=1}^{N} \frac{n_i^2}{d_i}, \tag{B.7}$$

The variance is characterized by the χ^2 statistic, i.e.

$$\sigma^2 = \frac{1}{N} \chi^2, \tag{B.8}$$

so, from Eq.B.7, the first term of Eq.B.1 is given by

$$\sigma^2 = \frac{1}{N} \sum_{i=1}^{N} \frac{n_i^2}{d_i}. \tag{B.9}$$

Such a value is required to be equal to 1 to guarantee a good agreement between measurements and theory.

Appendix C

Statistical notions

C.1 Probability distributions

Poisson distribution

The Poisson distribution describes the results of random experiments when independent events are counts with a mean value $\bar{\nu}$. It gives the probability for a discrete variable ν. It is an approximation of the binomial distribution in the case where the number of trials is huge $(n \to \infty)$ and the success probability p is very small. The Poisson probability is given by:

$$P_\mu(\nu) = \frac{\mu^\nu}{\nu!} e^{-\mu}. \tag{C.1}$$

Mean and variance are both equal to μ. This is the basis of the well known statistical uncertainty associated with counting experiments: $\delta n = \sqrt{n}$.

Normal or Gaussian distribution

The Gaussian distribution describe the probability of a continuous variable x. It is given by:

$$p_{\mu,\sigma}(x) = \frac{1}{\sqrt{2\pi\sigma^2}} \exp\left(-\frac{(x-\mu)^2}{2\sigma^2}\right) \tag{C.2}$$

For $\mu \to \infty$, the Poisson distribution approaches the Gauss one with the same mean and standard deviation (Central Limit Theorem).
For Gaussian distributed uncertainties, it is expected that the probability that a given measurement should fall in the interval within $\mu \pm 1\sigma$ is 68.3%, within $\mu \pm 2\sigma$ 95%, within $\mu \pm 3\sigma$ 99.7%, ecc (see Fig. C.1).
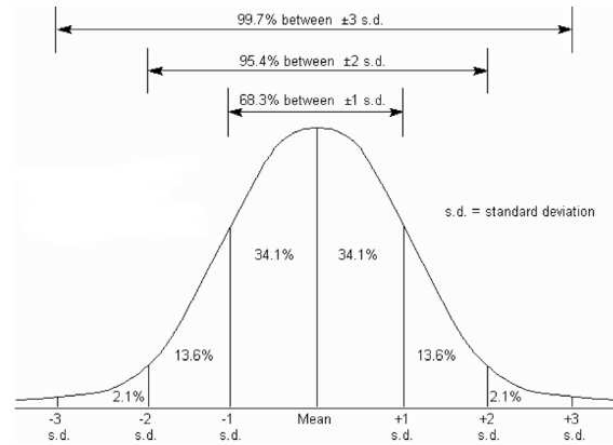
Figure C.1 Gaussian errors.

C.2   Random variables and the Bayes formula

The probability theory helps to deal with experimental data to obtain the most probable value of the measurement result. The random nature of the measurements can derive from the difficult control of the detection process or from the fact that what we want to study is intrinsically random (e.g. radiation emission). Measurements are well represented by random variables (r.v). The behaviour of a r.v. is described by the probability density function $f(x)$, where x is the r.v. and $f(x)dx$ gives the probability that the x value falls in $(x, x + dx)$ interval.

For our purposes, we limit to the multiplication theorem. Let A and B two events. Their product is defined as the event C that occurs when both A and B simultaneously occur. To enunciate this theorem, we need of some definitions. An event A is said dependent from B if the probability of A depends on the fact that B occurs or not. The probability of A, given that also B occurs, is called conditional probability of A, $P(A|B)$. So, their independency is expressed by $P(A|B) = P(A)$, while the dependency by $P(A|B) \neq P(A)$.

The product of two events is equal to that of one of the two events times the conditional probability of the other one, computed in the condition that the first has occurred:

$$P(AB) = P(A)P(B|A), \qquad (C.3)$$

or

$$P(AB) = P(B)P(A|B). \qquad (C.4)$$

The probability of the product of two independent events is equal to the product of the probabilities of the events, i.e. $P(AB) = P(A)P(B)$. Furthermore, if the events are exclusive $P(AB) = 0$.

The total probability formula directly derives from the theorem of probability product. Let H_i $i = 1, \ldots, n$ a complete set of mutually exclusive events called hypothesis, whose sum $H_1 + H_2 + \ldots + H_n = S$. For any given event $A \subset S$, the probability is given by:

$$P(A) = \sum_{i=1}^{n} P(H_i)P(A|H_i). \qquad (C.5)$$

The hypothesis theorem or Bayes formula is a consequence of the theorem of the product of probability and the total probability formula. Let H_i $i = 1, \ldots, n$ have known probability $P(H_i)$. An experiment is made and the event A is verified. What is the conditional probability $P(H_i|A)$ for each hypothesis?

By the theorem C.3 and C.4

$$P(AH_i) = P(A)P(H_i|A) = P(H_i)P(A|H_i) \quad i = 1, \ldots, n \qquad (C.6)$$

from which

$$P(A)P(H_i|A) = P(H_i)P(A|H_i) \quad i = 1, \ldots, n \qquad (C.7)$$

and, taking into account Eq.C.5, we get

$$P(H_i|A) = \frac{P(H_i)P(A|H_i)}{P(A)} = \frac{P(H_i)P(A|H_i)}{\sum_k P(H_k)P(A|H_k)} \quad i = 1, \ldots, n \qquad (C.8)$$

that is the Bayes formula. It explains the knowledge acquisition process, where the initial hypothesis are combined with the information derived by the taking place of specific effects. The initial hypothesis are modified into a continuous comparison with the experience. For this reason, $P(H_i|A)$ is also called posterior probability, $P(H_i)$ prior probability and $P(A|H_i)$ conditional probability or likelihood.

Often, in practice, we works with more than one r.v. at the same time, i.e. we deal with systems of r.v.. For them, the same rules of only one r.v. can

be used. Indeed, for two r.v. X and Y, the distribution function $F(x,y) \equiv P(X < x, Y < y)$ and the joint probability density $f(x,y) = \frac{\partial}{\partial x}\frac{\partial}{\partial y}F(x,y)$ can be written.

Necessary and sufficient condition for these two r.v. being independent is that the joint probability density is equal to the product of the marginal distributions of this two r.v., i.e.

$$f(x,y) = g(x)h(y), \tag{C.9}$$

where the marginal distributions of X and Y are defined as

$$g(x) = \int f(x,y)dy \qquad h(y) = \int f(x,y)dx. \tag{C.10}$$

The conditioned probability density, applying the theorem of the product Eq.C.3, is defined as:

$$f(y|x) = \frac{f(x,y)}{g(x)} \tag{C.11}$$

and, if the r.v. are independent, from Eq.C.9 we have

$$f(y|x) = \frac{g(x)h(y)}{g(x)} = h(y) \tag{C.12}$$

C.2.1 LR derived from Bayes theorem

Here the faithful Richardson's derivation [64] of the LR iterative formula (Eq.5.2) is reported. In its original formulation, he neglects the background radiation.

Here, for clarity of notation, the following form of the image formation equation is assumed:

$$d = Pf. \tag{C.13}$$

The Bayes theorem provides the conditional probability of an event f_i for a given value d_k of the r.v. δ. Indeed, if in Eq.C.8 $A = d_k$ and $H_i = f_i$, we find:

$$p(f_i|d_k) = \frac{p(f_i)p(d_k|f_i)}{\sum_j p(f_j)p(d_k|f_j)}, \tag{C.14}$$

where $p(d_k) = \sum_j p(f_j)p(d_k|f_j)$ is the total probability of d_k.

Considering all d_k and their dependence on f_i in accordance with Eq.C.13,

employing the marginal probability density in the discrete case, we can get

$$p(f_i) = \sum_k p(f_i d_k) = \sum_k p(f_i|d_k)p(d_k), \tag{C.15}$$

where, in the last equality, the theorem of the probability product (Eq.C.4) is used with $A = f_i$ and $B = d_k$. Substituting Eq.C.14 in Eq.C.15 gives

$$p(f_i) = \sum_k \frac{p(f_i)p(d_k|f_i)p(d_k)}{\sum_j p(f_j)p(d_k|f_j)}. \tag{C.16}$$

Bayes formula relates events at the ith location in the object f and those at the kth location in the image d, after observing that $p(d_k|f_i) = p_{ki}$ is the kth element of the matrix P in Eq.3.12. When this is applied, Eq.C.16 becomes

$$p^{(r+1)}(f_i) = p^{(r)}(f_i) \sum_k \frac{p(d_k|f_i)p(d_k)}{\sum_j p(d_k|f_j)p^{(r)}(f_j)} \quad r = 0, 1, \ldots \tag{C.17}$$

The initial point $p^0(f_i)$ is often estimated by means of Bayes's postulate (or theorem of the equidistribution of the ignorance), which assumes a uniform distribution so that $p^0(f_i) = 1/I$ or $f_i^0 = f/I$, where I is the identity matrix. Eq.C.17 can be reduced to a more easily workable form by expressing the probality of an event at the ith location in the object as $p(f_i) = f_i/f$ and the probality of an event at the kth location in the image as $p(d_k) = d_k/d = d_k/f$, since the restoration is a conservative process and $f = d$, and also $p(d_k|f_i) = p(P_{i,k}) = P_{i,k}/P$, $P = \sum_j p_j$. Eq.C.17 becomes

$$\frac{f_i^{(r+1)}}{f} = \frac{f_i^{(r)}}{f} \sum_k \frac{\frac{P_{ik}}{P}\frac{d_k}{f}}{\sum_j \frac{P_{jk}}{P}\frac{f_j^{(r)}}{f}} \tag{C.18}$$

or

$$f_i^{(r+1)} = f_i^{(r)} \sum_k \frac{P_{i,k}d_k}{\sum_j P_{j,k}f_j^{(r)}}. \tag{C.19}$$

In computer programming, taking into account also of the background b, the finite size of the arrays allows Eq.C.19 to be rewritten as Eq.5.2.

Appendix D

The MAP

D.1   Derivation of Eq.5.25

The probability density $p_\delta(d; f)$ is the conditional probability density of δ when the r.v. ϕ assumes the value f:

$$p_\delta(d; f) = p_\delta(d|\phi = f) = p_\delta(d|f). \tag{D.1}$$

It can be deduced from the known statistical properties of the Poisson noise. If both $p_\phi(f)$ and $p_\delta(d|f)$ are given, a complete knowledge of the total probability $p_{\phi\delta}(f, d)$ is found.

The joint probability density of the r.v. ϕ and δ is

$$p_{\phi\delta}(f, d) = p_\delta(d|f)p_\phi(f). \tag{D.2}$$

If the marginal probability density of δ is introduced

$$p_\delta(d) = \int p_{\phi\delta}(d, f)df, \tag{D.3}$$

from the theorem of the probability product, we have

$$p_{\phi\delta}(f, d) = p_\delta(d)p_\phi(f|d). \tag{D.4}$$

From the Bayes formula we obtain the conditional probability density of ϕ for a given value d of δ:

$$p_\phi(f|d) = \frac{p_{\phi\delta}(f, d)}{p_\delta(d)} = \frac{p_\delta(d|f)p_\phi(f)}{p_\delta(d)}, \tag{D.5}$$

i.e. it is the product of the likelihood function and of the a priori density function of ϕ. For further details see Appendix C.

If, in this equation, the detected value d of the r.v. δ is inserted, the conditional probability density of ϕ, called "a-posteriori" probability density of ϕ is obtained:

$$P_d^\phi(f) = p_\phi(f|d) = L(f)\frac{p_\phi(f)}{p_\delta(d)}, \tag{D.6}$$

that is just Eq.5.25.

D.2   Formulation of the Eq.5.26

A MAP estimate is defined as any object f_{MAP} that maximizes the a posteriori probability density (Eq.5.25):

$$f_{MAP} = \arg\max_f P_d^\phi(f) \tag{D.7}$$

As in the ML case, it is convenient considering the neg-log of $P_d^\phi(f)$. If a Gibbs prior for $p_\phi(f)$ is assumed, the following functional can be introduced:

$$
\begin{aligned}
J(f;d) &= -\ln P_d^\phi(f) - \ln Z - \ln p_\delta(d) = \\
&= -\ln L(f) + \ln Z + \mu\Omega(f) + \ln p_\delta(d) - \ln Z - \ln p_\delta(d) = \\
&= J_0(f;d) + \mu J_R(f).
\end{aligned} \tag{D.8}
$$

Here $J_0 = (f;d) - \ln L(f)$ is the functional derived by ML approach (the KL divergence) and $J_R(f) = \Omega(f)$ is that coming from the Gibbs prior, conceived as a regularization functional.

The MAP problem takes the following form:

$$f_{MAP} = \arg\min_f \{J(f;d)\}. \tag{D.9}$$

The optimization problem to be solved for obtaining the f_{MAP} estimate of the unknown object is:

$$\min J(f;d) = J_0(f;d) + \mu J_R(f) \tag{D.10}$$

$$s.t. \quad f \geq 0$$

$$\sum_{j=1}^{N} f_j = c,$$

In the previous problem, the total flux conservation is introduced as a constraint.

Both $J_0(f; d)$ and $J_R(f)$ are convex so that we have a convex minimization problem. The KKT conditions are necessary and sufficient for an object f_{MAP} to be a global minimum of $J(f; d)$, i.e.

$$f_{MAP}\nabla J(f; d) = 0 \qquad f_{MAP} \geq 0 \qquad \nabla J_\mu(MAP) \geq 0. \qquad (D.11)$$

Bibliography

[1] M. Allain. Proceedings of the 5th INTEGRAL Workshop on the IN-TEGRAL Universe (ESA SP-552). page 823, 2004.

[2] M. Allain and J.P. Roques. *A&A*, 447(3):1175, 2006.

[3] B. Aschenbach. *Reports on Progress in Physics*, 48:579, 1985.

[4] L.D. Baumert. *SIAM J.Appl.Math.*, 17:826, 1969.

[5] L.D. Baumert. *Cyclic Difference Sets. Lecture Notes in Maths.*, volume 17. Springer-Verlag, Berlin, 1971.

[6] A.J. Bird, A. Bazzano, and L. Bassani et al. *ApJ Suppl. Series*, 186:1, 2010.

[7] A.J. Bird, A. Malizia, and A. Bazzano et al. *ApJ Suppl. Series*, 170:175, 2007.

[8] E. Boldt. *Phys.Rep.*, 146:215, 1987.

[9] E. Boldt. *Physics of Neutron Stars and Black Holes.* Y.Tanake editor, 1988.

[10] E. Boldt. *X-ray astronomy*, SP-296:797, 1989.

[11] E. Boldt. The X-ray background. page 149, 1992.

[12] S. Bowyer, E.T. Byram, and T.A. Chubb et al. *Science*, 147:394, 1965.

[13] D. Calabro and J.K. Wolf. *Inf.Contro.*, 11:537, 1968.

[14] E. Caroli, R.C. Butler, and G. Di Cocco et al. *Il Nuovo Cimento*, 7C(6):786, 1984.

[15] E. Caroli, J.B. Stephen, and G. Di Cocco et al. *Space Science Reviews*, (45):349, 1987.

[16] Y. Chen, T.P. Li, and M. Wu. *Astronomical Data Analysis Software and Systems VI, ASP Conference Series*, (125), 1997.

[17] M. Chernyakova. Introduction to the INTEGRAL Data Analysis. Issue 5.1. November 2005. http://www.isdc.unige.ch/integral/analysis.

[18] M. Chernyakova and A. Neronov. IBIS Analysis User Manual. Issue 9.2. July 2010. http://www.isdc.unige.ch/integral/analysis.

[19] A. Comastri, G. Setti, G. Zamorani, and G. Hasinger. *A&A*, 1(296), 1995.

[20] J.M. Comella, H.D. Craft, and R.V.E. Lovelace et al. *Nature*, (221):453, 1969.

[21] T.J.-L. Courvoisier, R. Walter, and V. Beckmann et al. *A&A*, (411):L53, 2003.

[22] P. Diaconis and B. Efron. *Scientific American*, page 116, 1983.

[23] P.P. Dunphy, M.L. McConnell, and A. Owens et al.

[24] B. Efron. *The Annals of Statistics*, 7(1):1.

[25] R.D. Evans. *The Atomic Nucleus*. McGraw-Hill Book Company, 1979.

[26] E.E. Fenimore. *Appl.Opt.*, 17(22):3562, 1978.

[27] E.E. Fenimore. *Appl.Opt.*, 19(14):2465, 1980.

[28] E.E. Fenimore and T.M. Cannon. *United States Patent*, 4(209):780, 1980.

[29] E.E. Fenimore and T.M. Cannon. *Appl.Opt.*, 20(10):1858, 1981.

[30] E.E. Fenimore and T.M.Cannon. *Appl.Opt.*, 17(3):337, 1978.

[31] P. Ferrando. *SPIE Proc.*, 5168, 2003.

[32] F. Frontera. *Exp.Astr.*, 2:25, 1995.

[33] F. Frontera, M. Orlandini, and R. Landi et al. *ApJ*, 666:86, 2007.

[34] R. Giacconi, H. Hursky, F.R. Paolini, and B.B. Rossi. *Phys.Rev.Lett.*, 9(439), 1962.

[35] R. Gilli. *Adv. Space Res.*, 34:2470, 2004.

[36] A. Goldwurm, P. David, and L. Fochini et al. *A&A*, 411:L223, 2003.

[37] A. Goldwurm, P. Goldoni, and A. Gros et al. *Proc. of the 4th INTE-GRAL Workshop, ed. A.Gimenez, V. Riglero and C. Wrinkler, ESA-SP*, 459:497, 2001.

[38] S.R. Gottesman and E.E. Fenimore. *Appl.Opt.*, 28(20):4344, 1989.

[39] A. Gros, A. Goldwurm, and M. Cadolle-Belle M. et al. *A&A*, 411:L179, 2003.

[40] D.E. Gruber. *The X-ray Background.* Cambridge Univ.Press, 44, 1992.

[41] D.E. Gruber, J.L. Matterson, L.E. Peterson, and G.V. Jung. *ApJ*, 520:124, 1999.

[42] R.J. Hanish and L. White. *Proc. of a Workshop held at the Space Telescope Science Institute, Baltimore, NASA*, 20-21 November 1993.

[43] J.A. Hogbom. *A&A*, (15):417, 1974.

[44] T.J. Holmes. *J.Opt.Soc.Amer.A.*, (5):666, 1988.

[45] B.R. Hurt. *SPIE Proc.*, (1567):600, 1991.

[46] P. L. Jensen, K. Clausen, and C. Cassi et al. *A&A*, (411):L7, 2003.

[47] J. Jimenez, P. Olmos, J.L. de Pablos, and J.M. Perez. *Appl.Opt.*, 30(5):549, 1991.

[48] K.D. Joensen. *Proc.SPIE*, (2011):360, 1993.

[49] H.M. Johnson and C.B. Stephenson. *ApJ Letters*, (146):602, 1966.

[50] R.L. Kinzer, G.V. Jung, and D.E. Gruber et al. *ApJ*, 475(361), 1997.

[51] G. Knoll. *Radiation Detection and Measurements.* John Wiley & Sons, Inc., 1999.

[52] C. Labanti, G. Di Cocco, and G. Ferro et al. *A&A*, (411):L149, 2003.

[53] F. Lebrun, J.P. Leray, and P. Lavocat et al. *A&A*, (411):L141, 2003.

[54] T.P. Li. *Nuclear Physics B (Proc. Suppl.)*, (166):131, 2007.

[55] T.P. Li and M. Wu. *Ap.&SS*, (206):91, 1993.

[56] T.P. Li and M. Wu. *Ap.&SS*, (215):213, 1994.

[57] L.B. Lucy. *ApJ*, (79):745, 1974.

[58] N. Lund, S. Brandt, and C. Budtz-Jorgensen et al. *A&A*, (411):L231, 2003.

[59] F.E. Marshall, E.A. Boldt, and S.S. Holt et al. *ApJ*, (235):4, 1980.

[60] M. Mas-Hesse, A. Gimenez, and L. Culhane et al. *A&A*, (411):L261, 2003.

[61] S. Miyamoto, H. Tsunemi, and K. Tsono. *Nucl.Inst.Meth.*, (180):557, 1981.

[62] M. Orlandini, L. Sambo, and F. Frontera. Technical Report HXMT-IASFBO-09-534, 2009.

[63] D. Pellicciotta. *IEEE Trans.Nuc.Sc.*, 53(1), 2006.

[64] M.W. Richardson. *J.Opt.Soc.Am.*, (62):55, 1972.

[65] G.B. Rybicky and A.P. Lightman. *Radiative processes in astrophysics*. John Wiley and Sons, 2000.

[66] L. Sambo, J.B. Stephen, S. Bonettini, G. Zanghirati, and F. Frontera. Improving the angular resolution of coded aperture instruments using a modified Lucy-Richardson algorithm for deconvolution. In *Proceedings of The Extreme Sky: Sampling the Universe above 10 keV, October 13-19 2009, Otranto (Lecce), Italy*, 2009. https://pos.sissa.it/cgi-bin/reader/conf.cgi?confid=96.

[67] A.R. Sandage, P. Osmer, and R. Giacconi et al. *ApJ*, (146):316, 1966.

[68] S. Scaringi, A.J. Bird, and A.B. Hill et al. *A&A*, (516):A75, 2010.

[69] E. Schreier, R. Levinson, and H. Gursky et al. *ApJ Letters*, (172):L79, 1972.

[70] G. Setti and L. Woltier. *A&A*, (224):L21, 1989.

[71] Z.J. Shen and J.F. Zhou. *High energy and nuclear physics*, 31(11):1016, 2007.

[72] Z.J. Shen and J.F. Zhou. *Chin.J.Astrophys.*, 8(3):343, 2008.

[73] L.A. Shepp and J. Vardi. *IEEE Trans.Med.Imag.*, (MI-1):113, 1982.

[74] Manoj Kumar Singh, Uma Shanker Tiwary, and Young-Hoon Kim. *EURASIP Journal of Advances in Signal Processing*, 2008.

[75] G.K. Skinner. *Appl.Opt.*, 47:2739, 2008.

[76] G.K. Skinner and R.M. Rideout. Imaging in high energy astronomy. In *Proceedings of the International Workshop held in Anacapri (Capri-Italy), 26-30 September 1994*, page 177, 1995.

[77] J.B. Stephen and E. Caroli et al. *A&A*, (185):343, 1987.

[78] IBIS Team. http://www.isdc.unige.ch/integral/catalogue.

[79] IBIS Team. http://www.isdc.unige.ch/integral/analysis.

[80] P. Ubertini, F. Lebrun, and G. Di Cocco et al. *A&A*, (411):L131, 2003.

[81] G.M.P. van Kempen and L.J. van Vliet. *J.Opt.Soc.Am.A*, 17(3), 2000.

[82] J. Vardi, L.A. Shepp, and L. Kaufman. *J.Am.Stat.Association*, (80):8, 1985.

[83] A. Vecchi, S. Molendi, and W. Guainazzi et al. *A&A*, (349):L73, 1999.

[84] G. Vedrenne, J.P. Roques, and V. Schoenfelder et al. *A&A*, (411):L63, 2003.

[85] R.L. White and J. Allen. *Proc. of a Workshop held at the Space Telescope Science Institute, Baltimore, NASA*, 20-21 August 1990.

[86] C. Winkler, T.J.-L. Courvoisier, and G. Di Cocco. *A&A*, (411):L1, 2003.

[87] H. Wolter. *Ann.Phys.*, 10:94, 1952.

[88] H. Wolter. *Ann.Phys.*, 10:286, 1952.

[89] W.H. Zachariasen. *Theory of X-ray diffraction in Crystals*. Dover Pubblications, 1949.

[90] W.H. Zachariasen. *Acta Cryst.*, 23:558, 1967.

Acknowledgments

Voglio dedicare questo lavoro a tutte le mie Famiglie, a tutte le persone che in questi anni mi sono state accanto, persone che oggi sono quì con me a festeggiare e persone il cui spirito mi ha e mi sta accompagnando.

Voglio ringraziare Davide, mio compagno, amico e confidente per la vita. Grazie per avermi sorretto in questi ultimi mesi, per avermi aiutato, amato e appoggiato. Ringrazio i tuoi genitori, perchè, se sei la persona che ho sposato un anno e mezzo fa, è anche un po' merito loro.

Voglio ringraziare i miei genitori e mio fratello. Forse vi ho giudicato per avermi cresciuta dandomi troppe responsabilità, ma oggi vi ringrazio perchè sono quella che sono, coi miei pregi e i miei difetti, una persona che ogni mattina può guardarsi allo specchio senza abbassare lo sguardo.

Voglio ringraziare i miei nipotini Daniele, Mattia e Giacomo. La purezza e la sincerità di un bimbo sono disarmanti e, allo stesso tempo, ti riempiono la vita.

Voglio ricordare tutte le persone che ci hanno lasciato in questo ultimo anno: Alessandro, Andrea, Antonio, Maria e Concettina. La vostra storia mi ha reso ancor più chiaro quali sono i Veri Valori della vita.

Un grazie particolare va ad Andrea, Eleonora e Vittoria: il compito che avete affidato a Davide e a me ci onora e allo stesso tempo ci spaventa, ma siamo certi che non saremo soli nel portarlo avanti. Lassù Qualcuno, insieme al tuo papà, ama mamma e te e non vi lascerà mai.

Infine, non per ordine di importanza, voglio ringraziare tutta la mia Comunità per avermi sostenuto e aver pregato per me. La comunione e la fede uniscono tanto quanto (se non di più) dei legami di sangue.

Per quanto riguarda questo lungo e difficile lavoro, ringrazio il Prof. Filippo Frontera per gli utili spunti di riflessione e per avermi saputo indicare le persone con cui ho attivamente lavorato in questi tre anni. Per una per-

sona che è stata formata in un'altra università non è semplice sapere a quale porta bussare per chiedere aiuto.

Voglio ringraziare John B. Stephen per l'enorme pazienza e professionalità dimostrata, per avere messo a mia disposizione il suo enorme bagaglio di conocenze.

Voglio ringraziare Silvia Bonettini e Gaetano Zanghirati per avermi pazientemente introdotto nel campo nell'analisi numerica. Vi posso assicurare che per un fisico non è cosa semplice. Grazie alla passione che mettete nel vostro lavoro, ho ricevuto da voi la forza per non abbandonare questo progetto. Un progetto che alla fine, dopo tre anni, mi piace, trovo stimolante e del quale vorrei continuare ad occuparmi.

UNIFE

FORMAZIONE POSTLAUREA
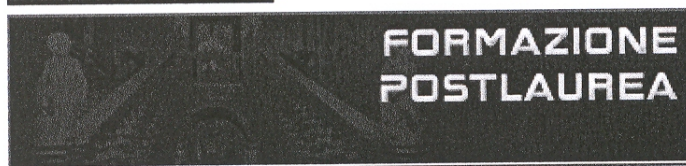
Your E-Mail Address
>   sambo@fe.infn.it

Subject
>   Diciarazione di Conformita'

Io sottoscritto Dott. (Cognome e Nome)
>   Sambo Lara

nato a
>   Cavarzere

Provincia
>   Venezia

il giorno
>   20/05/1981

avendo frequentato il corso di Dottorato di Ricerca in:
>   Fisica

Ciclo di Dottorato
>   XIII

Titolo della tesi in Italiano
>   Un metodo iterativo per deconvolvere immagini di strumenti a maschera codificata

Titolo della tesi in Inglese
>   An iterative method to deconvolve coded-mask images

Titolo della tesi in altra Lingua Straniera

Tutore - Prof:
>   Frontera Filippo

Settore Scientifico Disciplinare (SSD)
>   FIS/05

Parole chiave (max 10)
>   coded-mask, Lucy, Richardson, INTEGRAL, IBIS

Consapevole - Dichiara
>   CONSAPEVOLE --- 1) del fatto che in caso di dichiarazioni mendaci, oltre alle sanzioni previste dal codice penale e dalle Leggi speciali per l'ipotesi di falsità in atti ed uso di atti falsi, decade fin dall'inizio e senza necessità di alcuna formalità dai benefici conseguenti al provvedimento emanato sulla base di tali dichiarazioni; -- 2) dell'obbligo per l'Università di provvedere al deposito di legge delle tesi di dottorato al fine di assicurarne la conservazione e la consultabilità

da parte di terzi; -- 3) della procedura adottata dall'Università di Ferrara ove si richiede che la tesi sia consegnata dal dottorando in 4 copie di cui una in formato cartaceo e tre in formato .pdf, non modificabile su idonei supporti (CD-ROM, DVD) secondo le istruzioni pubblicate sul sito : http://www.unife.it/dottorati/dottorati.htm alla voce ESAME FINALE – disposizioni e modulistica; -- 4) del fatto che l'Università sulla base dei dati forniti, archivierà e renderà consultabile in rete il testo completo della tesi di dottorato di cui alla presente dichiarazione attraverso l'Archivio istituzionale ad accesso aperto "EPRINTS.unife.it" oltre che attraverso i Cataloghi delle Biblioteche Nazionali Centrali di Roma e Firenze. --- DICHIARO SOTTO LA MIA RESPONSABILITA' --- 1) che la copia della tesi depositata presso l'Università di Ferrara in formato cartaceo, è del tutto identica a quelle presentate in formato elettronico (CD-ROM, DVD), a quelle da inviare ai Commissari di esame finale e alla copia che produrrò in seduta d'esame finale. Di conseguenza va esclusa qualsiasi responsabilità dell'Ateneo stesso per quanto riguarda eventuali errori, imprecisioni o omissioni nei contenuti della tesi; -- 2) di prendere atto che la tesi in formato cartaceo è l'unica alla quale farà riferimento l'Università per rilasciare, a mia richiesta, la dichiarazione di conformità di eventuali copie; -- 3) che il contenuto e l'organizzazione della tesi è opera originale da me realizzata e non compromette in alcun modo i diritti di terzi, ivi compresi quelli relativi alla sicurezza dei dati personali; che pertanto l'Università è in ogni caso esente da responsabilità di qualsivoglia natura civile, amministrativa o penale e sarà da me tenuta indenne da qualsiasi richiesta o rivendicazione da parte di terzi; -- 4) che la tesi di dottorato non è il risultato di attività rientranti nella normativa sulla proprietà industriale, non è stata prodotta nell'ambito di progetti finanziati da soggetti pubblici o privati con vincoli alla divulgazione dei risultati, non è oggetto di eventuali registrazioni di tipo brevettale o di tutela. --- PER ACCETTAZIONE DI QUANTO SOPRA RIPORTATO

Firma Dottorando
Ferrara, lì 26/01/2011 Firma del Dottorando _____
Firma Tutore
Visto: Il Tutore Si approva Firma del Tutore _____